Delft University of Technology

Citation (APA)
Nasirpour, F. (2026). *Multi-Winding Transformer Modeling for Fast-Front Transient Analysis*. [Dissertation (TU Delft), Delft University of Technology]. https://doi.org/10.4233/uuid:cc47b486-2423-497b-b6d7-1fc99cb0110f

Multi-Winding Transformer Modeling For Fast-Front Transient Analysis

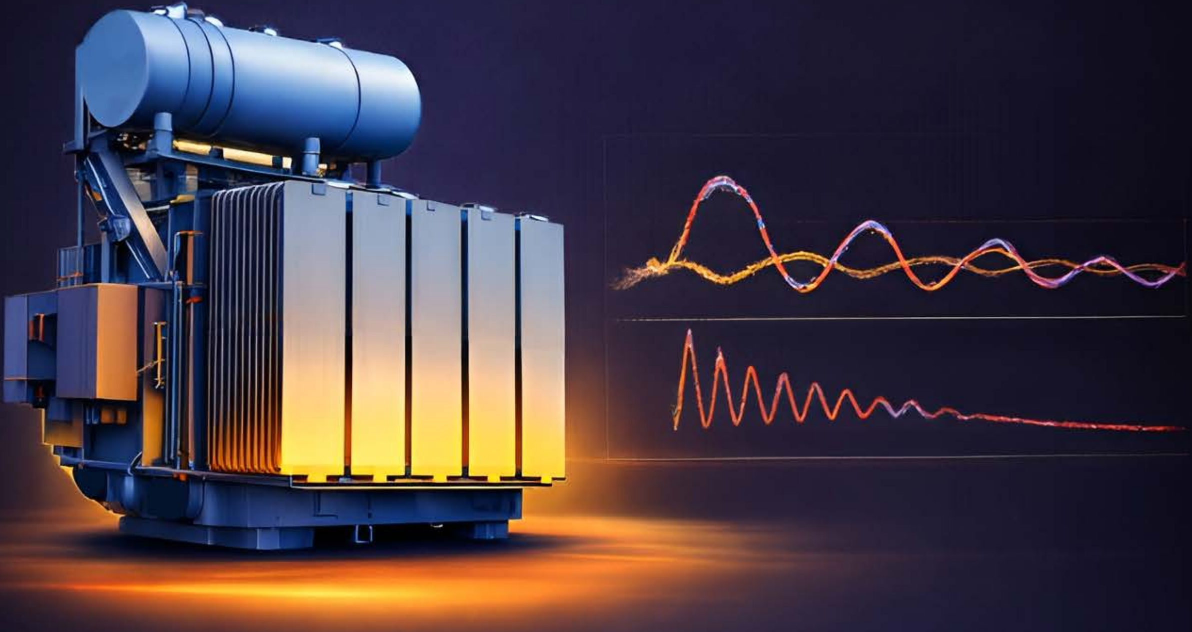

TU Delft

Farzad Nasirpour

Multi-Winding Transformer Modeling for Fast-Front Transient Analysis

Multi-Winding Transformer Modeling for Fast-Front Transient Analysis

Dissertation

for the purpose of obtaining the degree of doctor
at Delft University of Technology
by the authority of the Rector Magnificus, Prof. dr. ir. H. Bijl,
chair of the Board for Doctorates
to be defended publicly on
Monday 23 February 2026 at 12:30

by

Farzad NASIRPOUR

This dissertation has been approved by the promotors.

Composition of the doctoral committee:

Rector Magnificus,	chairperson
Prof. dr.ir. M. Popov,	Delft University of Technology, *promotor*
Dr. ir. M. Ghaffarian Niasar	Delft University of Technology, *promotor*
Independent members:	
Prof. dr. P. Palensky	Delft University of Technology
Prof. ir. P.T.M. Vaessen	Delft University of Technology
Prof. dr. ing. A. Neto	Delft University of Technology
Prof. dr. E. Rahimpour	Technical University of Applied Sciences Würzburg-Schweinfurt, Germany
Ir. L.W.A. Dorpmanns	Royal SMIT Transformers B.V., The Netherlands
Dr. J. Dong	Delft University of Technology, reserve member

Keywords: High-Frequency Modeling, Machine Learning in Power Systems, Power Transformers, White-Box Modeling
Cover by: Farzad Nasirpour/ GPT 5

ISBN 978-94-6536-048-5

To my parents

CONTENTS

SUMMARY

Power transformers are critical components of electrical power systems, and their behavior under high-frequency and fast transient conditions plays an important role in overall system reliability. Phenomena such as internal resonances within transformer windings can lead to significant overvoltages and localized electric field intensification, potentially resulting in insulation degradation or failure. Accurate modeling of transformer behavior over a wide frequency range is therefore essential for both design and transient analysis. However, conventional transformer models are often limited by either oversimplified analytical assumptions or the high computational cost and limited generalization capability of purely numerical approaches.

This thesis presents a comprehensive framework for the frequency-dependent modeling of power transformers, with particular emphasis on high-frequency behavior. The work focuses on the development of white-box models derived from electromagnetic field theory, complemented by data-driven machine learning techniques to enhance computational efficiency while preserving physical consistency.

The first part of the thesis investigates the impact of conductor and core losses on the impedance characteristics of transformer windings. Numerical simulations are employed to quantify the influence of eddy current losses in both conductors and ferromagnetic cores. The results demonstrate that each loss mechanism dominates in different frequency ranges, and that neglecting conductor losses can lead to significant errors in impedance estimation and resonance prediction at higher frequencies relevant to electromagnetic transient studies.

Building upon these insights, the thesis develops an analytical framework for frequency-dependent impedance modeling of transformer windings. To validate the proposed analytical approach, several case studies are presented in which the derived impedance characteristics and parameters are compared against numerical simulations and experimental measurements, demonstrating good agreement across a broad frequency range. The analyses confirm the capability of the proposed approach to accurately capture resonance phenomena and frequency-dependent losses with substantially reduced computational effort compared to full numerical field solvers.

In the final part of the thesis, a machine learning-based methodology is introduced to further accelerate the estimation of frequency-dependent winding impedances. Using a dataset generated from the analytical framework, an XGBoost model is trained to predict the frequency dependent parameters. The results show that the proposed data-driven models achieve high accuracy while offering significant computational speed-ups, making them well suited for large-scale parametric studies and design optimization.

Overall, this thesis contributes a unified modeling framework that bridges analytical electromagnetic theory, numerical validation, and machine learning techniques for the high-frequency modeling of power transformers. The proposed methods enable accurate and efficient prediction of transformer winding behavior under fast transient conditions, providing valuable tools for transformer designers and power system engineers.

1

INTRODUCTION

To trace something unknown back to something known is called explanation.

1.1. TRANSFORMER FAILURES AND TRANSIENTS

Since their invention in the 19th century, transformers have been indispensable to the evolution and expansion of electrical power systems. As the heart of electricity networks [1], they enable long-distance power transmission, making large-scale electrification possible. Today, power transformers remain among the most vital components in power systems, playing a fundamental role in the reliable delivery of electricity to end-users. Ensuring their continuous operation is essential for the reliable generation and transmission of electric power. Given the growing demand and economic constraints, utilities are exposed to pressure to maintain the reliability of these assets. Throughout their operational lifetime, transformers are subjected to a range of electrical, mechanical, thermal, and chemical stresses. These stresses may result in failures, causing catastrophic operational interruptions, unscheduled outages, substantial financial losses, system blackouts and brownouts, and potential safety hazards for personnel [2–4].

Transformer failures are generally classified into electrical, mechanical, and thermal categories [8]. Statistical analyses conducted by researchers indicate that around 35% of transformer major failures are attributed to insulation matters, with a significant share occurring in the windings [9, 10]. Figure 1.1 shows examples of such a failure [5–7]. A considerable number of transformer failures, particularly in high-voltage (HV) and extra-high-voltage (EHV) systems, have been attributed to transient overvoltages. As reported in [11], the main sources of transient-induced failures include switching surges, voltage spikes, line faults, and various transmission and distribution disturbances, which

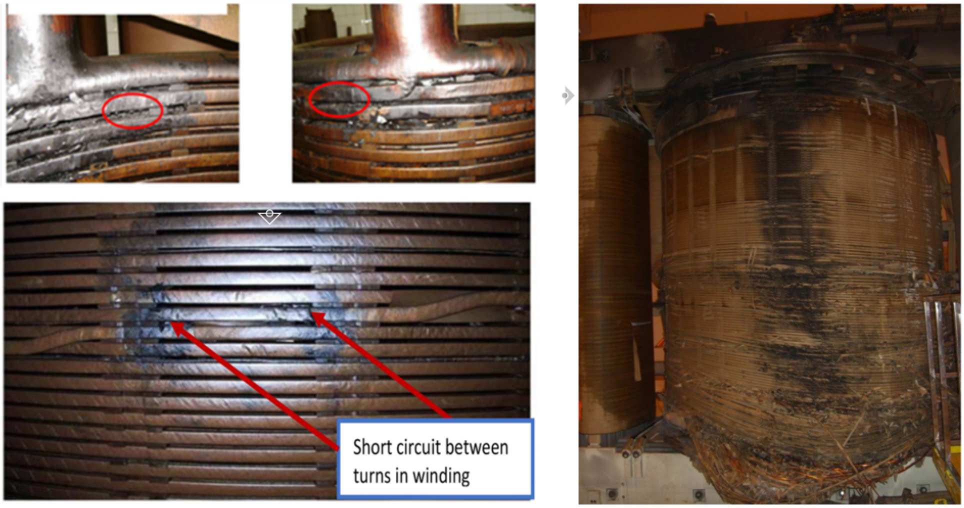

Short circuit between turns in winding

Figure 1.1: Examples of dielectric faults in transformers [5–7].

together account for approximately 29% of all failures. In addition, lightning-induced incidents, which are not included in this figure, are estimated to contribute an additional 17%.

Transformers exhibit different behavior under transient conditions compared to steady-state operation. One of the primary reasons for failure during such events is the nonlinear voltage distribution along the winding caused by high-frequency excitations. Under normal operating conditions, the voltage distributes linearly across the winding due to the dominant inductive behavior. However, at high frequencies, the capacitive characteristics of the winding become more significant, resulting in a highly nonlinear voltage distribution. As an illustrative example, consider the coil depicted in Figure 1.2(a), where each disk has a series capacitance C_s and a capacitance to ground C_g. This coil can be modeled as a capacitive network, as shown in Figure 1.2(b). The voltage distribution in such a system can be analyzed using the parameter α, defined as [12]:

$$\alpha = \sqrt{\frac{C_g}{C_s}} \tag{1.1}$$

As α increases, the voltage distribution becomes more nonlinear, as demonstrated in Figure 1.3. This nonuniform distribution leads to increased electric field intensities at the terminal of the winding, increasing the likelihood of insulation breakdown.

Another important concern is the possibility of resonances within the transformer. This phenomenon can be conceptually explained using the simplified equivalent circuit shown in Figure 1.4 [13]. When the natural frequencies of two subcircuits (subcircuit 1 and subcircuit 2) are nearly equal [13]:

$$\sqrt{\frac{1}{L_1C_1}} \approx \sqrt{\frac{1}{L_2C_2}} \tag{1.2}$$

and the surge impedance of subcircuit 2 is significantly higher than that of subcircuit 1 [13]:

$$\sqrt{\frac{L_2}{C_2}} \gg \sqrt{\frac{L_1}{C_1}} \tag{1.3}$$

substantial voltage amplification may occur at node C, as illustrated in Figure 1.5. In practical scenarios, the transformer behaves as a highly complex RLC network with multiple resonance frequencies. Nevertheless, the same underlying principles remain valid. Excessive resonant overvoltages at internal winding points, taps, or terminals can arise under the following conditions [13]:

- A transient voltage with a dominant frequency component f_0 excites the transformer terminals, and this frequency matches with a resonance peak in the internal or external voltage transfer characteristic of the transformer;
- At this frequency f_0, the transformer's input impedance is considerably higher than the source or network impedance.

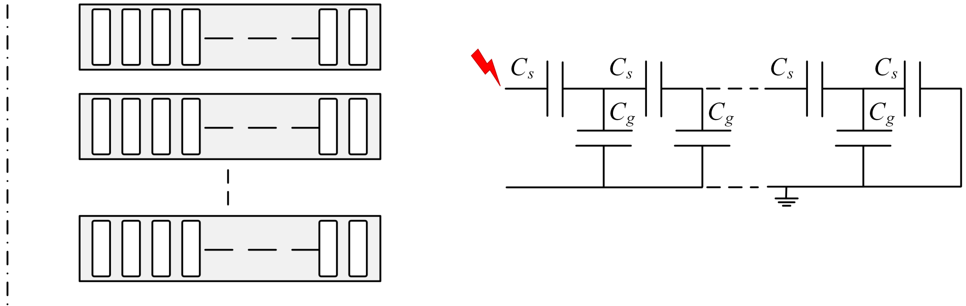

(a) (b)

Figure 1.2: (a) An illustration of a winding, and (b) its equivalent capacitance ladder network for distribution of surge voltage across transformer windings.

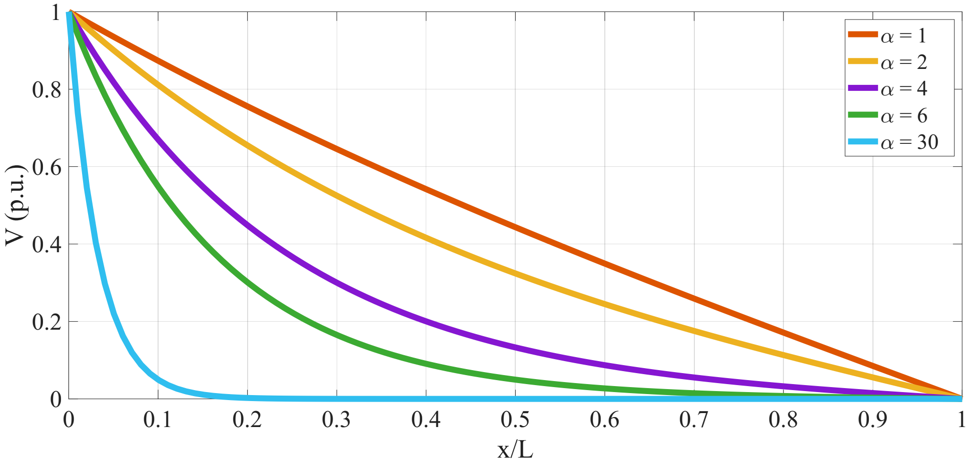

Figure 1.3: Voltage distribution along the winding for various values of α. L is the total length of the winding.

Studies have shown that resonance-related conditions are not uncommon and have contributed to transformer failures [14]. Many of these failures have been linked to high-frequency transient events, such as lightning strikes, cable energization, capacitor bank switching, and system faults, which excite internal winding resonances, especially when the transformer is lightly loaded [15].

Despite rigorous factory testing procedures, these transient scenarios are not adequately addressed in presently applied standards [13]. For example, standard lightning impulse tests assume specific wave shapes and often involve grounding of non-excited terminals, which fail to replicate the voltage transfer characteristics observed under actual service conditions. As emphasized by CIGRÉ JWG A2/C4.39 [13], such standardized test setups are insufficient for simulating fast-front or oscillatory waveforms arising from switching events, GIS operations, HVDC converters, or energization through long cables.

A key issue is that these transients may contain dominant frequency components that match the natural frequencies of transformer windings. When this occurs, internal voltages can be significantly amplified because of resonance, even if the magnitude of the impinging overvoltage is well below the surge arrester protection level. This resonant amplification poses a serious risk to the transformer insulation system. Moreover, such internal overvoltages are often not observable from the terminals, making them difficult to detect with standard diagnostic techniques [13].

To address these challenges, it is essential to develop detailed

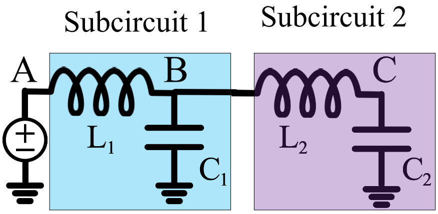

Figure 1.4: Simplified circuit illustrating resonance when the natural frequencies of two sub-circuits are nearly equal.

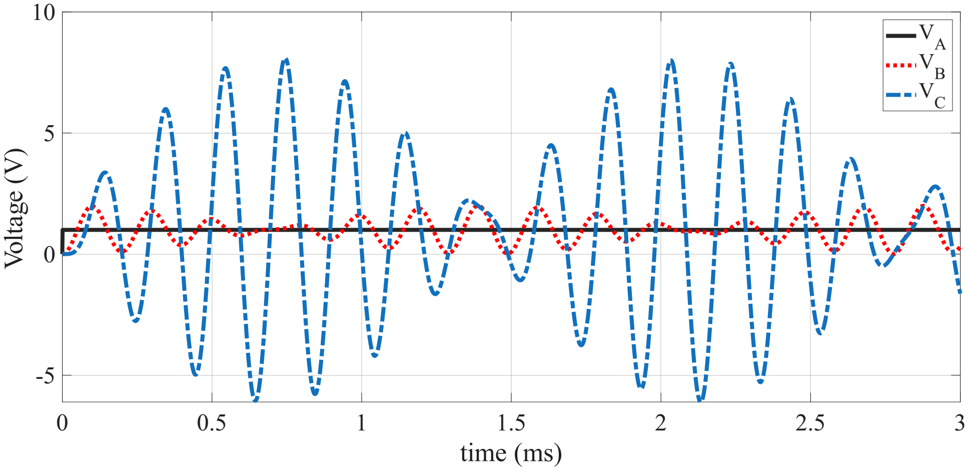

Figure 1.5: Voltage at points A, B, and C.

white-box models that will accurately represent the internal voltage transfer characteristics and transformer terminal impedance within a wide frequency range. These models should also be suitable for use in time-domain transient simulations, enabling more realistic analysis of these phenomena.

1.2. PROBLEM STATEMENT

The accurate modeling of transformers at high frequencies remains a significant challenge for academic research and practical engineering. Conventional analytical high-frequency transformer models are often inadequate for simulating fast transient events. Many of these models either neglect electromagnetic phenomena (such as skin and proximity effects) or account for them using simplified approximations [16–26]. However, these effects become increasingly significant at higher frequencies and must be accurately represented for reliable modeling. Numerical methods, such as finite element analysis (FEA), can capture complex electromagnetic interactions [27–35]. However, these methods are computationally demanding and require a lot of time to be built for a particular transformer.

Measurement-based, or black-box, modeling approaches have been widely employed to overcome some of the limitations of analytical methods. Although these models can provide accurate results within the specific frequency range and operating conditions under which they are derived, they lack a direct link to the physical structure of the transformer. Consequently, their applicability is limited when assessing design modifications or investigating failure mechanisms. Furthermore, these models depend on experimental measurements, making them unsuitable for use during the early design stages.

What is missing is an analytical modeling framework that accurately represents high-frequency transformer behavior. Such a model would provide both insight and computational efficiency, enabling the study of internal resonances, high-frequency transients, and their role in transformer failure. This thesis aims to address this gap by developing a physically based, analytical approach in high-frequency transformer modeling. The proposed method aims to capture essential electromagnetic effects using mathematical formulations derived from field theory, thereby offering a balance between accuracy and computational efficiency.

1.3. RESEARCH OBJECTIVES AND QUESTIONS

The primary objective of this research is to develop an analytical modeling framework that accurately represents the high-frequency behavior of power transformers. To achieve this goal, the following specific objectives are pursued:

- To derive frequency-dependent self- and mutual impedance expressions for transformer windings using electromagnetic field theory.
- To validate the proposed models with simulations and available measurements.
- To demonstrate the applicability of the model for analysis of high-frequency resonances and potential failure mechanisms in transformer operation.

Based on these objectives, the central research questions addressed in this thesis are:

1. What is the role of the transformer core at high frequencies, and how does it influence the overall transformer behavior?
2. How can electromagnetic interactions within transformer windings be accurately captured through analytical formulations at high frequencies?
3. To what extent can analytical models reliably predict the frequency-dependent impedance characteristics required for transient studies?
4. Can an analytical model simultaneously offer physical insight and practical value for engineers to analyse high-frequency transformer failures?

These questions form the basis of the proposed modeling framework and guide the structure, methodology, and analysis presented throughout this thesis.

1.4. FRAMEWORK

The modeling approach adopted in this thesis is rooted in analytical electromagnetic field theory, aiming to characterize the high-frequency behavior of power transformers in a physically consistent and computationally efficient manner. Instead of relying on purely empirical or fully numerical models, this work derives analytical expressions for transformer impedance directly from conductor geometry, material properties, and the electromagnetic behavior of the transformer in high-frequency regimes.

The overall methodology comprises the following components:

- **Electromagnetic field formulation:** The impedance of transformer windings is derived from Maxwell's equations using a quasi-static approximation appropriate for the high-frequency range of interest. The magnetic vector potential $\vec{A}$ is employed as the primary field variable, enabling the analytical computation of self- and mutual impedances. The influence of eddy current losses in the conductors and core is accounted for separately, reflecting the distinct behavior of the transformer core at high frequencies.
- **Model validation:** The accuracy and applicability of the proposed model are assessed through comparison with benchmark results, electromagnetic simulations, and measurements carried out on a three-phase transformer (see Figure 1.6). Emphasis is placed on validating the model over a wide frequency range, particularly in regions where resonant phenomena are known to occur.

- **Model implementation:** Following model validation, the developed analytical model was implemented in an EMT-based simulation environment. To enable practical use in such environments, a reduced-order version of the model is derived, which accurately reproduces the terminal behavior of the transformer while significantly reducing computational demands. This reduction also allows for the inclusion of internal points that experience the highest voltage amplification within the winding. The primary motivation for model order reduction is to facilitate efficient simulation in EMT-based tools, as the full model is computationally intensive. Furthermore, in cases where transformer manufacturers develop such detailed models, they may prefer to share only terminal equivalent representation with clients to preserve proprietary information. In such scenarios, the reduced-order model enables network studies without exposing the internal details of the transformer.

- **Machine learning-based parameter estimation:** A machine learning-based approach is introduced for the rapid and efficient prediction of frequency-dependent inductance and resistance values. The proposed ML model offers a computationally fast and accurate alternative to analytical derivations or electromagnetic simulations, enabling scalable estimation across diverse transformer configurations.

1.5. THESIS ORGANIZATION

This thesis is divided into seven chapters, each building upon the previous to develop and validate an analytical framework for modeling the high-frequency behavior of power transformers.

- **Chapter 1** introduces the motivation, research objectives, and contributions of the thesis. It outlines the methodological framework and defines the scope and limitations of the work.

- **Chapter 2** provides a comprehensive review of transformer modeling techniques, with an emphasis on high-frequency behavior. It contrasts black-box, grey-box, and white-box approaches, highlighting the need for physically grounded analytical models.

- **Chapter 3** investigates the role of the magnetic core and conductor losses in the high-frequency behavior of transformer windings. Through numerical simulations and simplified geometries, it examines the conditions under which the core can be neglected and identifies the critical contribution of conductor eddy currents. The chapter lays the physical foundation for separating loss mechanisms in the modeling process.

Figure 1.6: The three-phase transformer used as a case study (with permission from Alliander N.V.).

- **Chapter 4** presents an analytical formulation for determining the frequency-dependent impedance of transformer windings. It models both the core-confined and leakage magnetic flux components, and describes how they affect self- and mutual impedances. The chapter details the derivation of field equations, their solutions, and the analysis of leakage magnetic flux effects via the magnetic vector potential. The impedance matrices are subsequently used for constructing the transformer's admittance matrix for wideband transient studies.

- **Chapter 5** validates the proposed modeling approach through three representative case studies, including single-phase and three-phase transformer configurations. The chapter demonstrates the model's ability to accurately capture high-frequency behavior and internal resonances through comparison with measured data. It also details the process of model order reduction, amplification factor analysis, and passivity enforcement, enabling implementation in EMT-based simulation software for transient analysis.

- **Chapter 6** introduces a machine learning-based approach to estimate the frequency-dependent impedance of transformer windings. It proposes a novel modeling framework that leverages localized geometric features to predict impedance values with high accuracy. The methodology addresses the challenges of input dimensionality and dataset diversity by reformulating the problem into fixed-size inputs. The trained model is validated against analytical solutions and experimental data, demonstrating significant improvements in computational efficiency and maintaining high accuracy over a wide frequency range.

- **Chapter 7** concludes the thesis by summarizing the key findings. The limitations are discussed accordingly, and some ideas are suggested for future research in the area of high-frequency transformer modeling.

2

OVERVIEW OF TRANSFORMER MODELING TECHNIQUES

> *The more you know, the more you realize how much you don't know.*
>
> Aristotle

This chapter provides a comprehensive review of transformer modeling techniques across different frequency ranges, with a particular focus on their application in electromagnetic transient studies. It begins by discussing the influence of the involved frequencies on model selection and highlights the modeling requirements for each frequency range. The chapter then explores high-frequency modeling approaches, including both lumped and distributed parameter methods, and distinguishes between black-box, grey-box, and white-box modeling methods. Special attention is given to the limitations of current high-frequency white-box models, particularly regarding the treatment of core effects and the separate computation of resistance and inductance. The review reveals a lack of consensus in the literature concerning the role of the transformer core at high frequencies. These unresolved challenges motivate the advanced analytical methods and modeling strategies proposed in the subsequent chapters.

2.1. INTRODUCTION

Efficient power transmission through electricity is a fundamental requirement of modern electrical networks. Since electrical energy is generated at relatively low voltages, transmission over long distances at these levels would result in excessive resistive losses. To mitigate these losses, power must be transmitted at high voltages, as higher voltage levels reduce current flow for a given power transfer, thereby minimizing resistive losses in transmission lines. Power transformers play a crucial role in this process by stepping up the voltage for efficient long-distance transmission and subsequently lowering it for safe distribution and end-use applications. Given that voltage levels change multiple times from the power plant to the distribution system, the total installed transformer capacity in a network is typically 8 to 10 times the generation capacity of power plants [36]. As a result, power transformers are among the most vital components of the power system. They are designed for long operational lifespans, often exceeding 30 years, necessitating continuous research in areas such as design, manufacturing, protection, modeling, maintenance, and diagnostics [36].

Transformers operate based on the principle of electromagnetic induction, as described by Faraday's law, which states that a change in magnetic flux causes an electromotive force (EMF) [37]. This principle is mathematically expressed as:

$$emf = -\frac{d\phi}{dt} \tag{2.1}$$

In its simplest form, an ideal transformer consists of two windings, primary and secondary winding wound on a common magnetic core, as illustrated in Figure 2.1. When an alternating voltage is applied to the primary winding, it generates a time-varying magnetic flux according to Faraday's law [36]:

$$\lambda_1 = \int_{t_0}^{t} V_1(t)dt + \lambda_1(t_0) \tag{2.2}$$

where λ_1 is the linkage flux and V_1 is the applied voltage. Since an ideal transformer has a perfect coupling, the flux generated by the first winding passes through the second winding. This flux, in turn, induces a voltage V_2 in the secondary winding following Faraday's law:

$$V_2 = \frac{\mathrm{d}\lambda_2}{\mathrm{d}t} \tag{2.3}$$

The relationship between the primary and secondary voltages and currents and the number of turns in each winding in an ideal transformer is given by the following.

$$\frac{V_1}{V_2} = \frac{N_1}{N_2} \tag{2.4}$$

$$\frac{I_1}{I_2} = \frac{N_2}{N_1} \tag{2.5}$$

where V_1 and V_2 are the primary and secondary voltages, and N_1 and N_2 are the number of turns in the primary and secondary windings, respectively.

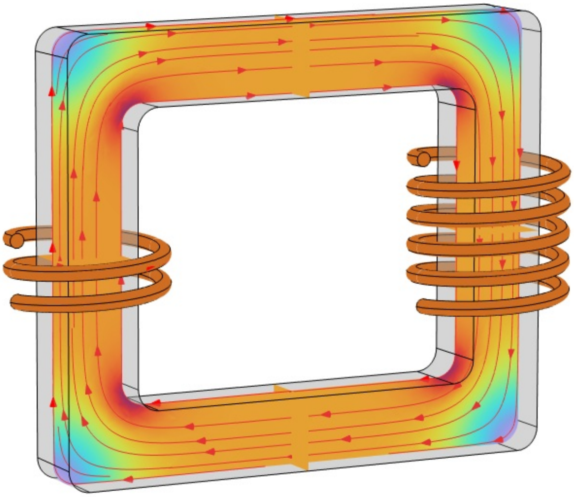

Figure 2.1: Schematic diagram of an ideal two-winding transformer.

An ideal transformer is characterized by the absence of core losses, meaning that both hysteresis and eddy current losses are zero. This implies infinite core resistance and a core material without hysteresis behavior. The winding conductors are assumed to have zero resistance, eliminating all winding losses. Additionally, the core has infinite relative permeability, which leads to zero magnetic reluctance and ensures that all magnetic flux is confined within the core. As a result, the entire magnetic flux links both windings, leading to zero leakage inductances and a coupling coefficient of unity. The magnetizing inductance is considered infinite, and thus no magnetic energy is stored. In addition, capacitances are assumed to be nonexistent, and the saturation flux density of the core is considered infinite [38].

Real-world transformers are far from perfect, and their behavior varies significantly across different frequency ranges, requiring models that can account for such variations. For example, steep-fronted overvoltages, such as those caused by breaker operations or nearby flashovers, require a model with a precise representation of the transformer's frequency-dependent input impedance [39]. Similarly, oscillating overvoltages, which can lead to resonant voltage buildup within the transformer windings, require models capable of accurately representing resonance and damping effects [39]. These complexities highlight the importance of selecting appropriate modeling approaches tailored to the specific application and frequency range of interest.

This chapter explores the various factors that influence transformer modeling, focusing on the high-frequency domain. Before delving into specific considerations for different applications, a general overview of transformer modeling approaches—white-box, black-box, and gray-box—will be provided. These approaches serve as the foundation for understanding how transformers can be represented in different scenarios, ranging from simplified models to highly detailed physical representations.

2.2. TRANSFORMER MODELING TECHNIQUES

Transformer modeling can be categorized into three primary approaches [35, 40]: white-box, black-box, and gray-box models. Each of these approaches differs in terms of complexity, required input data, and applicability to different studies. The following sections explore these modeling approaches, highlighting their strengths, limitations, and appropriate use cases.

2.2.1. WHITE-BOX MODELS

White-box models are detailed physics-based representations of transformers that rely on physical equations to describe the behavior of transformers. By explicitly modeling internal phenomena, white-box models provide a comprehensive and accurate depiction of transformer behavior [41]. The development of a white-box model requires detailed information about the transformer's design and materials [41, 42], including data on the core geometry, winding configurations, insulation properties, and material characteristics. Using these data, the governing equations are solved to predict the performance of the transformer under various operating conditions.

White-box models offer significant advantages. They provide deep physical insights into the internal behavior of transformers [41], enabling the study of complex phenomena such as resonance, and overvoltages within the transformers [42]. These models are suitable for system level analysis to study the interaction of transformers with the network, and designing stage [41, 43].

However, white-box models come with notable limitations. They are computationally intensive and require significant expertise in numerical modeling and simulation. The dependency on detailed design data poses challenges, as such information may be proprietary or unavailable [41], and inaccuracies in input data can compromise the model's reliability.

2.2.2. BLACK-BOX MODELS

Black-box models are a widely used approach for representing the terminal behavior of transformers. Unlike white-box models, which rely on detailed design data and physical equations, black-box models bypass the need for intricate knowledge of the transformer's internal structure and physical properties. Instead, these models are developed directly from measurement data obtained at the transformer terminals or data obtained from other models, e.g., white-box models [43]. They simplify the complexity of internal behaviors while ensuring sufficient accuracy for various applications. For example, system studies evaluating electrical stresses caused by lightning strikes, switching events, and short-circuit faults rely on electromagnetic transients (EMT) simulation tools such as PSCAD/EMTDC, EMTP, or ATP-EMTP. In these studies, the accuracy of the transformer model is essential to capture realistic voltage waveforms at the terminals [43]. Black-box models are particularly suitable for these scenarios due to their ability to accurately represent input impedance over a wide frequency range, making them valuable for both steady-state and transient studies [43, 44].

However, black-box models are subject to certain constraints. They lack interpretability, as they do not provide information on internal behavior or physical phenomena within the transformer, which makes them unsuitable for tasks such as transformer design or detailed diagnostics [43]. Furthermore, black-box models are heavily based on accurate and high-quality measurement data [43]. Any errors or limitations in the measurements can significantly impact the accuracy and reliability of the model. Furthermore, these models are context-specific, which means that they are only valid within the range of conditions for which measurements were taken [41]. For example, a high-frequency model designed to represent leakage inductance under short-circuit conditions cannot accurately capture the open-circuit behavior of the transformer [41]. This limitation arises because the model parameters are derived for a specific operating condition using the corresponding measurements. As a result, separate black-box models must be developed for different scenarios. An alternative approach is to combine multiple methods using special techniques, such as filters [45]. It should be noted that black-box models are predominantly applied in mid- and high-frequency applications and are not commonly used to represent low-frequency transients [41].

2.2.3. GRAY-BOX MODELS

Gray-box models aim to bridge the gap between black-box and white-box approaches [42]. These models incorporate physical meaning and structure while relying on terminal measurements to estimate key parameters, making them a hybrid approach that balances physical insight with practical feasibility [46]. Unlike white-box models, which require detailed design data, gray-box models derive their topology and structural components based on physical principles while estimating model parameters such as saturation inductance obtained from measured data, similar to black-box models [41].

Gray-box models have gained increasing interest among transformer modelers due to their ability to overcome the limitations associated with restricted access to transformer construction and material information [41]. Using measurement-based parameter estimation, they provide a practical and often fairly accurate alternative to purely physical or purely empirical modeling approaches. However, the main challenge remains in accurately estimating model parameters based on terminal measurements, which requires advanced identification techniques and optimization methods [41, 47].

2.3. TRANSFORMER MODELS BASED ON APPLICATION

After discussing various transformer modeling approaches, the next step is to examine their application in different transient studies. The level of detail and complexity required in a transformer model depends on the specific transient phenomenon under investigation. Selecting an appropriate transformer model is essential, as not all parameters are relevant for every study. For instance, capacitive effects may be insignificant in certain transient analyses but become critical in others, such as ferroresonance studies. Similarly, the representation of the iron core can vary from a simple inductive model to a detailed dynamic hysteresis model, depending on the study's objectives [41].

Choosing a suitable transformer model ensures that transient behaviors are accurately represented, enhancing the reliability of system analysis and the effectiveness of protective measures. Thus, understanding the diverse nature of transients in power systems is crucial for selecting an appropriate transformer model. These transients can vary significantly in terms of duration and frequency content. The following section provides an overview of these classifications and discusses their implications for transformer modeling.

2.3.1. CLASSIFICATION OF TRANSIENT PHENOMENA

As mentioned, the accuracy and complexity of the electromagnetic model depend largely on the specific objectives of the study. One of the key factors influencing the level of detail is the frequency range of interest. In other words, the selection of component models should be based on the frequency range of the transients under investigation. Table 2.1 represents transients in power systems classified into four groups, depending on the nature and duration of the change [12]. However, the exact frequency range of a given test case is often unknown before the simulation. This challenge can be addressed by referring to widely accepted classification tables, which provide general frequency ranges for various transient phenomena. Table 2.2 presents a concise summary of common transient events [12].

Table 2.1: Classification of Frequency Ranges

Group	Frequency Range	Shape Designation
I	0.1 Hz - 3 kHz	Low-Frequency Oscillation
II	50/60 Hz - 20 kHz	Slow-Front Surges
III	10 kHz - 3 MHz	Fast-Front Surges
IV	100 kHz - 50 MHz	Very Fast-Front Surges

Table 2.2: Origin and Frequency Range of the Transients in Power Systems

Origin	Frequency range
Ferroresonance	0,1 Hz to 1 kHz
load rejection	0,1 Hz to 3 kHz
Fault clearing	50 Hz to 3 kHz
Line switching	50 Hz to 20 kHz
Transient recovery voltage	50 Hz to 100 kHz
Lightning overvoltages	10 kHz to 3 MHz
Switching in GIS	100 kHz to 50 MHz

2.3.2. LOW- AND MID- FREQUENCY MODELS

Most transformer models implemented in electromagnetic transient simulation tools are primarily designed for low- and mid-frequency transients, typically for phenomena occurring well below the first winding resonance, which is generally in the kilohertz range [48]. These models are adequate for analyzing events such as line switching, harmonic interactions, ferroresonance, controller interactions, and short-circuit transients. They are also used to study magnetic saturation phenomena, including inrush currents and geomagnetically induced currents (GIC) [36, 41, 48, 49].

The proposed transformer models for low- and mid- frequencies can be categorized into three main groups: terminal-based (or matrix) models, topology-based models, and hybrid models [36]. This section explores the fundamental principles behind each modeling approach, highlighting their advantages and limitations.

TERMINAL (MATRIX)-BASED MODELS

In this category, the focus is on the voltage and current at the winding terminals, treating the transformer as a black box component [36]. Only the equations governing the relationship between terminal voltages and currents are required [36]. These models are typically represented mathematically as matrices using circuit elements such as self- and mutual inductances, ideal transformers, and resistances [36]. They are suitable for linear and short-circuit studies, with model parameters often derived from short-circuit tests [36]. The most common model of this category, BCTRAN routine, was first introduced by [50] and is implemented in EMTP software. BCTRAN model is based on the following equation [51]:

$$V = ZI \tag{2.6}$$

In which V is the terminals' voltage, I is the windings' current, and Z is the impedance matrix. For transient calculations, Equation (2.6) must be reformulated as:

$$v = Ri + L\frac{di}{dt} \tag{2.7}$$

where R and L represent the real and imaginary components of Z, respectively, and can be derived from excitation tests. This approach accounts for phase-to-phase coupling and models terminal characteristics; however, it does not differentiate between core or winding topology, as all core designs are treated identically in the mathematical formulation [51].

A potential limitation of this method is that the branch impedance matrix Z may become ill-conditioned for very small excitation currents or when these currents are completely neglected [52]. Additionally, short-circuit impedances are not well represented in this approach [51], due to the strong coupling between windings. To address these issues, an admittance matrix representation is often preferred:

$$I = YV \tag{2.8}$$

where the admittance matrix Y always exists and its elements can be directly obtained from standard short-circuit tests.

These models are inherently linear [51]. However, for many transient studies, it is necessary to account for saturation and hysteresis effects. Excitation current effects can be linearized within the matrix formulation, but this may introduce errors when the core saturates. Alternatively, excitation can be excluded from the matrix and modeled externally at the transformer terminals using nonlinear elements [51], see Figure 2.2. Although since the placement of the core model within the equivalent circuit is arbitrary, this can lead to inaccuracies in applications where precise core representation is essential, such as transformer energization [48].

It is worth mentioning that while these models are theoretically valid only at the frequency at which the nameplate data were obtained, they remain reasonably accurate for frequencies up to 1 kHz [51].

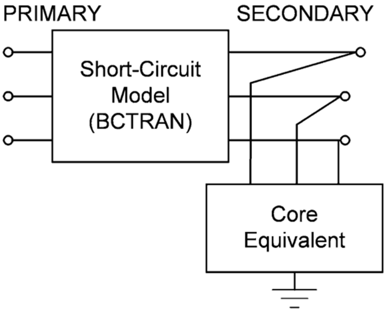

Figure 2.2: Basic BCTRAN-based model of a two-winding transformer with an externally represented core [51].

TOPOLOGY-BASED MODELS

Unlike terminal-based models, these models are derived from the transformer's magnetic circuit. In this approach, the placement of the core within the circuit is explicitly defined. Additionally, each inductor representing the core corresponds directly to a specific section of the core, ensuring that its nonlinear characteristics are accurately incorporated [48]. The key challenge lies in accurately determining the magnetic flux paths, as the model's accuracy heavily depends on the assumptions made about these paths [36]. In regions with high-permeability magnetic cores, defining flux paths is relatively straightforward. However, in areas with low permeability or under deep saturation, achieving an accurate representation becomes significantly more challenging [36].

The development of topology-based models generally involves two main steps: first, constructing a magnetic equivalent circuit of the transformer, and second, coupling the magnetic circuit to an external electrical circuit. This coupling establishes the relationships between currents, voltages, and magnetomotive forces. These relationships can be classified into two main approaches: duality-based and geometric methods [36, 51].

Duality based methods: The principle of duality is a well-established and physically accurate method to derive circuit-based models of power transformers. Originally introduced by Cherry [53] and later extended by Slemon to incorporate nonlinearities [54], this approach enables the inclusion of key transformer behaviors and phenomena, such as core saturation in individual legs, interphase magnetic coupling, and leakage flux interactions [51]. Duality-based models effectively capture the distribution of magnetic flux within both the core and windings, making them valuable for analyzing the electromagnetic behavior of transformers [55].

In this approach, windings are represented as magnetomotive force (MMF) sources, leakage paths as linear reluctances, and the magnetic core as saturable reluctances [51]. The node and mesh equations of the magnetic circuit directly correspond to the dual node and mesh equations in the electrical equivalent circuit [51]. To enhance practical applicability, the current sources resulting from the transformation are replaced with ideal transformers. This substitution ensures primary-to-secondary isolation while preserving the turns ratio [51]. Figure 2.3 illustrates the equivalent circuit of a single-phase shell-form transformer with concentric windings, derived using this methodology [51].

Geometric models: Unlike models based on the duality principle, geometric models utilize an inductance matrix to establish the coupling between magnetic and electrical circuits [36]. This inductance matrix is determined based on the core topology [36, 51]. In the presence of a nonlinear core, the inductance matrix must be updated at each time step to account for changes in permeability. Additionally, in geometric models, the magnetic and electrical components of the transformer remain decoupled, making them computationally distinct [36].

It should be noted that for low-frequency transients, where transformer's behavior significantly impacts system performance, topology-based models are generally superior to matrix-based models. Topology-based models offer a more accurate representation of the physical structure and internal interactions within the transformer, making them particularly effective for detailed transient analyses in this frequency range [48].

HYBRID MODELS

The fundamental concept of hybrid models is to enhance the representation of leakage inductance by incorporating both the transformer's

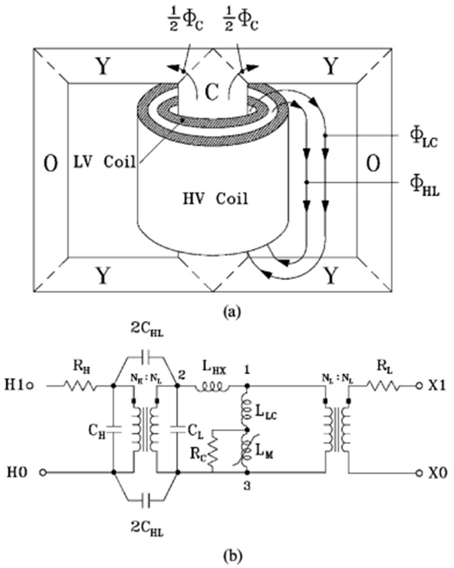

(a)

(b)

Figure 2.3: Duality-derived model for a single-phase shell-form transformer. (a) Core design. (b) Equivalent circuit [51].

topology and core nonlinearity [36]. This is achieved by coupling an equivalent circuit of the core, derived using the duality principle, with a leakage inductance model [36]. The approach relies on the assumption that core inductances are significantly higher than leakage inductances, meaning that the linkage flux primarily closes through the core, with leakage inductance remaining unaffected by core permeability [36]. However, this assumption does not hold under saturation, where core permeability decreases, affecting the leakage flux. To account for this, hybrid models represent core and leakage inductances separately, connecting them at their terminals to maintain accuracy for different operating conditions [36].

2.3.3. TRANSFORMER MODELS FOR HIGH FREQUENCIES

The behavior of a transformer at high frequencies differs significantly from its low-frequency characteristics. As frequency increases, phenomena such as skin and proximity effects, dielectric losses, resonances in windings, and capacitive effects become dominant, necessitating more sophisticated modeling approaches.

High-frequency transformer models aim to capture these intricate behaviors to ensure accurate analysis of fast transients. Unlike low-frequency models, which primarily consider inductive and resistive components, high-frequency models must incorporate additional capacitive components in the transformers to simulate their behavior in the frequency range of interest.

The selection of an appropriate high-frequency model depends on the specific study, particularly whether the focus is on the internal electromagnetic behavior of the transformer or only on its terminal response. Some applications, such as insulation design, require detailed internal modeling, while others, such as system-level transient studies, may only need an accurate representation of terminal characteristics.

In the following sections, various high-frequency modeling techniques will be explored. Each method offers different levels of complexity and accuracy, making them suitable for different types of high-frequency phenomena and engineering applications.

WHITE-BOX MODELS

High-frequency white-box (WB) or detailed models of transformers provide insights into both external and internal overvoltages, making them essential for analyzing high-frequency transient phenomena. These models rely on detailed transformer design data, including geometry and material properties, to accurately represent the transformer's electromagnetic behavior [56].

White-box models can be broadly classified into lumped-parameter circuit models and distributed parameter models. Lumped parameter models use spatial discretization of the windings to approximate the transformer's behavior, while distributed parameter models adopt a traveling wave approach. In all cases, model parameters are derived through analytical formulations and/or numerical methods, ensuring a physically consistent representation of the transformer's high-frequency response [56].

Lumped-parameter model: The most common approach to obtain a detailed transformer model is based on lumped-element parameters [56]. In this method, the transformer winding is subdivided into smaller sections, which can represent a single turn, multiple turns, a disk, or a group of disks, depending on the required level of detail [42]. The length of these sections directly determines the highest frequency for which the model remains valid. In practice, this corresponds to a few megahertz for large power transformers, depending on the design and discretization level.

Each section is then represented using fundamental circuit elements, such as inductances, capacitances, and resistances, to account for the electrical and magnetic interactions within the windings. Finally, all sections are interconnected to form a complete transformer model that accurately captures its high-frequency behavior [42, 56]. Figure 2.4 represents the detailed transformer model obtained in this way, where

L_{hv} and L_{lv} represent the self-inductances of the high-voltage (HV) and low-voltage (LV) winding sections, respectively. M_{ij}, M_{in}, and M_{jn} denote the mutual impedance between these winding sections and other parts of the transformer. Notably, the term *mutual impedance* is used instead of *mutual inductance* since it accounts for both inductive and resistive components of the interaction between sections, and the resistive term arises from eddy losses. The conductor resistances of the HV and LV windings are represented by R_{hv} and R_{lv}. Capacitive effects are also included in the model: C_{hv} and C_{lv} represent the capacitances of the HV and LV winding sections, while C_{hl} accounts for the coupling capacitance between HV and LV sections. Additionally, C_{hg} and C_{lg} represent the capacitances between the HV winding and the tank, and between the LV winding and the core, respectively. In Figure 2.4, the capacitances to ground and between windings are divided between the beginning and end of each section. When consecutive sections are interconnected, these half-capacitances form parallel pairs, which effectively result in the capacitances illustrated in the figure.. For the sake of simplicity, the conductances are not represented in the figure, but they should be accounted for if they are not negligible.

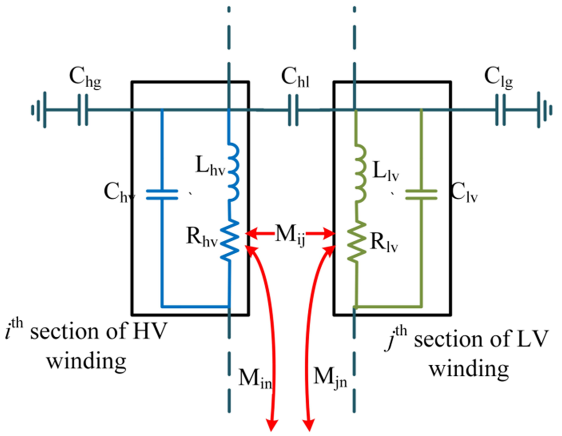

Figure 2.4: An illustration of a transformer model.

Distributed-parameter methods In the lumped parameter method, the finest possible discretization is at the level of individual turns. However, when the wavelength of the signal becomes comparable to the length of these sections, the lumped parameter approach loses its validity. This limitation is particularly evident in scenarios involving very fast-front transients, such as those caused by gas-insulated substation (GIS) switching operations [56], where a traveling wave modeling approach becomes necessary for accurate representation.

In such cases, the transformer can be modeled using the well-known Telegrapher's equations for a single-phase transmission line (STL) [48]. The Telegrapher's equations in the Laplace domain are given as [48, 57, 58]:

$$-\frac{\mathrm{d}V}{\mathrm{d}x} = (R + j\omega L)I = ZI \tag{2.9}$$

$$-\frac{\mathrm{d}I}{\mathrm{d}x} = (G + j\omega C)U = YU \tag{2.10}$$

where V and I represent the voltage and current at position x along the winding, and Z and Y denote the series impedance and shunt admittance per unit length, respectively. By solving Equations (2.9) and (2.10), the voltage distribution within the transformer windings can be determined.

However, the STL model does not account for the mutual inductance between turns of a winding, which can be significant when computing inter-turn voltages under fast-front incident impulses [48]. To overcome this limitation, a multiconductor transmission line (MTL) model can be applied, as illustrated in Figure 2.5. In this model, continuity is preserved by topologically connecting the end of each conductor to the beginning of the next conductor [48, 59], which is expressed as:

$$v_{ri} = v_{s(i+1)}, \quad i_{ri} = -i_{s(i+1)}, \quad i = 1, 2, \ldots, n-1 \tag{2.11}$$

The Telegrapher's equations for the MTL model are given by:

$$-\frac{\mathrm{d}V}{\mathrm{d}x} = ZI \tag{2.12}$$

$$-\frac{\mathrm{d}I}{\mathrm{d}x} = YI \tag{2.13}$$

where Z and Y are $N \times N$ matrices representing the series impedance and shunt admittance per unit length, and N is the number of conductors (turns or discs). The vectors V and I represent the voltages and currents at position x along the winding.

For very fast transients, it may be necessary to model all individual turns. Applying a full MTL model can be computationally expensive in such a case [60]. To mitigate these computational challenges, a hybrid approach combining the STL and MTL models can be employed [56, 60, 61]. In this approach, the STL model is first used to determine the voltages at coil connection points, followed by the application of the MTL model to compute the voltage distribution within each coil section [56, 59, 60].

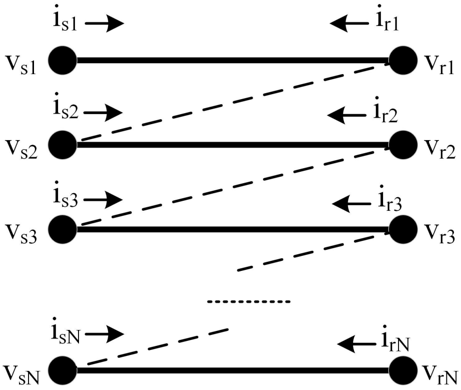

Figure 2.5: Multiconductor Transmission Line Model for the Transformer Winding.

BLACK-BOX MODELS

High-frequency black-box models aim to accurately represent the transformer's response as observed from its external terminals within a defined frequency range [56]. These models are particularly useful for system-level studies where internal transformer details are not required, and only terminal behavior is of interest. System studies involving black-box transformer models are essential for evaluating electrical stresses caused by lightning strikes, switching events, and short-circuit faults. The results of these studies inform the selection of insulation levels for electrical equipment, as defined by IEC and IEEE standards. To achieve realistic voltage waveforms at transformer terminals, the applied transformer model must [42, 43]:

- have a sufficiently accurate input impedance to capture the damping effect on steep-fronted incoming waves and oscillating voltages.
- maintain accuracy at 50/60 Hz to enable proper initialization of steady-state conditions in simulations.

Considering the transformer as a linear time-invariant (LTI) component, the relationship between the voltage and current at its terminals can be expressed in the frequency domain as:

$$I(f) = Y(f)V(f) \tag{2.14}$$

where f is the frequency, $I(f)$ and $V(f)$ are the vectors of currents and voltages at the transformer terminals, respectively, and $Y(f)$ is the admittance matrix of the transformer, which describes its electrical behavior over a range of frequencies.

The most accurate approach to obtain $Y(f)$ is through direct frequency response measurements of the transformer. However, it can also be derived from frequency response data obtained using detailed white-box models [42, 43].
For the n-terminal transformer shown in Figure 2.6, the elements of the i^{th} row of the admittance matrix can be determined by applying a voltage source to terminal i while keeping all other terminals short-circuited. The admittance elements are then calculated as follows:

$$Y_{ii} = \frac{I_i}{V_i}, \quad Y_{ij} = \frac{I_i}{V_j} \tag{2.15}$$

where Y_{ii} represents the self-admittance of terminal i, and Y_{ij} represents the mutual admittance between terminals i and j.

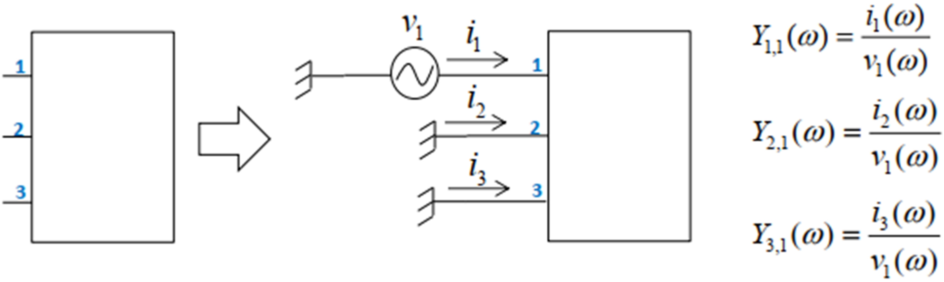

Figure 2.6: Schematic of an n-terminal transformer used for admittance matrix determination [43].

After obtaining the frequency response data, a mathematical model should be developed to represent the transformer's behavior. One common approach is the state-space model, as shown in Equation (2.16) [43]:

$$Y_{meas}(\omega) \simeq Y = C(\mathrm{j}\omega I - A)^{-1}B + D \tag{2.16}$$

where $A(n \times n)$ is the system dynamics matrix, $B(n \times m)$ is the input matrix, $C(l \times n)$ maps the internal states to the outputs, and $D(l \times m$ directly relates the inputs to the outputs. Here, n denotes the number of state variables, m the number of inputs, and l the number of outputs. Another widely used technique is the pole-residue model, which can be expressed as [43]:

$$Y_{\mathrm{meas}}(\omega) \simeq Y = \sum_{i=1}^{N} \frac{R}{\mathrm{j}\omega - a_i} + D \tag{2.17}$$

One of the most effective techniques for estimating the parameters of these mathematical models is the vector fitting (VF) method. The details of this method are provided in [43, 62–65]. These expressions are then structured for integration into circuit solvers through one of the following methods:

- Equivalent circuit representation using lumped RLC parameters [28, 30, 66],
- Direct implementation as a state-space model for numerical simulation [67, 68].

Additional details on how to obtain these models and examples using them for transient studies can be found in [45, 69–71].

GRAY-BOX MODELS

As mentioned before, grey-box (GB) models represent a balance between white-box models, which rely on design data, and black-box models, which are purely measurement-based. The core idea behind grey-box modeling is to establish a topologically correct transformer representation and then tune its parameters to fit frequency response measurements [46]. This approach enables a physically meaningful model while using measurement data for accuracy [46]. High frequency gray-box models are typically based on ladder networks, as shown in Figure 2.7, and require rigorous fitting procedures [72, 73]. These models can approximate internal winding responses at high frequencies but might not be suitable for low-frequency studies [46].

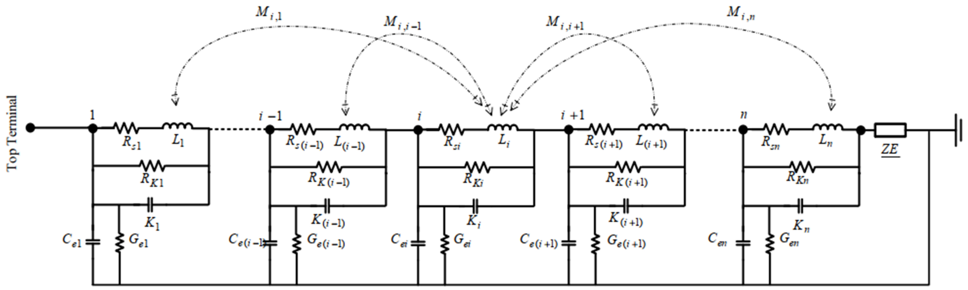

Figure 2.7: Ladder network topology of a transformer.

As this thesis focuses on the white-box modeling of power transformers, the following section provides an overview of the common approaches used to determine the parameters of such models.

2.4. PARAMETER DETERMINATION FOR WHITE-BOX MODELS

As previously discussed, the white-box modeling approach represents the transformer using inductances, resistances, and capacitances derived from its physical structure. The accurate determination of these parameters is crucial for modeling high-frequency behavior precisely.

The following sections explore the most commonly used methods for parameter determination, highlighting their applications and limitations.

2.4.1. INDUCTANCE CALCULATION

In the equivalent circuit of a transformer, the magnetic behavior is represented by self- and mutual inductances. Due to the eddy currents induced in the conductors and core, the inductance of the windings varies with frequency, typically decreasing as frequency increases. This reduction occurs more evidently when the frequency reaches a point where the skin depth of the magnetic flux becomes comparable to the dimensions of the conductors and the laminated sheets of the core.

Before delving into inductance calculations, it is important to consider the influence of the iron core on inductance values at high frequencies. Due to its high permeability, the iron core significantly affects inductance values at low frequencies. However, at high frequencies, many researchers have concluded that the magnetic flux does not penetrate the core due to the very small skin depth [74, 75]. The skin depth, which describes the extent to which magnetic flux and eddy currents penetrate a conductor [38], is given by:

$$\delta = \sqrt{\frac{2}{\omega\mu\sigma}} \tag{2.18}$$

where σ is the electrical conductivity of the material, ω is the angular frequency, and μ is the permeability of the material.

Since the cores of power transformers are made of materials with high magnetic permeability and electrical conductivity, the resulting skin depth for each laminated sheet at high frequencies becomes extremely small. For instance, the skin depths in iron are approximately 0.35 mm at 50 Hz and 7 nm at 100 kHz. Given that typical lamination thicknesses range between 0.1 mm and 0.3 mm, many studies have concluded that magnetic flux penetration into the core is negligible at high frequencies and modeled the transformer as an air-core component. Moreover, the limited flux penetration implies that the core can be effectively treated as a magnetic flux barrier at high frequencies. On the other hand, some researchers have demonstrated that the equivalent complex permeability of the core remains significant even at frequencies as high as 1 MHz [76]. This indicates that the skin depth may not be negligible and suggests that the effects of the core at high frequencies cannot be ignored.

Consequently, various approaches have been proposed for calculating inductances for high-frequency transformer models, each based on different assumptions regarding the role of the magnetic core. These approaches can be categorized as follows:

1. **Air-core approximation** ($\mu = 1$): Assumes the absence of the core, modeling the transformer as an air-core structure.
2. **Finite permeability core**: Takes into account the actual permeability of the core material.
3. **Core as a magnetic shield** ($\mu = 0$): Treats the core as a perfect magnetic shield, completely preventing magnetic flux penetration.

The following sections provide an overview of each approach, discussing their assumptions, applicability, and limitations in the context of high-frequency transformer modeling.

AIR-CORE APPROXIMATION

The simplest and most common approach to modeling a transformer core is to completely neglect its presence [56]. For the two coils shown in Figure 2.8, the mutual inductance can be determined by solving Maxwell's equations. The expression for this case is given by [16, 74]:

$$M_{12} = \frac{\mu_0}{4\pi} \oint_{C_1} \oint_{C_2} \frac{\mathrm{d}\vec{s}_1 \cdot \mathrm{d}\vec{s}_2}{R_{12}} \tag{2.19}$$

where μ_0 is the permeability of free space, $\mathrm{d}\vec{s}_1$ and $\mathrm{d}\vec{s}_2$ are differential elements along the paths of coils C_1 and C_2, respectively, and R_{12} is the distance between these differential elements.

For circular thin wires, Equation (2.19) leads to the following closed-form expression for mutual inductance [74]:

$$M_{12} = \frac{2\mu_0\sqrt{r_1 r_2}}{\sqrt{k'}}\left[K(k') - E(k')\right] \tag{2.20}$$

where

$$k' = \frac{1-\sqrt{1-k^2}}{1+\sqrt{1-k^2}} \tag{2.21}$$

$$k = \sqrt{\frac{4 r_1 r_2}{(r_1+r_2)^2 + d^2}} \tag{2.22}$$

In Equations (2.21) and (2.22), K and E represent the complete elliptic integrals of the first and second kind, respectively. The variables r_1 and r_2 denote the radii of the two coils, and d is the axial distance between their centers. Lyle's method can be employed to calculate the mutual inductance between coils with rectangular cross-sections. The simplest form of Lyle's method is that each coil is approximated by two thin-wire circular coils. The placement of these equivalent coils depends on the conductor construction [77].

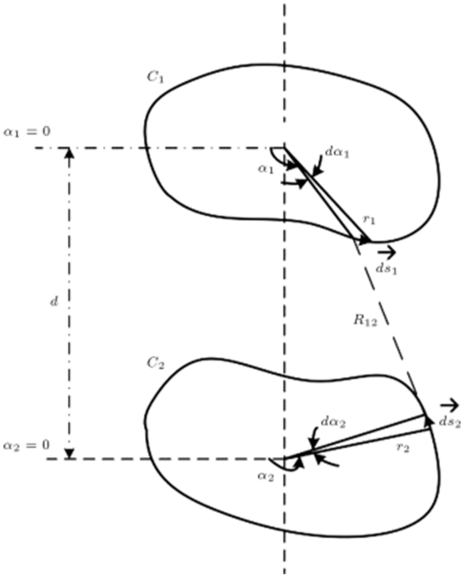

Figure 2.8: Two parallel thin wires [78].

The self-inductance of the turn showed in the Figure 2.9 can be computed as follows [74]:

$$L = R(\ln(\frac{8R}{GMD} - 2) \tag{2.23}$$

in which, GMD is the geometric mean distance and is defined as:

$$\begin{aligned}\ln(\frac{GMD}{\sqrt{a^2+b^2}}) = \frac{2b}{3a}\tan^{-1}\frac{a}{b} + \frac{2a}{3b}\tan^{-1}\frac{b}{a} \\ - \frac{b^2}{12a^2}\ln(1+\frac{a^2}{b^2}) - \frac{a^2}{12b^2}\ln(1+\frac{b^2}{a^2}) - \frac{25}{12}\end{aligned} \tag{2.24}$$

This approach provides reasonable accuracy when the two coils are similar in structure and when the main dimensions of their cross-sections are comparable to the average radius of the coil. In [79], the authors propose a unified formula for calculating both self- and mutual-inductance without restrictions on the coil dimensions. In Equation (2.20) and Equation (2.23), the frequency dependency of inductances due to eddy currents in the conductors is neglected. This can lead to different characteristics at high frequencies. To address this limitation, [80] proposes a combined analytical and finite element method (FEM) approach for parameter estimation, incorporating the effects of eddy currents circulating in the conductors.

The air-core assumption significantly underestimates the power frequency impedance of the transformer compared to its actual value. This discrepancy leads to inaccurate initial conditions in transient studies, potentially affecting the reliability of the analysis.

MAGNETIC SHIELDING

Some researchers have concluded that, when subjected to very fast front transients, the penetration of magnetic flux into the transformer core becomes negligible [25, 81], effectively causing the core to act as a magnetic insulating barrier. This phenomenon is illustrated in Figure 2.10. As a result, conventional air-core approximations tend to overestimate inductance values, particularly within the core window, leading to substantial modeling errors [25, 81].

To address this limitation, several studies have incorporated the shielding effect of the core into inductance calculations. A common solution involves modifying air-core inductance expressions using analytical techniques that account for the exclusion of magnetic flux by the core [25, 81]. These approaches employ a multilayer image method to refine the inductance calculation. The resulting expressions are computationally efficient and demonstrate high accuracy, as verified through comparison with finite element method (FEM) simulations. In addition to analytical approaches, FEM-based methods have also been investigated. For instance, [31] utilized a two-dimensional axisymmetric model to compute the per-unit-length inductance matrix of transformer windings.

FINITE PERMEABILITY

Several studies have demonstrated that the presence of an iron core significantly influences transformer behavior at high frequencies, challenging the common assumption that magnetic flux does not penetrate the core under such conditions. For example, in [82] and [83] it was discussed that the transformer core plays a crucial role in damping transient overvoltages, with inductance values remaining influential even beyond 1 MHz. Findings in [76] further support this view, showing that the effective complex permeability of power transformer

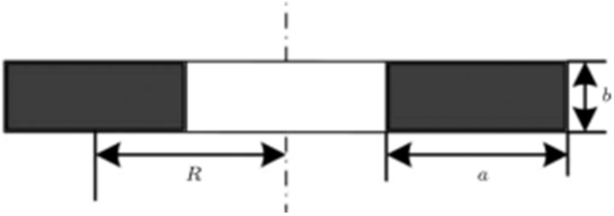

Figure 2.9: Parameter determination of a single turn [78].

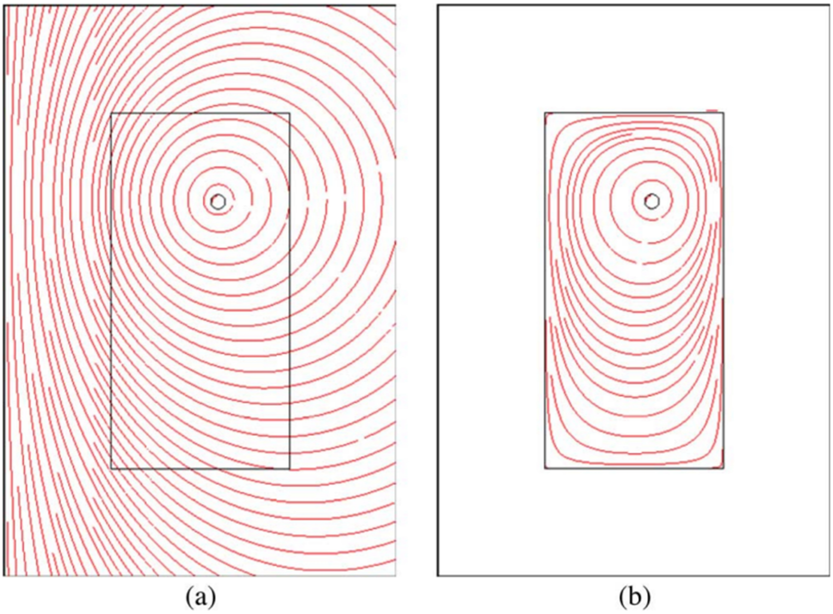
(a)
(b)

Figure 2.10: Magnetic flux distribution at 10 MHz. (a) Air core. (b) Iron core [81]

cores remains substantial at frequencies up to 1 MHz. Similarly, [84] asserted that the magnetic core cannot be neglected at frequencies above 10 kHz. Experimental studies reinforce these conclusions, indicating that inductance values deviate significantly from air-core approximations when an iron core is present, even at frequencies as high as 1 MHz [56].

Therefore, an alternative approach for inductance calculations involves explicitly accounting for finite permeability in transformer models. Several studies have proposed efficient methods to incorporate these effects. In [19], self- and mutual-impedance calculations for coils on ferromagnetic cores were examined, taking into account eddy current losses in the core. However, this study assumed a uniform current distribution in the conductors, which limits accuracy for scenarios with significant skin and proximity effects. To overcome these limitations, other researchers [28, 83, 85] employed FEM-based approaches to calculate inductance and resistance parameters more accurately. These studies utilized the concept of complex permeability to approximate eddy current losses in conductive materials without requiring an excessively fine mesh. This approach improves computational efficiency while preserving modeling accuracy.

2.4.2. RESISTANCE CALCULATION

At high frequencies, the resistive losses in transformers are beneficial as they contribute to damping transient voltage responses, thereby reducing the associated voltage oscillations [56]. Typically, transient voltage oscillations are underdamped, and the introduction of resistance not only decreases their magnitude but also slightly lowers their oscillation frequency [56].

In high-frequency transformer models, resistance values account for winding and core losses. Conductance, on the other hand, represents dielectric losses within the transformer structure [56].

DIELECTRIC LOSSES

The frequency-dependent dielectric losses can be represented by the concept of complex permittivity, as described in [56]. The complex permittivity of a dielectric medium ϵ^* can be expressed as follows [86, 87]:

$$\epsilon^*(\omega) = \epsilon_0 \epsilon_r^*(\omega) = \epsilon_0(\epsilon_r^{'}(\omega) - j\epsilon_r^{''}(\omega)) \tag{2.25}$$

where ϵ_0 denotes the vacuum permittivity, while $\epsilon_r^{\prime}$ and $\epsilon_r^{\prime\prime}$ represent the real and imaginary parts of the permittivity, respectively.
Consequently, the dielectric conductance can be computed using [56]:

$$G(\omega) = \omega \tan\delta \epsilon_r^{'} C_0 \tag{2.26}$$

where C_0 is the geometric capacitance calculated assuming vacuum conditions, and $\tan\delta$ denotes the dissipation factor of the dielectric material, defined as:

$$\tan\delta = \frac{\epsilon_r^{''}(\omega)}{\epsilon_r^{'}(\omega)} \tag{2.27}$$

WINDING LOSSES

Winding losses significantly contribute to the overall energy losses in magnetic components. Eddy currents generated within the conductors cause winding losses to increase substantially at higher frequencies [88]. To accurately determine these losses, several approaches are available, including analytical, empirical, and numerical methods. Among these methods, FEM stands out as it can yield highly accurate results, allowing detailed winding loss calculations for various configurations. However, FEM requires extensive computational resources, as accurate results typically demand mesh element sizes approximately one-third of the skin depth within the conductor [88]. Consequently, FEM becomes computationally intensive, especially at higher frequencies. In contrast, analytical and empirical methods offer more efficient computational alternatives. These approaches are widely utilized due to their ability to quickly estimate winding losses without the substantial computational requirements associated with FEM.

Eddy current phenomenon in conductors manifest itself as two distinct effects: the skin effect and the proximity effect. The skin effect arises due to the conductor's own current, where the induced magnetic field causes the current density to become non-uniform and increasingly concentrated near the conductor's surface at higher frequencies [38]. In contrast, the proximity effect results from the interaction with magnetic fields generated by currents flowing through neighboring conductors, similarly causing uneven current distribution within the conductor [38]. An important concept in calculating the increase in winding losses due to eddy currents is the orthogonality between skin and proximity effects. This orthogonality permits the independent calculation of losses associated with each effect [38, 88].

Skin Effect Skin effect losses in conductors with rectangular cross-sections can be estimated using the formulation proposed by Lammeraner and Stafl [56, 89]:

$$R_{\mathrm{skin}}(\omega) = \mathrm{Re}\{R_{DC}\,\zeta \coth \zeta\} \tag{2.28}$$

where

$$\zeta = b\sqrt{\mathrm{j}\omega\mu\sigma} \tag{2.29}$$

In Equations (2.28) and (2.29), R_{DC} represents the DC resistance per unit length of the conductor, ω is the angular frequency, b denotes half of the conductor's thickness (radial dimension), μ is the permeability, and σ is the conductivity of the conductor material.
However, if the conductor has a large height-to-width ratio (axial-to-radial dimensions), Equation (2.28) tends to underestimate the skin effect losses. In such scenarios, a more accurate estimation can

be achieved by approximating the conductor's cross-section with an equivalent circular shape and applying an equation based on Bessel functions [56]:

$$R_{\mathrm{skin}}(\omega) = \mathrm{Re}\{R_{DC}\, m \frac{I_0(mr)}{I_1(mr)}\} \tag{2.30}$$

where r is the equivalent circular radius of the conductor, I_0 and I_1 are modified Bessel functions of the first kind of order zero and one, respectively, and m is defined as:

$$m = \sqrt{\mathrm{j}\omega\mu\sigma} \tag{2.31}$$

Proximity Effect The increase of resistance due to the proximity effect is given by [56, 89]:

$$R_{prox}(\omega) = \mathrm{Re}\{\mathrm{j}\omega \frac{\tanh \zeta}{\zeta} L_0\} \tag{2.32}$$

In Equation (2.32), L_0 is the average inductance accounting for induced currents due to adjacent conductors, and ζ is defined in Equation (2.29). At higher frequencies, the proximity effect losses between two turns can be approximated by [56]:

$$R_{prox}(\omega) = \sqrt{\frac{2\omega}{\mu\sigma d^2} L_{air}} \tag{2.33}$$

where L_{air} is the leakage inductance between turns, and d is the insulation thickness.

Empirical Formulas Apart from analytical and numerical methods, the resistance of transformer winding sections at high frequencies can also be estimated using empirical approaches. Two widely recognized methods are the *K-Factor* and *D-Factor* approaches [56].

In the K-Factor method, a constant multiplier—referred to as the K-Factor—is applied to all DC resistance values to approximate their frequency-dependent behavior. This approach is straightforward to implement. However, its main limitation lies in the fact that it modifies all resistances uniformly with a single constant, which means that accurate damping can only be achieved for one dominant oscillatory frequency [56, 77]. In practice, different resonance frequencies can exist within the transformer, typically ranging from tens to hundreds of kilohertz. As a result, the K-Factor method may fail to accurately capture the frequency-dependent nature of losses across the entire system. Typical K-Factor values range from 1500 to over 3000, depending on the specific dominant frequency being targeted for damping [56].

The D-Factor method, on the other hand, is based on empirical data collected by Fergestad from 25 power transformers of varying sizes [56]. The procedure for implementing this method is as follows [56, 90]:

1. The eigenvalues and eigenvectors of the undamped white-box transformer model are computed.
2. The real parts of the eigenvalues, denoted as α_i, are then assigned according to an experimentally derived relationship between the real part α_i and the imaginary part $\omega_i = 2\pi f_i$ of the eigenvalues:

$$\frac{\alpha_i}{\omega_i} = -0.022 - 0.058 \times 10^{-6} \times \omega_i \quad \text{for} \quad 0 < \omega_i \leq 5 \times 10^5 \tag{2.34}$$

$$\frac{\alpha_i}{\omega_i} = -0.050 \quad \text{for} \quad \omega_i > 5 \times 10^5 \tag{2.35}$$

CORE LOSSES

An approximate formula to account for the effects of eddy current losses in the transformer core can be expressed as follows [56, 89]:

$$R_{core}(\omega) = \text{Re}\{\frac{4N^2A}{ld^2\sigma} x \tanh x\} \tag{2.36}$$

$$x = \frac{d}{2}\sqrt{j\omega\mu\sigma} \tag{2.37}$$

where ω denotes the angular frequency, l is the axial length of the core limb, d represents the lamination thickness, μ and σ indicate the permeability and conductivity of the core material respectively, N signifies the number of coil turns, and A is the total cross-sectional area of the core laminations.

Alternatively, the increase in resistance caused by eddy current losses in the core can be calculated using the method presented in [19]. This approach will be discussed in greater detail in subsequent chapters.

2.4.3. CAPACITANCE CALCULATION

During fast-front transient events, transformers are subjected to rapid voltage pulses containing significant high-frequency contents. These high-frequency transients reveal capacitive effects that normally remain insignificant during regular operating conditions [77]. Therefore, accurately simulating transformer behavior under transient conditions necessitates precise determination of capacitances, which can be incorporated into lumped or traveling-wave models [77].

Depending on the degree of discretization, capacitances used in transformer models can be classified into two types: equivalent capacitances, derived using energy-based approaches, and physical capacitances, calculated directly from the geometry and spatial arrangement of windings. These methods are described in detail in the following sections.

ENERGY METHOD

The energy-based approach is particularly suitable when multiple conductors are grouped and treated as a single section. This method relies on the distribution of the electric field and the stored energy within the transformer to compute the equivalent capacitances. The equivalent capacitance of a winding section is defined as the capacitance value of an equivalent capacitor that exhibits the same electrostatic behavior as the winding section [56].

To illustrate this method, consider Figure 2.11, which depicts various capacitances, including those between turns of the same winding and between turns of adjacent disks. The objective is to replace each section with an equivalent capacitance that preserves the same electrostatic characteristics. This is achieved by leveraging the electrical energy stored within the winding configuration. The energy stored in a capacitor is given by:

$$E = \frac{1}{2}CV^2 \tag{2.38}$$

where C is the capacitance and V is the voltage across it.

Beyond capacitance values, the above equation also requires knowledge of the voltage distribution within the winding, which introduces two challenges. First, the equivalent series capacitance is typically assumed to be a constant value; however, Equation (2.38) indicates that it depends on the time-dependent voltage distribution within the winding. This implies that the actual series capacitance must also be time-dependent [56]. Second, the voltage distribution required for this calculation is generally unknown. In fact, determining this distribution is the primary objective of transient transformer models [56]. While this may initially seem to present a circular dependency, an effective approach to address these challenges is to assume a predefined voltage distribution. One assumption could be considering a linear voltage distribution in the sections [77, 91], as it provides a reasonable approximation of the average voltage distribution within an oscillating winding, and provides a straightforward way to compute the energy stored within the windings [56]. As a result, the series capacitance calculated under this assumption remains constant and can be interpreted as the average series capacitance. Non-linear voltage

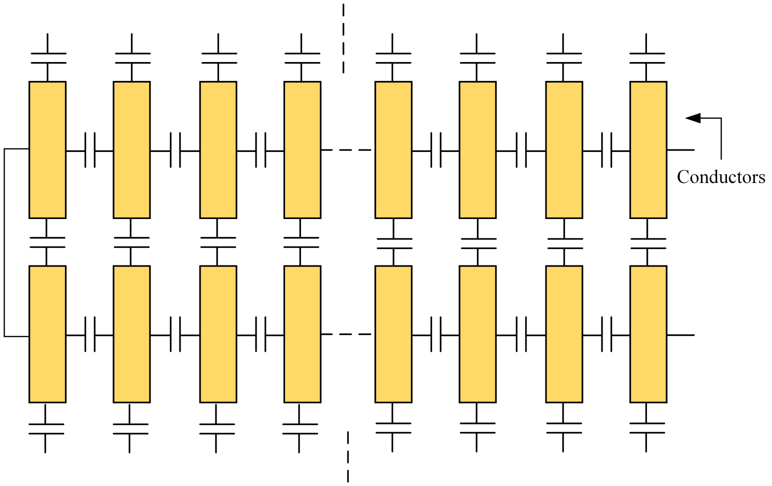

Figure 2.11: An illustration of capacitances between various turns of a winding section.

distribution can also be considered within the windings (discs), as proposed by Stein [92], although this method only determines the initial series capacitance [56].

For the geometry shown in Figure 2.11 and by assuming a linear voltage distribution, equipotential surfaces can be considered between disks, as illustrated in Figure 2.12. The energy stored between these surfaces can then be calculated as follows:

$$E_{\text{tot}} = E_{\text{series}} + E_{\text{shunt}} \tag{2.39}$$

where E_{tot} represents the total stored energy, while E_{series} and E_{shunt} correspond to the energy stored between adjacent turns and between turns and the equipotential surfaces, respectively.

Considering the linear voltage drop along the disk as:

$$V(x) = V\left(1 - \frac{x}{L}\right) \tag{2.40}$$

the energy stored in the shunt capacitance, E_{shunt}, is given by:

$$E_{\text{shunt}} = \frac{1}{2}\left(\frac{2C_{dd}}{L}\right)\int_0^L \left([V(1-\frac{x}{L})-V]^2 + [V(1-\frac{x}{L})-0]^2\right)\mathrm{d}x \tag{2.41}$$

which simplifies to:

$$E_{\text{shunt}} = \frac{1}{2}\left(\frac{4}{3}C_{dd}\right)V^2 \tag{2.42}$$

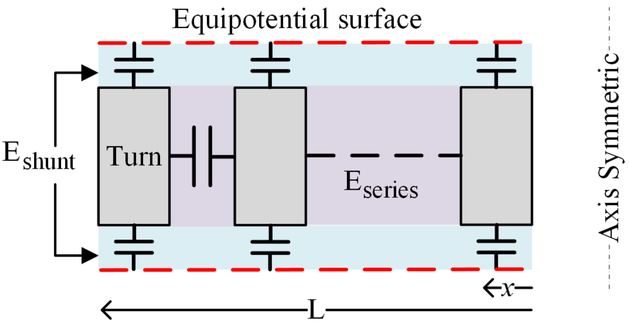

Figure 2.12: An illustration of a winding section and equipotential lines.

where C_{dd} is the total capacitance between turns and the equipotential surfaces.

Similarly, the energy stored in the series capacitance, E_{series}, can be determined using Equation (2.43), as there are $N_t - 1$ turn-to-turn capacitances, each with voltage V/N_t.

$$E_{\text{series}} = \frac{1}{2}(N_t - 1)C_{tt}\left(\frac{V}{N_t}\right)^2 \tag{2.43}$$

in which C_{tt} is the capacitance between adjacent turns.

By combining Equations (2.42) and (2.43) and considering the total voltage drop V, the equivalent capacitance can be expressed as:

$$C_{\text{eq}} = C_{tt}\frac{N_t - 1}{N_t^2} + \frac{4}{3}C_{dd} \tag{2.44}$$

This equivalent capacitance can be used to replace the complex capacitance network in Figure 2.11 while preserving the same electrostatic behavior. By simplifying the network in this manner, the computational complexity is reduced without compromising accuracy in modeling the transformer's transient response.

GEOMETRICAL CAPACITANCES

Geometrical capacitances refer to the physical capacitances that arise due to the spatial arrangement and geometry of transformer windings and their surrounding structures. Unlike equivalent capacitances, which are derived based on the stored energy, geometrical capacitances are determined directly from the physical dimensions, permittivity of the materials, and the relative positioning of conductors.

Depending on the specific geometry of interest, these capacitances can be determined using conventional analytical formulas, such as those applicable to cylindrical or parallel-plate geometries. For more complex arrangements, such as capacitances between transformer windings and the tank, approximate formulas are often employed. For configurations that involve complex geometries or when higher accuracy is required, numerical methods such as FEM can be employed to precisely calculate the capacitances.

2.5. CONCLUSION

This chapter provides an overview of various transformer modeling approaches for different frequency ranges, with a particular focus on white-box modeling techniques. The modeling strategies were categorized based on the frequency content of the transient phenomena under consideration, highlighting the relevance of different levels of detail and parameter accuracy. Analytical, empirical, and numerical methods for determining transformer parameters such as inductance, resistance, and capacitance are discussed in the framework of their applicability, computational requirements, and physical realism.

Despite the extensive research conducted in this area, there remains no consensus in the literature regarding the influence of the magnetic core on transformer's high-frequency behavior. While some studies suggest that the core can be neglected due to minimal flux penetration at high frequencies, others demonstrate that the core continues to exhibit significant effects particularly in terms of damping and complex permeability even at frequencies exceeding 1 MHz. This ongoing debate underscores the need for more comprehensive and physically accurate modeling approaches.

Additionally, eddy current losses in conductors are either neglected or estimated using oversimplified analytical expressions, which may fail to capture the correct loss behavior over a wide frequency range. Moreover, a common limitation in many existing methods is the separate calculation of resistance and inductance parameters, particularly in analytical and empirical approaches. In reality, these quantities are interdependent. Eddy currents circulating within conductive materials alter the magnetic flux distribution, which not only impacts losses but also modifies inductance values as a function of frequency. Consequently, treating these parameters independently can lead to inaccurate predictions of transformer behavior.

In the following chapters, these limitations will be addressed in more detail. We will explore improved techniques for accurately estimating high-frequency transformer parameters, with an emphasis on physically consistent modeling practices that consider the coupled nature of losses and magnetic behavior.

3

MAGNETIC CORE EFFECT ON TRANSFORMER HIGH-FREQUENCY BEHAVIOR

What we observe is not nature itself, but nature exposed to our method of questioning.

Werner Heisenberg

This chapter investigates the influence of magnetic core and conductor eddy current losses on the high-frequency behavior of transformer windings. A simplified disk-type winding structure is modeled using finite element simulations to isolate and quantify the effects of various loss mechanisms. Results demonstrate that while core losses dominate at lower frequencies, their influence becomes negligible at high frequencies due to phase shifts along the winding, which effectively cancel the net magnetomotive force. In contrast, conductor eddy losses remain significant and must be included to accurately capture the damping behavior and inductance values at high frequencies. The findings are supported by both impedance analysis and frequency-domain current phase distributions, offering new insights into the frequency-dependent role of the core and validating key assumptions behind the proposed white-box modeling approach.

Parts of this chapter have been published in:

- F. Nasirpour, M. G. Niasar, and M. Popov. "Magnetic core effects on the high-frequency behavior of transformers". In: *International Journal of Electrical Power & Energy Systems* 159 (2024), p. 110035

3.1. INTRODUCTION

Transformer failures are often triggered by fast transient phenomena, such as lightning impulses, switching surges, and fault-induced transients. These events can cause highly non-linear voltage distributions along transformer windings, potentially exciting resonance and leading to localized overvoltages. Such conditions significantly increase the risk of dielectric breakdown. Therefore, understanding and accurately modeling the high-frequency behavior of transformers is crucial for predicting and mitigating these failure risks. A key aspect of this modeling is the accurate representation of internal damping mechanisms, which limit the amplitude of overvoltages. Losses within the transformer contribute substantially to this damping.

The main sources of loss in transformers include hysteresis and anomalous (excess) losses, ohmic losses caused by currents circulating in conductive materials, and dielectric losses. Detailed modeling of hysteresis and other additional losses by using models such as Preisach or Jiles-Atherton is generally discouraged in the context of high-frequency transformer modeling for network studies, due to the associated complexity [56].

As described in the previous chapter, dielectric losses are incorporated into the model through conductance terms, which can be estimated using the loss tangent, $\tan(\delta)$, of insulation materials. Eddy current losses in the conductors and the core are included via the resistive components, since in configurations where conductors are wound around a magnetic core, the resulting core losses appear as increased resistance in the conductors. This is because the core itself is not explicitly represented in the voltage-current relations [23].

The influence of the magnetic core on the resistance and inductance of winding sections is often neglected, typically justified by the assumption that the magnetic field penetration depth in the core is extremely small at high frequencies (e.g., above 10 kHz), rendering the core's effect negligible. This assumption is further supported by experimental observations showing that the open-circuit and short-circuit impedance characteristics of transformer windings tend to converge at high frequencies, as illustrated in Figure 3.1.

In contrast, several studies have reported that the magnetic core continues to influence transformer impedance and damping characteristics even at frequencies exceeding 1 MHz. For example, it has been shown in [82] that the core plays a significant role in damping transient overvoltages, and that inductance values remain appreciable at frequencies above 1MHz, challenging the assumption that magnetic flux cannot penetrate the core at such frequencies. Another study [83] has concluded that, when the LV winding is open-circuited, the laminated core becomes the dominant source of losses. The authors in [94] have demonstrated that the effective complex permeability of

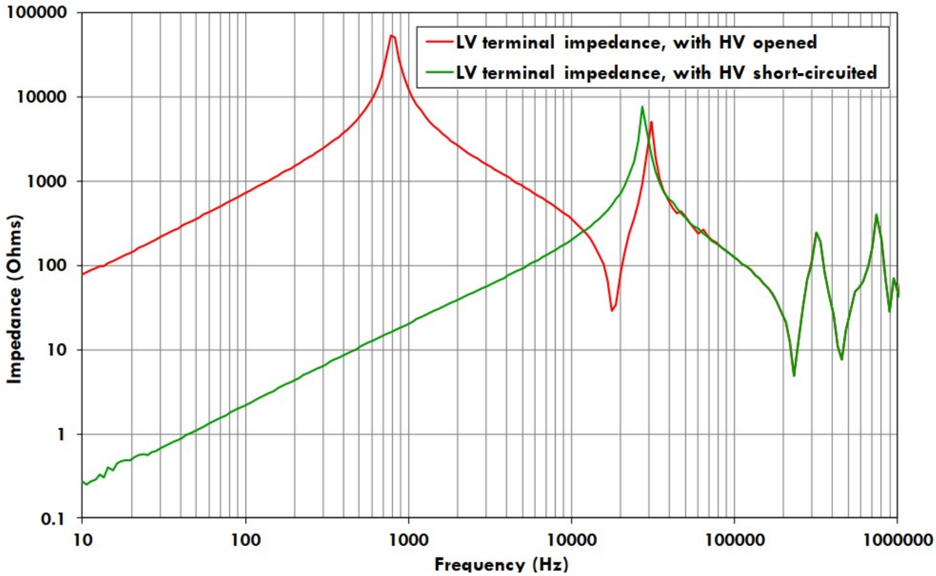

Figure 3.1: Terminal impedance measurements [43].

the transformer core materials remains appreciable up to at least 1 MHz. These studies argue that conductor losses are often negligible in comparison to core losses and suggest that the magnetic core should still be accounted for at frequencies above 10kHz.

This divergence in findings underscores the need for a more comprehensive and systematic investigation into the role of the magnetic core in the high-frequency behavior of transformers.

This chapter aims to clarify the influence of the magnetic core on the high-frequency response of transformers. A combined methodology involving finite element simulations and experimental validation is adopted. Initially, numerical methods are employed to assess the significance of eddy current losses in both the core and the conductors across a wide frequency range. Subsequently, high-frequency models for a representative winding geometry are developed to investigate the separate and combined effects of these losses. Finally, experimental measurements are conducted to validate the numerical results and support the general conclusions.

3.2. AN EQUIVALENT CORE MODEL FOR HIGH-FREQUENCY ANALYSES

To systematically investigate the influence of the magnetic core on the high-frequency behavior of transformers, it is essential to develop detailed models that allow separate assessment of eddy current effects in the conductors and core.

At this stage, the most appropriate and accurate approach is the use of numerical methods, as they solve the governing equations without simplifications typically associated with analytical methods. To study eddy current losses, a simplified winding configuration wound on a laminated core is considered. This setup provides a representative case analogous to real transformers, without the need to model the complex transformer geometry.

When dealing with laminated cores, several modeling approaches are available. One option is to model the laminated structure explicitly using real permeability and conductivity values for each lamination sheet and the insulation in between. However, this method is computationally expensive as it requires very fine meshes, especially at higher frequencies.

An alternative and more efficient approach involves replacing the laminated core with a core modeled with zero conductivity and complex permeability. In this case, the ohmic losses due to eddy currents circulating in the core are approximated by hysteresis losses introduced via the complex permeability. Since the core is electrically insulated, detailed meshing near the edges of the laminations is no longer necessary, as no current flows through these areas. The losses are captured through the magnetic field distribution, which remains accurate even with relatively coarse meshes.

Despite its practicality in numerical modeling, this approach is not adopted in this thesis, as the ultimate goal is to develop an analytical framework to obtain high-frequency transformer models. The use of complex permeability is not compatible with the types of analytical formulations presented in chapter 4. Instead, the laminated core is approximated by an equivalent solid core model with an effective conductivity,σ^*, chosen to reproduce the same loss characteristics. This approach eliminates the need to explicitly model each lamination and the insulation between them, significantly simplifying the meshing requirements, reducing memory demand, and improving computational efficiency.

The effective conductivity of the equivalent solid core is calculated using the following:

$$\sigma^* = \frac{\sigma k}{n^2} \tag{3.1}$$

where σ is the base material conductivity, k is the stacking factor accounting for insulation gaps between lamination sheets, and n is the number of sheets. The effective permeability μ_z^* can be determined using Equation (3.2), where μ_z represents the permeability of the laminated core in the flux direction.

$$\mu_z^* = k\mu_z + (1-k) \simeq k\mu_z \tag{3.2}$$

To verify the accuracy of this substitution, two geometries are simulated in FEM environment: one featuring an explicitly modeled laminated core, and the other using the equivalent solid core with effective conductivity. Table 3.1 outlines the geometric details and simulation configuration for this case. Both models share identical geometries, except for the core representation. This is shown in Figure 3.2. When replacing the laminated core with an equivalent solid core, only the conductivity in the plane orthogonal to the flux direction is modified. Given the toroidal shape of the core, a new coordinate system is defined in COMSOL Multiphysics, which is consistently aligned with the core's cross-section. This allows the software to distinguish the direction of conductivity by specifying the conductivity values as a vector, as illustrated in Figure 3.3.

Table 3.1: The required details of the geometries shown in Figure 3.2.

Parameter	**Value**
Number of turns	32
Laminated sheet width (mm)	0.3
Insulation width between sheets (mm)	0.01
Core conductivity (S/m)	1.12×10^7
Inner/Outer diameter (mm)	6.9 / 13.08
Core height (mm)	1
Core relative permeability	4000
Current source (A)	1

To maintain computational efficiency, only 1/32 of the entire core structure is simulated by exploiting the core's geometric symmetry. Periodic boundary conditions are applied to ensure that the reduced model accurately represents the behavior of the complete core structure. A copper conductor is wound around the core, and by exciting it with a current source, the average magnetic flux density within the core cross-section is obtained for various frequencies, examples of which are shown Figure 3.4. Since the magnetic flux distributions in both the laminated and equivalent solid core cases are identical, the parameters dependent on the flux—specifically, the winding's inductance and resistance—are also expected to be the same. It should be noted that

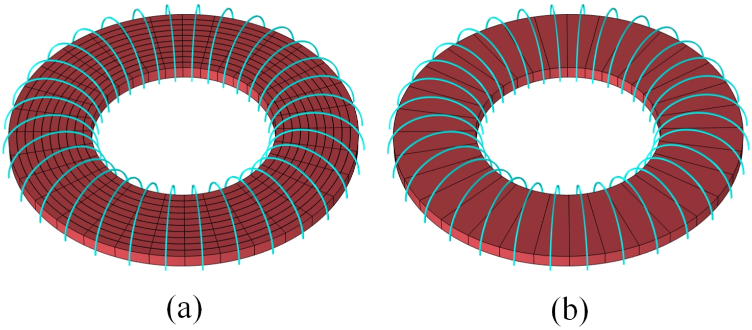

Figure 3.2: The geometry of (a) a laminated core and (b) its equivalent solid one.

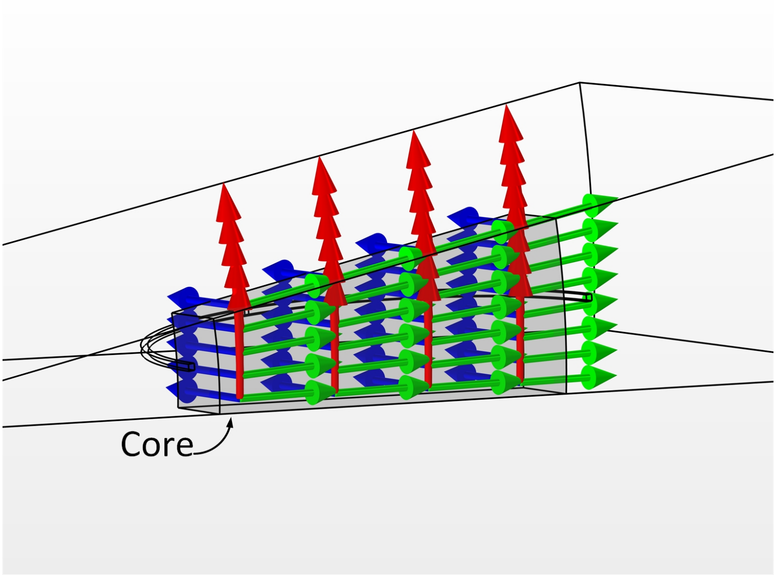

Figure 3.3: The coordinate system used for the equivalent solid core.

in Figure 3.4, only the magnetic flux within the core is compared, and the leakage flux outside the core is not included. This does not affect the validity of the analysis, as for the frequency range in which the core has a significant impact, nearly all magnetic flux remains confined within the core. This point is further explained later in this chapter and in Chapter 4.

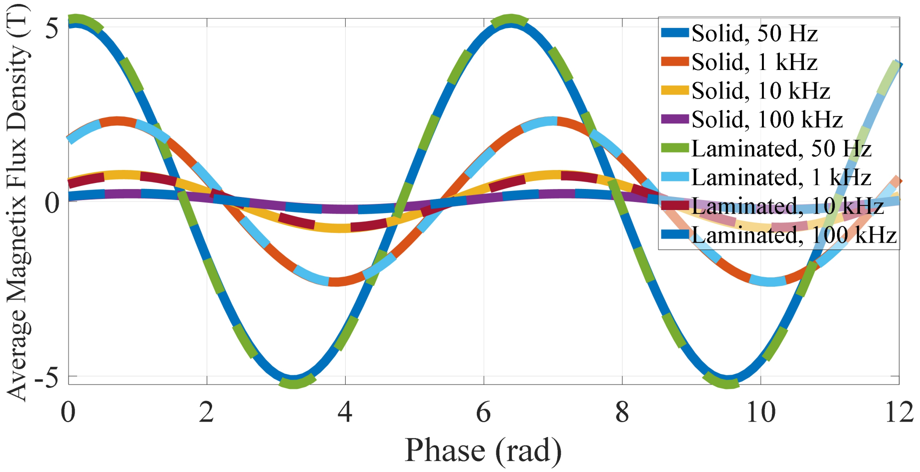

Figure 3.4: Average magnetic flux density in laminated and equivalent solid cores

This expectation is confirmed by the results presented in Tables 3.2 and 3.3, which compare the inductance and resistance values between the laminated core and the equivalent solid core geometries. The close agreement between the two models demonstrates that Equations (3.1) and (3.2) can be reliably used to replace a laminated transformer core with an equivalent solid core, without introducing significant computational errors.

Having validated this modeling approach, the next step is to investigate the impact of core eddy current losses on the winding's high-frequency response.

Table 3.2: Inductance of the Windings in Figure 3.2.

Frequency Hz	Inductance (lamination) mH	Inductance (solid) mH	Difference %
50	15.66	15.71	-0.31
100	15.01	15.11	-0.66
200	13.03	13.19	-1.22
1 k	5.20	5.34	-2.69
100 k	0.465	0.446	4.08
1 M	0.155	0.147	5.16

Table 3.3: Resistance of the Windings in Figure 3.2.

Frequency Hz	Resistance (lamination) mΩ	Resistance (solid) mΩ	Difference %
50	0.71	0.69	-2.24
100	2.17	2.07	-4.60
200	6.69	6.52	-2.54
1 k	29.01	29.92	-3.13
100 k	341.93	338.86	-0.89
1 M	1089.70	1070.7	-1.10

3.3. IDENTIFICATION

To investigate the influence of the core on high-frequency behavior, a winding configuration based on a typical disk-type arrangement comprising twenty disks with ten turns each is modeled in COMSOL Multiphysics using a 2D representation to reduce computational requirements. The details of this case are given in Table 3.4. The laminated core is first replaced with an equivalent solid core described in the previous section. Then, to model the winding in 2D environment, the core is substituted by a cylindrical shape with a length equal to the mean magnetic path length of the original rectangular core. This equivalence is illustrated in Figure 3.5. In the 2D model, it is necessary to ensure that the magnetic path is properly closed. To achieve this, a periodic boundary condition is applied at the end of the core. The complete geometry with the boundary of the problem is shown in Figure 3.6.

Table 3.4: Details of Disk-type Winding and Core

Component	**Parameter**	**Value**
HV winding	Winding type	Disk
	Number of disks	20
	Number of turns per disk	10
	Conductor size (radial × axial) (mm)	6.99 × 15.35
	Inner/Outer diameter (mm)	200 / 376
Core	Leg diameter (mm)	100
	Leg height (m)	1.2

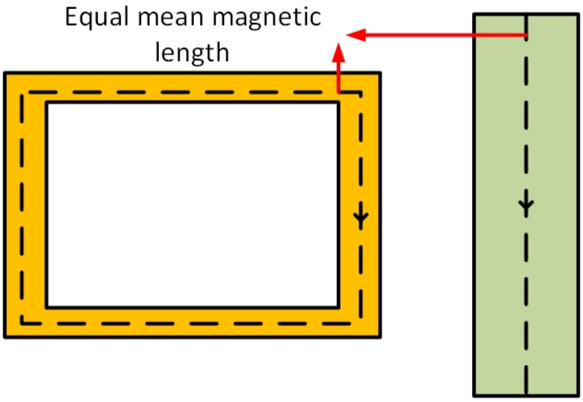

Figure 3.5: A rectangular core and its equivalent 2D representation.

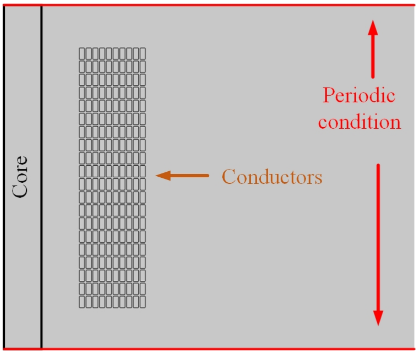

Figure 3.6: Winding geometry used for simulation studies

As detailed model development is not the primary focus of this chapter, only the conceptual framework is presented here. Each section can be modeled as illustrated in Figure 3.7. Each disk is represented by an equivalent circuit consisting of inductance, resistance, and capacitance. The inductance and resistance are extracted from magnetostatic simulations by neglecting capacitive effects. In a separate step, the capacitances are calculated using electrostatic simulations, ignoring magnetic effects. This sequential approach allows for independent determination of each parameter.

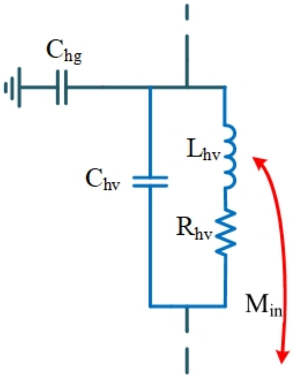

Figure 3.7: Equivalent circuit of each winding section.

Considering the voltage-current relationship:

$$V = ZI \tag{3.3}$$

The parameters of each section can be obtained by exciting the section of interest with a current source while leaving the others open-circuited. The impedance is then calculated as:

$$Z_{ij} = \frac{V_{ij}}{I_{jj}} \tag{3.4}$$

The real part of Z_{ij} gives the resistance, and the imaginary part corresponds to the reactance, from which the inductance is derived by dividing by angular frequency. In Equation (3.4), indices i and j denote the respective winding sections being analyzed.
Capacitances are computed using the Maxwell capacitance matrix method, based on charge-voltage relationships. This involves exciting one section while short-circuiting the rest.

To analyze the contribution of different loss mechanisms, the inductance and resistance values are extracted under the following three simulation cases:

1. Both core and conductor eddy currents included;
2. Only core eddy currents included;
3. Core excluded, with only conductor losses modeled.

For the case where the conductors' skin effect is neglected, the homogenized multi-turn approach is used. The core conductivity and permeability are set to zero and one, respectively, when the eddy losses in the core are ignored. In the other case, material conductivity is defined to account for conductive losses. Losses in dielectric materials are neglected, as the focus of this study is on conductive loss contributions.
With this model established, the influence of core losses on the high-frequency behavior of the transformer can be systematically investigated.

3.4. IMPACT OF EDDY CURRENTS IN THE CORE ON WINDING PARAMETERS

In the first step, the inductance and resistance values for sections are compared across the three modeling cases. Figures 3.8 and 3.9 presents the self-inductance and resistance of the first section as an example. It is worth noting that the capacitance values are not included in this comparison, as all models utilize the same capacitance values.

According to Figures 3.8 and 3.9, when core eddy current losses are included, the resulting inductance and resistance values are significantly dominated by them. The values obtained when core eddy currents are considered are several orders of magnitude higher than those calculated when core losses are neglected, and the influence of conductor eddy losses appears to be negligible in comparison.

These findings suggest that the commonly held assumption that magnetic flux does not penetrate the core at high frequencies because of substantial eddy losses is not entirely accurate. This misconception largely arises from the traditional calculation of penetration depth using the bulk electrical conductivity of the core material (e.g., iron). In reality, the laminated structure of the core drastically reduces its effective conductivity, resulting in a much larger penetration depth. The depth calculated using the actual material conductivity reflects the penetration for individual sheets rather than the entire core cross-section (this distinction becomes clearer when considering the penetration depth at 50 Hz). While this explanation supports the possibility of the magnetic flux existence in the core at high frequencies, it does not fully explain the observed transformer behavior at high frequencies. For example, Figure 3.1 shows the impedance characteristics of the low-voltage (LV) winding in two scenarios. When the high-voltage (HV) winding is short-circuited, the core is effectively bypassed. However, when the HV winding is open-circuited, the magnetic flux is expected to circulate within the core, thereby significantly influencing the inductance and resistance values. Despite this, the measured characteristics do not show the expected dominance of core-related effects, indicating that additional mechanism(s) must be considered to fully explain the transformer's behavior at high frequencies. This is the subject of the next section.

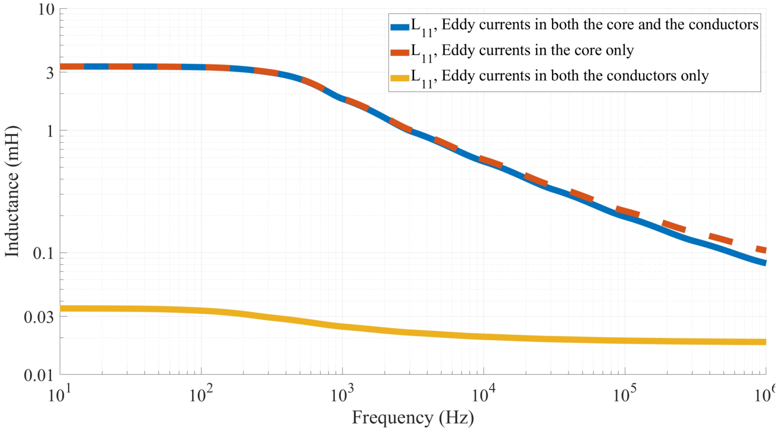

Figure 3.8: Self-inductance of a winding section.

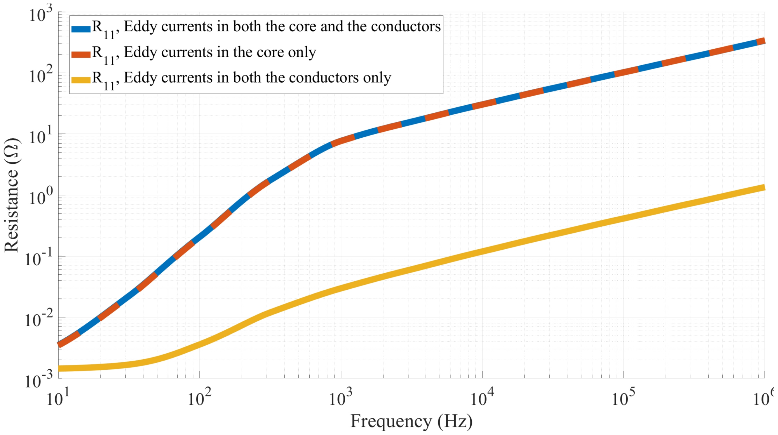

Figure 3.9: Self-resistance of a winding section.

3.5. HIGH-FREQUENCY IMPEDANCE BEHAVIOR AND CORE DECOUPLING MECHANISM

To further investigate the influence of eddy current losses in both the conductors and the core, the impedance characteristics of the modeled winding structure are plotted for the three simulation cases. As shown in Figure 3.10, despite the significant differences in computed inductance and resistance values when core eddy losses are included, the impedance characteristics at high frequencies closely overlap with the case where only conductor eddy currents are considered. In contrast, the case in which conductor eddy losses are neglected, shows a remarkable different behavior. This observation highlights the critical role of conductor eddy losses in accurately modeling high-frequency behavior.

The reason why core eddy losses do not significantly influence the impedance at high frequencies can be explained as follows: at these frequencies, the wavelength of the traveling wave approaches the physical length of the winding. Consequently, substantial phase shifts occur between different sections of the winding, leading to a distributed magnetic flux that is out of phase along the winding length. This phase difference effectively cancels the net magnetomotive force (MMF), resulting in negligible flux in the core. Therefore, the core becomes magnetically inactive not because of the limited penetration depth, which remains significant, as shown in section 3.4, but because of the magnetic flux phase shifts within the winding.

In the parameter extraction process, each section is treated independently, hence the effects of the phase shift along the winding would not be apparent. However, as the frequency increases, the effect of the

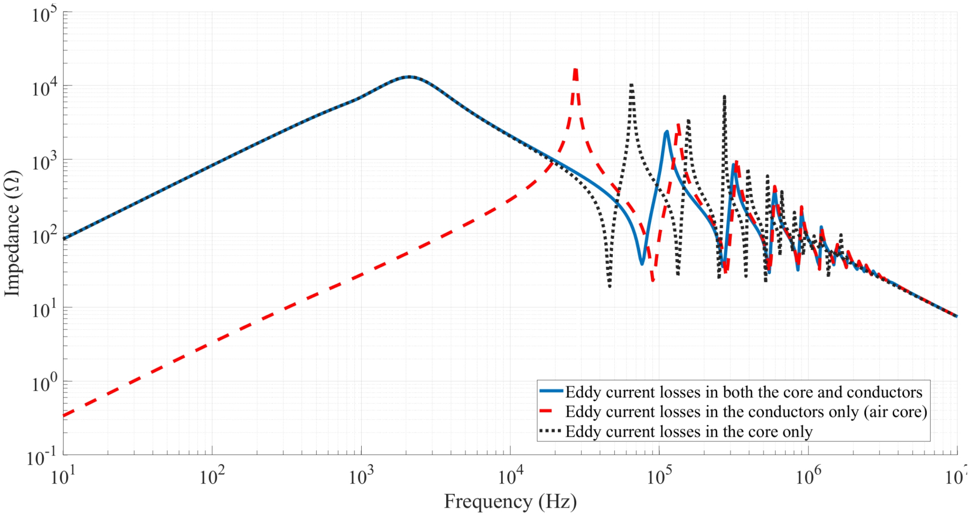

Figure 3.10: The impedance characteristics of the representative winding for the three case scenarios.

common flux diminishes due to phase cancellation, while local conductor eddy losses become dominant. This explains why, when conductor eddy losses are ignored, the impedance characteristics diverge significantly at high frequencies. Figure 3.11 illustrates the phase distribution of the current in different sections of the winding across a wide frequency range. In this case, the winding is excited with a one-ampere current source in the frequency domain, which corresponds to a Dirac delta function in the time domain. As shown, at lower frequencies, the current maintains an almost uniform phase across all winding sections. However, as the frequency increases, distinct phase differences emerge between various parts of the winding. At sufficiently high frequencies, some sections exhibit current flowing in the opposite phase relative to others, resulting in a significant reduction of the net magnetomotive force (MMF) and, consequently, very little magnetic flux in the core. To further illustrate this phenomenon, the current phasors representing the MMF contribution of each section at selected frequencies are shown in Figure 3.12.

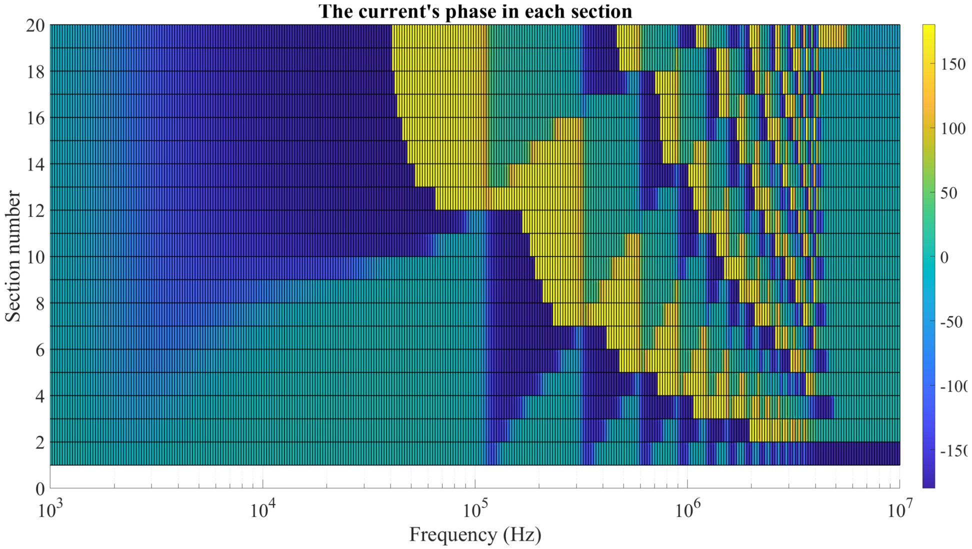

Figure 3.11: The electrical current’s phase in each section.

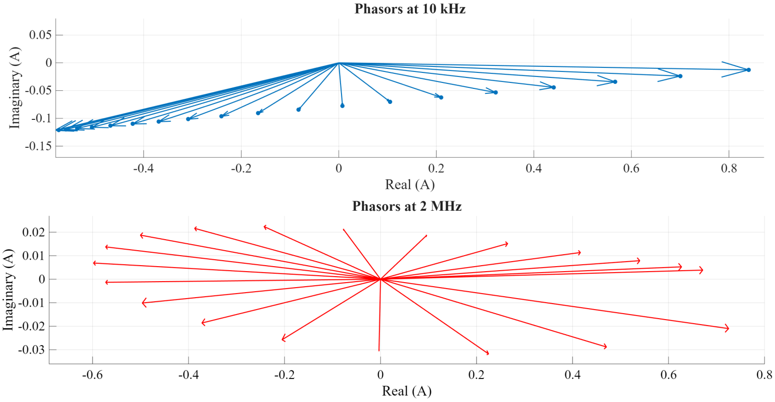

Figure 3.12: The current’s phasor in the sections at two frequencies.

Additionally, Figure 3.13 schematically shows a simplified double-disk geometry to emphasize this concept. In this figure, the 2D cross-sectional representation implies that current flows perpendicular to the plane of the figure. When the phase shift is negligible, the magnetic flux in the core is substantial and contributes to both losses and inductance. However, when significant phase shifts are present, the core becomes magnetically inactive and does not alter the magnetic field distribution outside of it, or its influence becomes negligible. Thus, in this frequency range, the inductance and resistance values can be accurately determined without including the core in the model. This observation forms an essential basis for the modeling methodology adopted in this thesis, which will be elaborated upon in the following chapters.

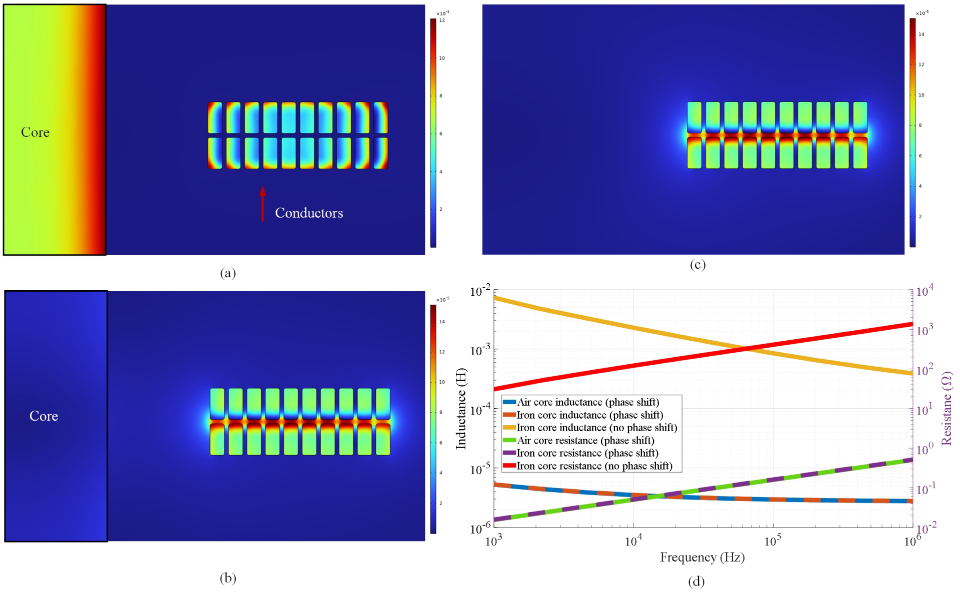

Figure 3.13: (a) Disks carrying the same current in the presence of the magnetic core, (b) Disks carrying an opposite current in the presence of the magnetic core, (c) Disks carrying an opposite current in the air, (d) The inductance and resistance of the winding in different cases.

To further validate this behavior, the frequency response of an inductor with two different core configurations, ferrite and air, is measured and compared, as shown in Figure 3.14. Given that ferrite cores possess low conductivity and are capable of operating effectively at high frequencies, any significant flux in the core at high frequencies would result in a noticeably different response compared to the air-core case. However, because of the phase shift mechanism described earlier, the responses are nearly identical. This confirms that the presence of the core does not significantly influence the magnetic field in the vicinity of the conductors; thus, the inductance and resistance values can be determined without accounting for the core in this frequency range.

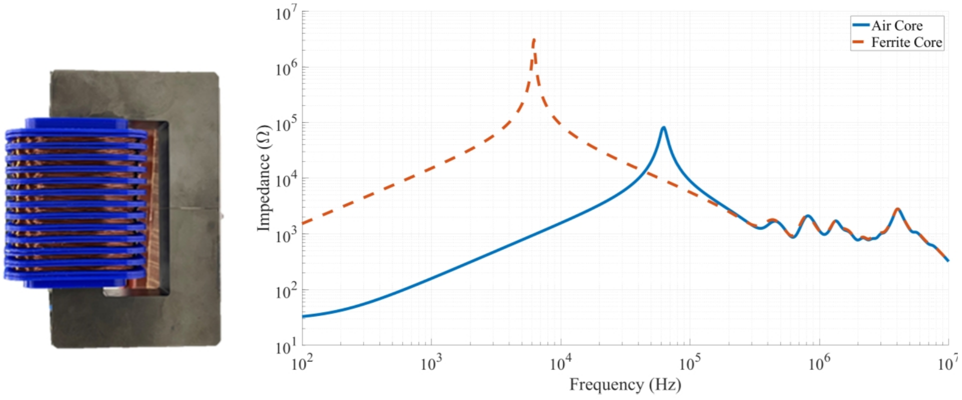

(a)

(b)

Figure 3.14: (a) The inductor used for the measurement verification, (b) Its frequency response with air and ferrite cores.

It should be noted that although the core's influence becomes negligible at high frequencies, it remains essential at low frequencies (around 10 kHz for large power transformers), particularly for capturing the correct initial conditions in simulations. Omitting the core in such cases would result in unrealistically low transformer impedance; therefore, the core must still be included in the overall modeling framework.

3.6. CONCLUSIONS

In this chapter, the influence of the core and conductor eddy current losses on the high-frequency behavior of transformer windings has been systematically investigated using numerical modeling. By applying a simplified disk-type winding structure and evaluating different modeling scenarios, it was shown that conductor eddy current losses play a dominant role in shaping the impedance characteristics at high frequencies. In contrast, despite the significant eddy current losses in the core at lower frequencies, their impact becomes negligible at higher frequencies.

This behavior was attributed not to limited flux penetration depth in the laminated core, as is commonly assumed, but also to the distributed phase shift along the winding at high frequencies. This phase shift leads to a reduction of the net magnetomotive force, effectively rendering the core magnetically inactive in this frequency range. The study demonstrated that, even when the core is present, it does not significantly alter the magnetic field distribution in the vicinity of the conductors nor affect the calculated impedance at high frequencies. Furthermore, the results highlight the necessity to include conductor eddy current losses in the model to ensure accurate high-frequency response. These losses not only contribute to the damping behavior but also influence the inductance values, thereby affecting the overall transient response of the transformer. Nevertheless, the core remains essential for accurately modeling low-frequency behavior and ensuring realistic initial conditions in time-domain simulations. The findings of this chapter not only clarify the role of the core and conductor losses across the frequency spectrum but also provide a solid foundation for the modeling methodology adopted in this thesis, which will be elaborated upon in subsequent chapters.

4

TRANSFORMER HIGH-FREQUENCY WINDING IMPEDANCE

> *Everything should be made as simple as possible, but not simpler.*
>
> Albert Einstein

This chapter presents a detailed analytical framework for modeling the frequency-dependent impedance of transformer windings. The impedance calculation is decomposed into contributions from the magnetic flux confined within the core and that outside it. The influence of the core is analyzed based on a simplified cylindrical geometry, while the leakage flux is treated by assuming the air-core approximation. The resulting resistance and inductance matrices are used to construct the transformer's full admittance matrix, which captures both low- and high-frequency behaviors. The analytical formulation is validated against FEM results, demonstrating both accuracy and computational efficiency.

Parts of this chapter have been published in:

- F. Nasirpour, T. Luo, M. G. Niasar, and M. Popov. "Multi-Winding Power Transformer Modeling for Fast-Front Transients". In: *IEEE Transactions on Power Delivery* (2025), pp. 1–13

4.1. INTRODUCTION

In the previous chapter, it was shown that for the low-frequency region, the inductance and resistance of the winding are primarily influenced by the core and associated eddy current losses, while skin and proximity effects in the conductors are negligible. For higher frequencies, the net magnetomotive force (MMF) generated by the winding becomes insignificant, and the core no longer alters the magnetic field distribution in its surroundings, particularly near the conductors. These observations can be used to calculate the frequency-dependent inductance and resistance of transformer windings.

For the rest of the chapter, the term impedance of the winding refers to the frequency-dependent inductance and resistance of a section, excluding its capacitance. The calculation of capacitances is explained in Chapter 2.

4.2. CALCULATION OF THE WINDING SECTION IMPEDANCE

The mutual impedance between the winding sections n and m can be defined as:

$$Z_{nm} = Z_{\text{core}(nm)} + Z_{\text{air}(nm)} \tag{4.1}$$

where $Z_{\text{core}(nm)}$ is the impedance contribution from the core-related magnetic flux, and $Z_{\text{air}(nm)}$ corresponds to the component arising from the flux outside the core. To model the high-frequency behaviour of the transformers, the term $Z_{\text{air}(nm)}$ can be effectively approximated by assuming an air-core configuration. As demonstrated in the previous chapter, because of the phase shift introduced at high frequencies, the resulting impedance remains practically unchanged whether the flux is assumed to be entirely external to the core or the core is replaced with air. Therefore, the air-core assumption is justified in this context. The resistance R_{nm} and inductance L_{nm} can be obtained as:

$$R_{nm} = \Re(Z_{nm}) \tag{4.2}$$

$$L_{nm} = \Im(\frac{Z_{nm}}{2\pi f}) \tag{4.3}$$

where $\Re$ and $\Im$ denote the real and imaginary parts, respectively, and f is the frequency.

4.2.1. CORE-COMPONENT IMPEDANCE

Consider the configuration depicted in Figure 4.1 [95]. The ferromagnetic core is assumed to be infinitely long, characterized by conductivity σ_2, permeability μ_2, and radius b. A filamentary turn of radius a is wound around the core at the axial position $z = 0$, carrying a sinusoidal current whose phasor representation is I.

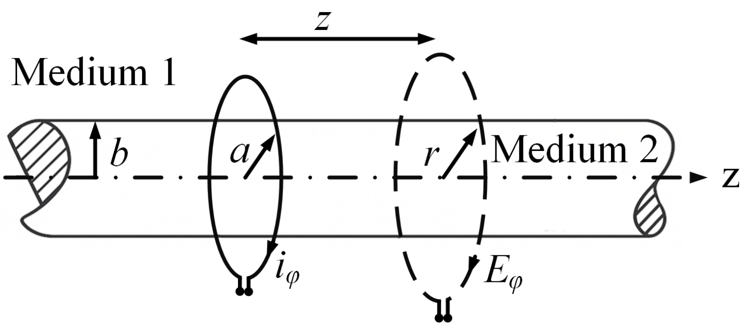

Figure 4.1: Configuration of filamentary turns around an infinitely long ferromagnetic core

The mutual impedance between the energizing turn and the second open-circuit turn with radius r, located at an axial distance z, is determined through the azimuthal electric field intensity $\boldsymbol{E}_\varphi$. Under quasi-stationary conditions, the problem can be analyzed using Maxwell's equations [95]:

$$\nabla \times \mathbf{E} = -\frac{\partial \mathbf{B}}{\partial t} \tag{4.4}$$

$$\nabla \times \mathbf{B} = \mu \mathbf{J} + \epsilon_0 \frac{\partial \mathbf{E}}{\partial t} \tag{4.5}$$

Considering the symmetry of the problem, the following field assumptions apply [95]:

$$E_r = 0, \quad E_z = 0, \quad \frac{\partial E_\varphi}{\partial \varphi} = 0 \tag{4.6}$$

$$H_\varphi = 0 \quad \frac{\partial H_r}{\partial \varphi} = 0, \quad \frac{\partial H_z}{\partial \varphi} = 0 \tag{4.7}$$

With these assumptions, the relevant field equations in cylindrical coordinates simplify to:

$$\frac{\partial E_\varphi}{\partial z} = j\omega\mu_r H_r, \tag{4.8}$$

$$\frac{1}{r}\frac{\partial (rE_\varphi)}{\partial r} = -j\omega\mu_z H_z, \tag{4.9}$$

$$\frac{\partial H_r}{\partial z} - \frac{\partial H_z}{\partial r} = \sigma E_\varphi + I_\varphi \delta(r-a)\delta(z), \tag{4.10}$$

The Dirac delta function $\delta(r-a)$ and $\delta(z)$ indicates the location of the energizing turn [95]. By substituting equations Equation (4.8) and Equation (4.9) into Equation (4.10), the governing equations for the two media are obtained as follows [95]:

1. Medium 1 ($r \geq b$)

$$\frac{\partial^2 E_{\varphi_1}}{\partial z^2} + \frac{\partial^2 E_{\varphi_1}}{\partial r^2} + \frac{1}{r}\frac{\partial E_{\varphi_1}}{\partial r} - \frac{E_{\varphi_1}}{r^2} = j\omega\mu_1 I_\varphi \delta(r-a)\delta(z) \tag{4.11}$$

2. Medium 2 ($r \leq b$)

$$\frac{\mu_{2z}}{\mu_{2r}}\frac{\partial^2 E_{\varphi_2}}{\partial z^2} + \frac{\partial^2 E_{\varphi_2}}{\partial r^2} + \frac{1}{r}\frac{\partial E_{\varphi_2}}{\partial r} - \frac{E_{\varphi_2}}{r^2} = j\omega\mu_{2z}\sigma_2 E_{\varphi_2} \tag{4.12}$$

Medium 1 is assumed to be non-conductive ($\sigma = 0$), and $\mu_{1r} = \mu_{1z} = \mu_1$. The following field continuity conditions must be satisfied at $r = b$:

$$E_{\varphi_1} = E_{\varphi_2} \tag{4.13}$$

$$H_{z_1} = H_{z_2} \tag{4.14}$$

Additionally, the boundary conditions are [95]:

$$E_{\varphi_2} = 0 \quad \text{at } r = 0, \tag{4.15}$$

$$E_{\varphi_1} \to 0 \quad \text{as } r \to \infty, \tag{4.16}$$

$$E_{\varphi_1}, E_{\varphi_2} \to 0 \quad \text{as } z \to \pm\infty. \tag{4.17}$$

To solve the system of equations, the Fourier integral transform is applied with respect to z. Transformed quantities are denoted by an asterisk ($*$) [95]:

$$\frac{\partial^2 E^*_{\varphi_1}}{\partial r^2} + \frac{1}{r}\frac{\partial E^*_{\varphi_1}}{\partial r} - \frac{E^*_{\varphi_1}}{r^2} - \beta^2 E^*_{\varphi_1} = j\omega\mu_1 I_\varphi \delta(r-a) \tag{4.18}$$

$$\frac{\partial^2 E^*_{\varphi_2}}{\partial r^2} + \frac{1}{r}\frac{\partial E^*_{\varphi_2}}{\partial r} - \left(\frac{1}{r^2} + c\beta^2 + m^2\right) E^*_{\varphi_2} = 0 \tag{4.19}$$

where $c = \mu_{2z}/\mu_{2r}$ and

$$m = \sqrt{j\omega\mu_{2z}\sigma_2} \tag{4.20}$$

Equation Equation (4.19) is a modified Bessel differential equation, with a general solution:

$$E^*_{\varphi_2} = A I_1(\Gamma r) + B K_1(\Gamma r) \tag{4.21}$$

where I_1 and K_1 are the modified Bessel functions of the first and second kind, respectively, and:

$$\Gamma^2 = c\beta^2 + m^2 = \frac{\mu_{2z}}{\mu_{2r}}\beta^2 + j\omega\mu_{2z}\sigma_2 \tag{4.22}$$

To ensure regularity at $r = 0$, we set $B = 0$.
Assuming the field at $r = b$ is $E^*_{\varphi b}$, the solution becomes:

$$E^*_{\varphi_2}(r) = \frac{I_1(\Gamma r)}{I_1(\Gamma b)} E^*_{\varphi b} \tag{4.23}$$

The solution in medium 1 is given by [95]:

$$\begin{aligned} E^*_{\varphi_1} = \frac{K_1(\beta r)}{K_1(\beta b)} E^*_{\varphi b} + j\omega\mu_1 a \bigg\{ \frac{K_1(\beta r) I_1(\beta b) K_1(\beta a)}{K_1(\beta b)} \\ - I_1(\beta r) K_1(\beta a) \bigg\} I_\varphi \end{aligned} \tag{4.24}$$

For $r > a$, the terms r and a should be interchanged in $I_1(\beta r)K_1(\beta a)$.
At $r = b$, the field intensities must be continuous, i.e., $H_{z_1} = H_{z_2}$. Hence:

$$\frac{1}{j\omega\mu_1}\frac{1}{r}\frac{\partial(rE^*_{\varphi_1})}{\partial r} = \frac{1}{j\omega\mu_{2z}}\frac{1}{r}\frac{\partial(rE^*_{\varphi_2})}{\partial r} \quad \text{at } r = b \tag{4.25}$$

Differentiating both sides, and using the following Bessel function identities:

$$\frac{\partial I_n(r)}{\partial r} = I_{n-1}(r) - \frac{n}{r} I_n(r) \tag{4.26}$$

$$\frac{\partial K_n(r)}{\partial r} = -K_{n-1}(r) - \frac{n}{r} K_n(r) \tag{4.27}$$

yields:

$$\frac{\partial(rK_1(\gamma r))}{\partial r} = -\gamma r K_0(\gamma r) \tag{4.28}$$

$$\frac{\partial(rI_1(\gamma r))}{\partial r} = \gamma r I_0(\gamma r) \tag{4.29}$$

Thus, the expression for $E^*_{\varphi b}$ is [95]:

$$E^*_{\varphi b} = -j\omega\mu_1 \frac{a\beta K_1(\beta a) I_1(\Gamma b)\left[I_0(\beta b)K_1(\beta b) + I_1(\beta b)K_0(\beta b)\right]}{\frac{\mu_1}{\mu_{2z}}\Gamma I_0(\Gamma b)K_1(\beta b) + \beta K_0(\beta b) I_1(\Gamma b)} I_\varphi \tag{4.30}$$

The electric fields E_{φ_1} and E_{φ_2} are obtained by applying the inverse Fourier transform. In medium 1:

$$E_{\varphi_1}(r,z) = \frac{1}{2\pi}\int_{-\infty}^{\infty} E^*_{\varphi_1}(r,\beta)e^{j\beta z}\,d\beta \tag{4.31}$$

The mutual impedance Z between the turns is found by evaluating the induced voltage in the secondary turn [95]:

$$V = ZI_\varphi \tag{4.32}$$

$$V = -\int_0^{2\pi} E_{\varphi_1}(r,z)r\,d\varphi = -2\pi r E_{\varphi_1}(r,z) \tag{4.33}$$

Thus:

$$Z = \frac{-2\pi r E_{\varphi_1}(r,z)}{I_\varphi} \tag{4.34}$$

The impedance Z can be expressed as:

$$Z = j\omega L_1 + Z_c \tag{4.35}$$

where:

$$L_1 = \mu_1 ra\int_{-\infty}^{\infty} I_1(\beta r)K_1(\beta a)e^{j\beta z}\,d\beta \tag{4.36}$$

(For $r > a$, interchange r and a in the integral.)
and

$$Z_c = j\omega\mu_1 ra\int_{-\infty}^{\infty} K_1(\beta a)\frac{K_1(\beta r)I_0(\beta b)}{K_0(\beta b)} \times \left\{\frac{1-\frac{\mu_1}{\mu_{2z}}\frac{\Gamma}{\beta}\frac{I_1(\beta b)I_0(\Gamma b)}{I_0(\beta b)I_1(\Gamma b)}}{1+\frac{\mu_1}{\mu_{2z}}\frac{\Gamma}{\beta}\frac{I_0(\Gamma b)K_1(\beta b)}{K_0(\beta b)I_1(\Gamma b)}}\right\} e^{j\beta z}\,d\beta \tag{4.37}$$

The first term is equivalent to the mutual inductance between two filamentary turns in air, aligned along the same axis, as given by Maxwell [95]:

$$L_1 = \mu_1\sqrt{ra}\frac{2}{k}\left[\left(1-\frac{k^2}{2}\right)K(k) - E(k)\right] \tag{4.38}$$

where

$$k = \sqrt{\frac{4ar}{z^2 + (a+r)^2}} \tag{4.39}$$

and K and E denote the complete elliptic integrals of the first and second kinds, respectively. The second term accounts for the effects of the magnetic core.

For practical transformers with a finite-length core, the core can be idealized as a straight segment placed between two infinitely permeable magnetic plates, as shown in Figure 4.2 [95]. This effectively closes the magnetic circuit.

Since the plates are assumed to be infinitely permeable, the boundary condition becomes [95]:

$$H_r = 0 \quad \text{at } z = \pm\frac{l}{2} \tag{4.40}$$

At these boundaries, the magnetic field lines must enter and exit perpendicularly. A similar field configuration can also be achieved by removing the infinite plates and introducing an infinite number of image sources along the axial direction, as depicted in Figure 4.3 [95].

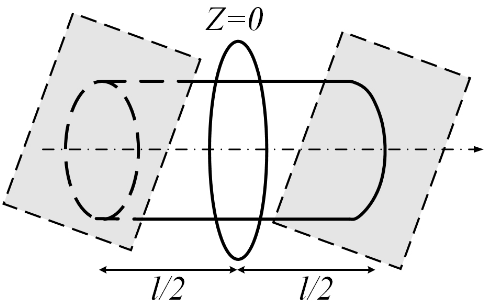

Figure 4.2: Closed magnetic core configuration.

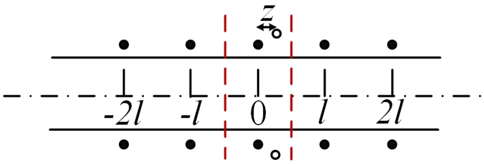

Figure 4.3: Replacement of the plates with an infinite number of images.

Rewriting Equation (4.35) as:

$$Z = \int_{-\infty}^{\infty} G(a,r,\beta) e^{j\beta z} d\beta \tag{4.41}$$

The corresponding expression for the closed core becomes [95]:

$$Z = \int_{-\infty}^{\infty} G(a,r,\beta) \sum_{k=-\infty}^{\infty} e^{jkl} e^{j\beta z} d\beta \tag{4.42}$$

Using the Dirac comb function and its Fourier series:

$$\text{III}_T(t) := \sum_{k=-\infty}^{\infty} \delta(t-kT) = \frac{1}{T} \sum_{n=-\infty}^{\infty} e^{i2\pi n \frac{t}{T}} \tag{4.43}$$

Equation (4.42) simplifies to:

$$Z = \frac{2\pi}{l} \sum_{k=-\infty}^{\infty} G(a,r,\beta_k) e^{j\beta_k z} \tag{4.44}$$

where

$$\beta_k = \frac{2\pi k}{l} \tag{4.45}$$

Based on Equation (4.38), the impedance can be written as:

$$L_1 = \mu_1 r a \frac{2\pi}{l} \sum_{k=-\infty}^{\infty} I_1(\beta_k r) K_1(\beta_k a) e^{j\beta_k z} \tag{4.46}$$

(If $r > a$, interchange r and a in the summation.)
And, based on Equation (4.37):

$$Z_c = \frac{2\pi}{l} \sum_{k=-\infty}^{\infty} \frac{r a K_1(\beta_k a) K_1(\beta_k r) I_1(\beta_k b) F(\beta_k)}{K_1(\beta_k b)} e^{j\beta_k z} \tag{4.47}$$

where $F(\beta)$ is defined as:

$$F(\beta) = j\omega\mu_1 \left\{ \frac{f(\beta) - \frac{\mu_1}{\mu_{2z}} f(\Gamma)}{g(\beta) + \frac{\mu_1}{\mu_{2z}} f(\Gamma)} \right\} \tag{4.48}$$

with the auxiliary functions:

$$f(x) = x \frac{I_0(xb)}{I_1(xb)} \tag{4.49}$$

$$g(x) = x \frac{K_0(xb)}{K_1(xb)} \tag{4.50}$$

For practical applications, the infinite series in Equations (4.46) and (4.47) must be truncated. Noting that a single-sided summation is sufficient, they can be approximated as [95]:

$$L_1 \approx \mu_1 r a \frac{\pi}{l} \left\{ \frac{r}{a} + 4 \sum_{k=1}^{N-1} I_1(\beta_k r) K_1(\beta_k a) \sigma_k \cos(\beta_k z) \right\} \tag{4.51}$$

and

$$Z_c \approx \frac{\pi}{l} \left\{ C + 4 \sum_{k=1}^{N-1} \frac{r a K_1(\beta_k r) K_1(\beta_k a) I_1(\beta_k b)}{K_1(\beta_k b)} F(\beta_k) \sigma_k \cos(\beta_k z) \right\} \tag{4.52}$$

where:

$$\sigma_k = \frac{\sin(k\pi/N)}{(k\pi/N)} \tag{4.53}$$

C is defined as:

$$C = j\omega b^2 \left\{ \frac{2\mu_{2z} I_1(mb)}{mb I_0(mb)} - \mu_1 \right\} \tag{4.54}$$

where m is given in Equation (4.20).

To understand the physical significance of each term, consider the case where the permeability of the surrounding medium is set to zero. Physically, this suppresses the flux external to the core. In this condition, according to Equation (4.35), all terms vanish except the term related to C, identifying it as the impedance contribution from flux fully confined within the core [95]. Consequently, the remaining two terms represent contributions due to leakage flux [95].

For power transformers, the term C is dominant in the low-frequency region. This term is called core-component impedance in this thesis. At higher frequencies, the core becomes magnetically inactive and does not significantly alter the external magnetic field distribution. However, the other terms become less accurate in this regime since eddy current losses in the conductors and their impact on the field distribution are neglected.

To address this limitation, an alternative approach is adopted and discussed in the following section.

4.3. AIR-COMPONENT IMPEDANCE

As the core does not alter the magnetic flux distribution external to it in this case, the leakage flux is evaluated based on the air-core assumption. This section builds upon the works presented in [96, 97].

Starting with Maxwell's equations:

$$\nabla \times \mathbf{E} = -\frac{\partial \mathbf{B}}{\partial t} \tag{4.55}$$

$$\nabla \cdot \mathbf{B} = 0 \tag{4.56}$$

The electric field can be expressed as:

$$\nabla \times \mathbf{E} = -\nabla \times \left(\frac{\partial \mathbf{A}}{\partial t}\right) \tag{4.57}$$

$$\nabla \times \mathbf{E} + \nabla \times \left(\frac{\partial \mathbf{A}}{\partial t}\right) = \nabla \times \left(\mathbf{E} + \frac{\partial \mathbf{A}}{\partial t}\right) = 0 \tag{4.58}$$

If the curl of a vector field is zero, then that field can be expressed as the gradient of a scalar potential field. Hence:

$$-\nabla \varphi = \mathbf{E} + \frac{\partial \mathbf{A}}{\partial t} \tag{4.59}$$

Integrating both sides over the conductor cross-section, and considering the potential to be fixed over the cross-section with $\mathbf{J} = \sigma \mathbf{E}$ yields [96]:

$$-\nabla \varphi = R_{\mathrm{dc}} I + \mathrm{j}\omega \bar{\mathbf{A}} \tag{4.60}$$

where R_{dc} is the DC resistance of the conductor, $\bar{\mathbf{A}}$ is the average magnetic vector potential over the cross-section, I is the AC current, and ω is the angular frequency.
The per-unit-length AC impedance Z_{ac} for a round conductor can be calculated by dividing both sides of the Equation (4.60) by I. Note that $\mathbf{A}$ is not unique if the net current is non-zero; thus, it depends on the choice of reference point.

To specify $\mathbf{A}$ for the geometry of interest, consider the following for a single conductor:

$$\mathbf{B} = \nabla \times \mathbf{A} \tag{4.61}$$

$$\nabla \times \mathbf{B} = \nabla \times \nabla \times \mathbf{A} = \nabla(\nabla \cdot \mathbf{A}) - \nabla^2 \mathbf{A} \tag{4.62}$$

Applying the Coulomb gauge ($\nabla \cdot \mathbf{A} = 0$) and using $\nabla \times \mathbf{B} = \mu_0 \sigma \mathbf{E}$:

$$\nabla^2 \mathbf{A} = -\mu_0 \sigma \mathbf{E} \tag{4.63}$$

Since

$$\mathbf{E} = -\nabla \varphi - \mathrm{j}\omega \mathbf{A} \tag{4.64}$$

then:

$$\nabla^2 \mathbf{A} - \mathrm{j}\mu_0 \sigma \omega \mathbf{A} = \mu_0 \sigma \nabla \varphi \tag{4.65}$$

In polar coordinates, the Helmholtz equation in Equation (4.65) becomes:

$$\frac{\partial^2 A}{\partial r^2}+\frac{1}{r}\frac{\partial A}{\partial r}+\frac{1}{r^2}\frac{\partial^2 A}{\partial \varphi^2}-j\omega\sigma\mu A=\mu\sigma\nabla\varphi \tag{4.66}$$

Since **A** has only a *z*-component:

$$H_r=\frac{1}{\mu r}\frac{\partial A}{\partial \varphi},\quad H_\varphi=-\frac{1}{\mu}\frac{\partial A}{\partial r} \tag{4.67}$$

There are two regions of interest: inside and outside the conductor. Equation (4.66) can be solved by applying the method of separation of variables. The general solution is considered in the form $A(r,\varphi)=R(r)\phi(\varphi)$, and the particular solution is taken as $A=A_0$. Let us define:

$$k^2=-j\omega\sigma\mu \tag{4.68}$$

Then the governing equation becomes:

$$r^2\frac{\partial^2 R_1}{\partial r^2}+r\frac{\partial R_1}{\partial r}+(r^2k^2-\lambda)R_1=0 \tag{4.69}$$

$$\frac{\partial^2 \phi_1}{\partial \varphi^2}+\lambda\phi_1=0 \tag{4.70}$$

Due to the periodic boundary condition $A(r,\varphi)=A(r,\varphi+2\pi)$, λ must be positive and is taken as $\lambda=n^2$. The radial equation is a form of Bessel's equation. Thus, the general solution is:

$$R_1(r)=C_{1n}J_n(kr)+D_{1n}Y_n(kr) \tag{4.71}$$

Since the solution must be finite at $r=0$, $D_{1n}=0$. For the angular part:

$$\phi_1(\varphi)=A_{1n}\cos(n\varphi)+B_{1n}\sin(n\varphi) \tag{4.72}$$

Hence, the complete solution in region 1 is:

$$A_1(r,\varphi)=A_0+\sum_{n=0}^{\infty}J_n(kr)\left(A'_{1n}\cos(n\varphi)+B'_{1n}\sin(n\varphi)\right) \tag{4.73}$$

Outside the conductor, the conductivity is assumed to be zero. Therefore, the equation simplifies to Laplace's equation. Following the same method, the solution in region 2 becomes:

$$A_2(r,\varphi) = C_0 + D_0 \ln\left(\frac{r}{r_0}\right) + \sum_{n=1}^{\infty} r^n \left(A'_{2n}\cos(n\varphi) + B'_{2n}\sin(n\varphi)\right)$$
$$+ \sum_{n=1}^{\infty} r^{-n}\left(A''_{2n}\cos(n\varphi) + B''_{2n}\sin(n\varphi)\right) \tag{4.74}$$

Here, r_0 is the reference point. The zero-order logarithmic term is related to the current inside the conductor via Ampère's law, and $D_0 = -\mu_0 I/(2\pi)$. The r^{-n} terms decay with radius and are associated with the emitted magnetic potential due to the current density in the conductor. The r^n terms grow with radius and correspond to received potential from external sources.

The boundary conditions on the conductor surface at $r = a$ are:

$$\mu_c H_{r,c}|_{r=a} = \mu_0 H_{r,\text{air}}|_{r=a} \tag{4.75}$$

$$H_{\varphi,c}|_{r=a} = H_{\varphi,\text{air}}|_{r=a} \tag{4.76}$$

$$A_{z,c}|_{r=a} = A_{z,\text{air}}|_{r=a} \tag{4.77}$$

These lead to the following relations:

$$A'_{10} = -\frac{D_0}{akJ_1(ka)}$$

$$A'_{1n} = \frac{2na^{n-1}}{kJ_{n-1}(ka)}A'_{2n} = \frac{2n}{a^{n+1}kJ_{n+1}(ka)}A''_{2n}, \quad n \geq 1$$

$$B'_{1n} = \frac{2na^{n-1}}{kJ_{n-1}(ka)}B'_{2n} = \frac{2n}{a^{n+1}kJ_{n+1}(ka)}B''_{2n}, \quad n \geq 1$$

$$A_0 + A'_{10}J_0(ka) = C_0 + D_0 \ln\left(\frac{a}{r_0}\right) \tag{4.78}$$

When there are several conductors, a set of equations can be formed by equating the received part of one conductor to the summation of the emitted parts from other conductors. For this, it is necessary to express all equations in a common coordinate reference. A Cartesian coordinate system is chosen for this purpose. As shown in Figure 4.4, there is a global Cartesian coordinate system (x,y), and each conductor has a local Cartesian coordinate system (x_p, y_p) whose origin is the center of the conductor.

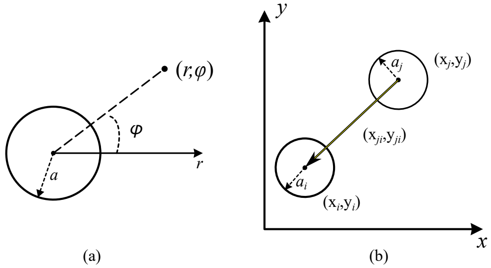

(a) (b)

Figure 4.4: Illustration of coordinates used for the 2D analysis, (a) polar coordinates for a single round conductor, (b) Cartesian coordinates for multiple conductors

The received part of conductor p can be written in its local coordinate system as:

$$A_{pr} = C_{0p} + \sum_{n=1}^{+\infty} \left\{ A'_{2np} \Re((x_p + jy_p)^n) + B'_{2np} \Im((x_p + jy_p)^n) \right\}. \tag{4.79}$$

The emitted part of conductor q, as received by conductor p, is expressed in the local coordinate system (x_p, y_p) as:

$$\begin{aligned} A_{qe} = {} & \frac{D_{0q}}{2} \ln \frac{(x_p - \Delta X_{pq})^2 + (y_p - \Delta Y_{pq})^2}{r_0^2} \\ & + \sum_{n=1}^{+\infty} \left\{ A''_{2nq} \Re\left(\left((x_p - \Delta X_{pq}) - j(y_p - \Delta Y_{pq}) \right)^{-n} \right) \right. \\ & \left. + B''_{2nq} \Im\left(\left((x_p - \Delta X_{pq}) - j(y_p - \Delta Y_{pq}) \right)^{-n} \right) \right\}. \end{aligned} \tag{4.80}$$

Note that A_{qe} is transformed to the local coordinates of conductor p using the relations $x_p = x_q + X_q - X_p$ and similarly for y_p. ΔX_{pq} and ΔY_{pq} are defined as follows:

$$\Delta X_{pq} = X_q - X_p \tag{4.81}$$

$$\Delta Y_{pq} = Y_q - Y_p \tag{4.82}$$

By expanding Equations (4.79) and (4.80) using binomial and Maclaurin series expansions, the coefficients of the terms $x_p^P y_p^Q$ in the received part A_{rp} and the emitted part A_{eq} are determined. The relation between A'_{2nq} and A''_{2nq} is known from Equation (4.78). Thus, for a system with M conductors, a system of equations is formed. Truncating the infinite series to N^{th} order facilitates the calculation process. The resulting matrix equation takes the form:

$$\begin{pmatrix} I_{2N+1} & \cdots & \alpha_{1M} \\ \vdots & \ddots & \vdots \\ \alpha_{M1} & \cdots & I_{2N+1} \end{pmatrix} \begin{pmatrix} \gamma_1 \\ \vdots \\ \gamma_M \end{pmatrix} = \begin{pmatrix} \sum_{q\neq 1} \beta_{1q} \\ \vdots \\ \sum_{q\neq M} \beta_{Mq} \end{pmatrix}. \tag{4.83}$$

By solving this system, the coefficients for conductor p are obtained. Then, the impedance of conductor p can be calculated using Equation (4.60). The obtained impedance in this way is called the air-component impedance in this thesis.

For rectangular conductors, the proposed method can be applied by replacing each conductor with several round conductors, as shown in Figure 4.5. Conceptually, a rectangular conductor can be viewed as an arrangement of numerous parallel round conductors, which helps to approximate the high-frequency behavior of the original shape. This approach reliably captures high-frequency behavior and is computationally efficient for arbitrary winding configurations.

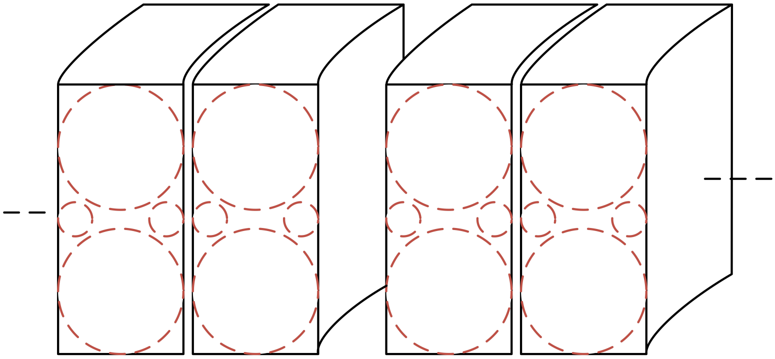

Figure 4.5: Replacing rectangular conductors with several round ones

To validate the accuracy of the applied method, the obtained results are compared with FEM simulations. For computational efficiency in FEM environment, a geometry with ten disks, each with 10 turns, is simulated. Figures 4.6 and 4.7 show the self- and mutual resistances and inductances associated with the first disk, obtained from both the analytical approach and FEM. In the analytical method, each turn is modeled using four parallel round conductors. As observed, the agreement between the FEM and analytical results is very good, which shows the accuracy of the proposed method.

4.3.1. CORE-COMPONENT VS AIR-COMPONENT

To understand the effects of the core- and air component fluxes on the impedance of the winding sections, the inductance and resistance

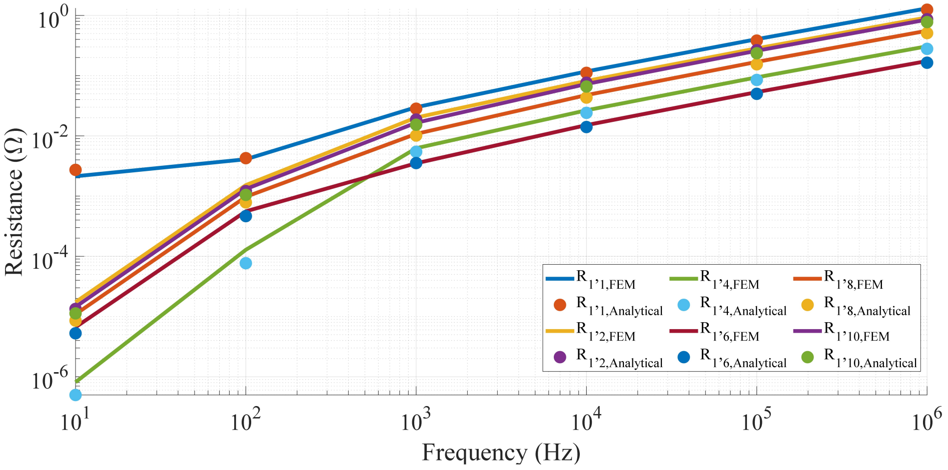

Figure 4.6: Resistance values associated with the first disk obtained from analytical formulas and FEM.

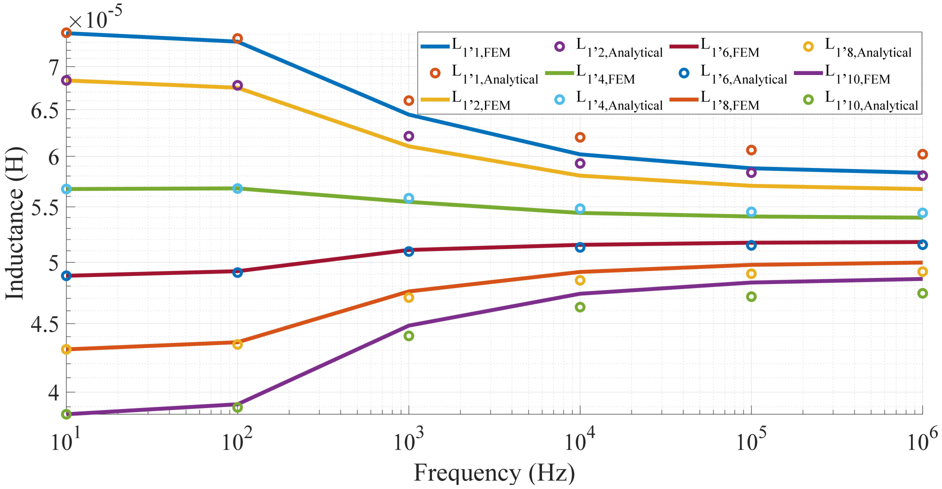

Figure 4.7: Inductance values associated with the first disk obtained from analytical formulas and FEM.

of the first section of the three-phase transformer manufactured by Royal SMIT Transformers B.V. (Figure 1.6) are plotted in Figures 4.8 and 4.9, respectively, considering each effect separately. These figures show that the impedance contribution from the core component is significantly greater than that of the air component up to several kHz. This observation further confirms that the influence of the magnetic flux external to the core on the winding impedance is negligible in the frequency range where the core remains magnetically active. Therefore, calculating the leakage flux contribution using an air-core assumption does not compromise accuracy at low frequencies. The justification for this assumption at high frequencies has already been provided earlier.

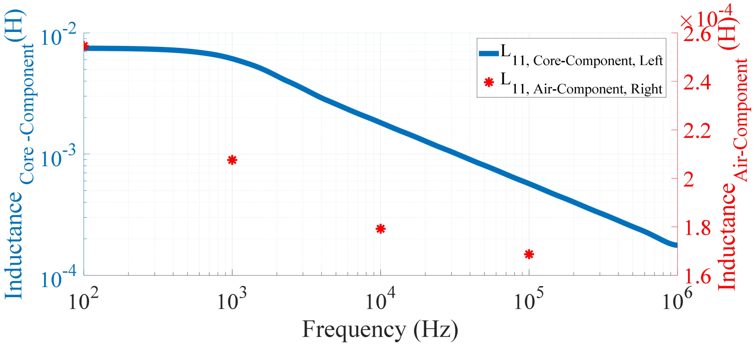

Figure 4.8: The inductance of the first transformer's disk obtained by taking into account different flux components.

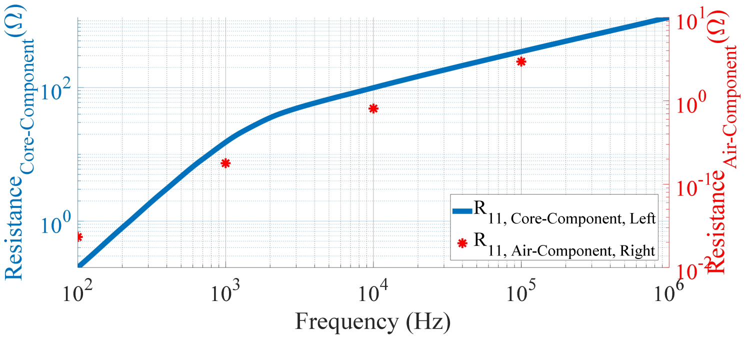

Figure 4.9: The resistance of the first transformer's disk obtained by taking into account different flux components.

4.4. TRANSFORMER ADMITTANCE MATRIX

Having all the required elements, the admittance matrix of the transformer can be obtained using:

$$\mathbf{Y} = \boldsymbol{\Gamma} + j\omega\mathbf{C} \tag{4.84}$$

$$\boldsymbol{\Gamma} = \mathbf{k}(\mathbf{R} + j\omega\mathbf{L})^{-1}\mathbf{k}^{\mathrm{T}} \tag{4.85}$$

where $\boldsymbol{\Gamma}$, $\mathbf{R}$, $\mathbf{L}$, and $\mathbf{C}$ denote the nodal impedance, resistance, inductance, and capacitance matrices, respectively. $\mathbf{k}$ is the incidence matrix, $\mathbf{k}^{\mathrm{T}}$ represents its transpose, and ω is the angular frequency. The impedance matrix $\mathbf{Z}$ can be obtained by inverting the admittance matrix $\mathbf{Y}$. The procedure for computing these matrices is described below.

4.4.1. RESISTANCE AND INDUCTANCE MATRICES

The resistance and inductance matrices are defined as branch impedance matrices. Their diagonal elements represent the self-resistance and self-inductance of the winding sections, while the off-diagonal elements represent mutual coupling between sections. Since the parameters are frequency-dependent, these matrices must be updated at each frequency point of interest.

4.4.2. INCIDENCE MATRIX

The incidence matrix transforms branch-domain resistance and inductance matrices into their corresponding nodal-domain representation. It encodes the winding topology, including star (Y) and delta connections, through an appropriate arrangement of its elements. The matrix contains only three values:

- 1 if a branch starts at a node,
- −1 if a branch ends at a node,
- 0 if the branch is not connected to the node.

4.4.3. CAPACITANCE MATRIX

The capacitance matrix is defined in the nodal domain. Its diagonal entries represent the sum of all capacitances connected to a given node, while the off-diagonal elements represent the negative of the capacitance between the corresponding pair of nodes.

4.5. CONCLUSION

This chapter presents a detailed analytical framework for modeling the frequency-dependent impedance of transformer windings, with an emphasis on the physical interpretation and separation of flux components. The formulation is structured around the decomposition of magnetic flux into core and air (leakage) components, enabling their individual contributions to be quantified and subsequently combined within a unified model. For the core flux, analytical expressions for the mutual impedance between winding turns are derived, explicitly accounting for the finite conductivity and permeability of the magnetic core. To represent the leakage flux, a magnetic vector potential-based approach is employed, where the solution of the Helmholtz equation in cylindrical coordinates accurately captures skin and proximity effects in round conductors. The framework is further extended for rectangular conductors by discretizing them into equivalent round conductors, thereby enabling efficient high-frequency modeling without a significant loss of accuracy.

By combining these techniques, the transformer admittance matrix has been constructed using frequency-dependent resistance, inductance, and capacitance matrices. This matrix-based representation facilitates the inclusion of the high-frequency behavior of transformer windings in system-level simulations, while remaining computationally efficient.

The analytical framework established in this chapter provides a reliable and versatile basis for transformer modeling across a wide frequency range. In the next chapter, the application of this model to real transformers and winding geometries is presented, along with comparisons to experimental results to validate its accuracy and effectiveness.

5

EMT-BASED TRANSFORMER MODELS FOR FAST TRANSIENTS

> *The purpose of computing is insight, not numbers.*
>
> Richard Hamming

This chapter presents the validation and practical implementation of the proposed high-frequency transformer modeling methodology through a series of case studies. Three representative configurations are examined: a high-voltage (HV) winding, a three-phase transformer, and a single-phase transformer published in CIGRÉ JWG A2/C4.52. For these cases, the high-frequency characterizations and voltage distributions are computed and compared with measurements in the frequency and time domains. To enable efficient transient simulations, model order reduction using Kron reduction is applied, and voltage amplification is analyzed to retain the most critical nodes. The reduced models are subsequently fitted using vector fitting and enforced for passivity, allowing their integration into EMT-based simulation environments.

Parts of this chapter have been published in:

- F. Nasirpour, T. Luo, M. G. Niasar, and M. Popov. "Multi-Winding Power Transformer Modeling for Fast-Front Transients". In: *IEEE Transactions on Power Delivery* (2025), pp. 1–13
- F. Nasirpour, A. Heidary, M. G. Niasar, A. Lekić, and M. Popov. "High-frequency transformer winding model with adequate protection". In: *Electric Power Systems Research* 223 (2023), p. 109637

5.1. INTRODUCTION

In the previous chapter, the methodology for determining the parameters of a high-frequency transformer model was discussed. In this chapter, the proposed approach is applied to three case studies. These include two power transformers with rated powers of 48 MVA and 50 MVA, as well as a high-voltage (HV) winding consisting of 22 disks.

The HV coil is specifically designed to allow access to the terminals of each disk, thereby enabling voltage distribution measurements along the winding. It is important to note that the modeling of the three-phase transformer is conducted by modeling each phase independently, after which the phases are interconnected to form the complete three-phase configuration.

5.2. TRANSFORMER CHARACTERISTICS

Under the assumption of linear behavior, the relationship between voltages $\mathbf{V}$ and currents $\mathbf{I}$ at different nodes of the transformer windings can be expressed as:

$$\mathbf{V} = \mathbf{Z}\mathbf{I} \tag{5.1}$$

When node j is excited by a current I_j, the resulting node voltages can be calculated as follows [99]:

$$\begin{bmatrix} V_1 \\ \vdots \\ V_j \\ \vdots \\ V_n \end{bmatrix} = \begin{bmatrix} Z_{11} & Z_{12} & \cdots & Z_{1n} \\ \vdots & \ddots & \ddots & \vdots \\ Z_{j1} & Z_{j2} & \cdots & Z_{jn} \\ \vdots & \ddots & \ddots & \vdots \\ Z_{n1} & Z_{n2} & \cdots & Z_{nn} \end{bmatrix} \begin{bmatrix} 0 \\ \vdots \\ I_j \\ \vdots \\ 0 \end{bmatrix} \tag{5.2}$$

Using Equation (5.1), the voltage distribution within the transformer windings can be determined. These results can subsequently be validated against experimental measurements in the frequency or time domain. It should be noted that in Equation (5.2), the end of the excited winding is grounded.

5.3. HIGH VOLTAGE WINDING

To validate the modeling approach using a geometry of reduced complexity, the method is first applied to a high-voltage (HV) winding before proceeding to more comprehensive transformer case studies. The HV winding consists of 22 disks, as depicted in Figure 5.1, where each disk is treated as one section in the model. Detailed coil specifications are provided in Table 5.1.

The coil includes wound-in electrostatic shields between the turns, designed to improve capacitive voltage distribution and enhance overall transformer reliability by mitigating nonlinear voltage distribution within the winding. The resulting capacitances are calculated under the assumption of linear voltage distribution in the windings and shields, again employing the energy method introduced in Chapter 2. Since the stored electric energy between the shields and turns is included in the total energy calculation, the resulting equivalent capacitance values are higher. Due to prolonged exposure to open air, the paper insulation in the coil has absorbed a significant amount of moisture. While this moisture introduces additional dielectric losses, measurements show no noticeable change in the relative permittivity of the insulation. To incorporate the effect of dielectric losses, the following loss tangent model is employed, as given in [100]:

$$\tan\delta = 1.082 \times 10^{-8} \cdot \omega + 40 \times 10^{-3} \tag{5.3}$$

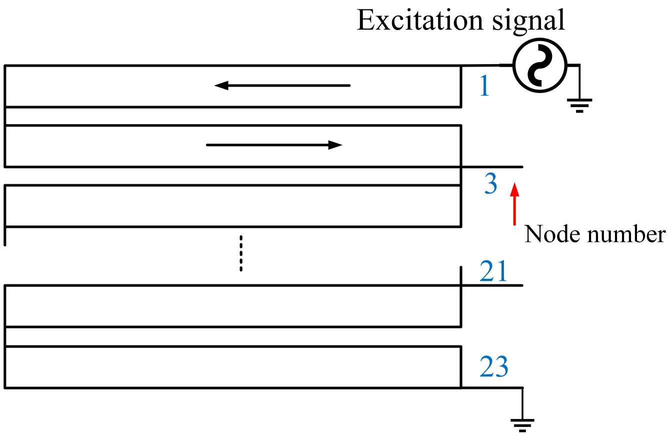

Figure 5.1: An illustration of the HV winding. Arrows indicate the winding direction.

To validate the model, voltage distribution measurements are performed along the winding at various terminals and across a range of frequencies using an Omicron Bode 100 instrument. Measurements are conducted with 50 Ω terminating resistors. Figures 5.2 and 5.3 compare the measured and modeled voltage ratios at nodes 3 and 13, respectively. The close agreement confirms the accuracy of the modeling methodology and parameter extraction.

Transient simulations are also carried out by applying triangular voltage pulses with rise times of 5 µs and 3 µs, and a fall time of 0.3 µs, as shown in Figure 5.4. The resulting voltage responses at nodes 13 and 15 are measured and compared with the simulation results in Figures 5.5 and 5.6, respectively. Nodes 13 and 15 were selected as

Table 5.1: HV Coil Parameters

Parameter	**Value**
Number of disks	22
Number of turns per disk	40
Conductor dimensions	1.8 mm × 8 mm
Insulated conductor dimensions	3.11 mm × 9.31 mm
Radial build	125.5 mm
Inner diameter	750 mm
Outer diameter	1001 mm
Vertical distance between disks	4 mm
Disks with 3 turns of shields	4
Disks with 2 turns of shields	4
Disks with 1 turn of shields	4
Disks with no shields	10

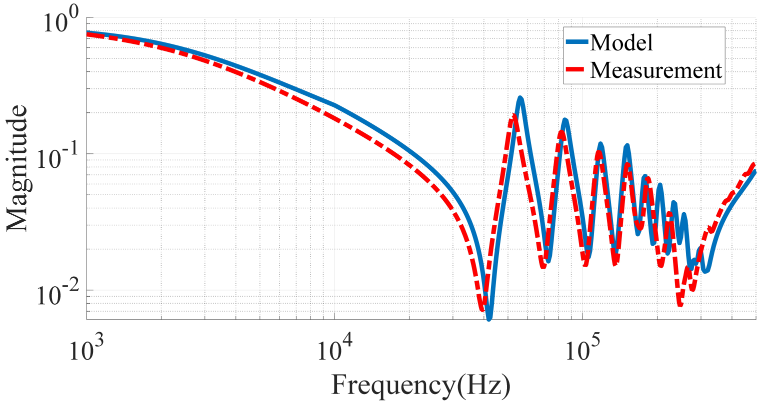

Figure 5.2: Voltage ratio at node 3 relative to the terminal voltage.

the highest voltage amplification occurs near the center of the winding. The observed oscillations at 40 kHz in both cases match the first anti-resonance frequency predicted by the model. These simulations confirm the model's fidelity in the time domain as well.

To underscore the significance of frequency-dependent inductance modeling, a separate model is developed using constant inductance values derived from [101]. In this simplified model, skin and proximity effects are neglected. The results show not only magnitude discrepancies but also significant phase shift errors when compared to measurements. This highlights the need to incorporate frequency dependence into the inductance formulation, as also emphasized in the

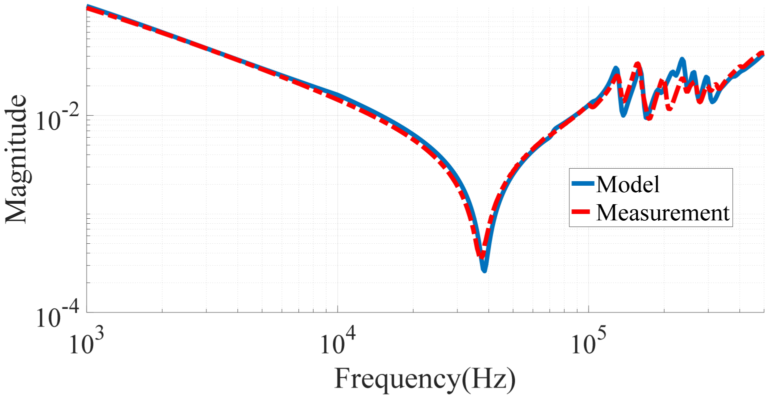

Figure 5.3: Voltage ratio at node 13 relative to the terminal voltage.

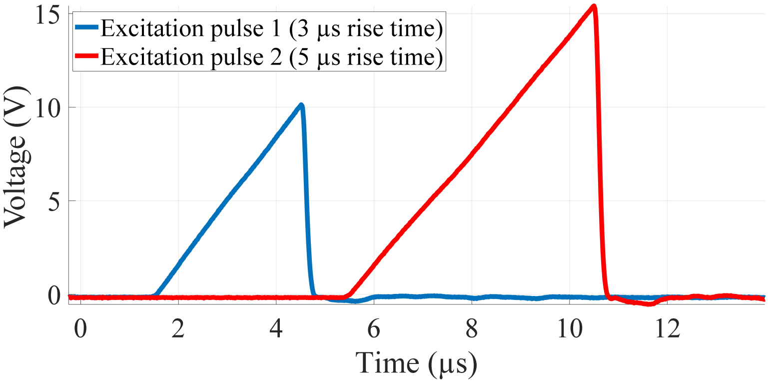

Figure 5.4: Excitation signals applied to the HV winding.

CIGRÉ Working Group A2/C4.52 [56]. For example, the voltage at node 15 predicted by the constant-parameter model is included in Figure 5.6 for comparison. Based on this figure, one might conclude that the simplified model is sufficiently accurate for the first 10-20 μs. While the voltage profiles match well during the first few microseconds in this particular case, this behavior cannot be generalized to all transformers. The winding under study exhibits high dielectric losses, which result in closely matched amplitudes between the full and simplified models. However, in other cases, this assumption may not hold. Furthermore, the resonance points predicted by the frequency-dependent model can differ significantly from those obtained using a simplified approach.

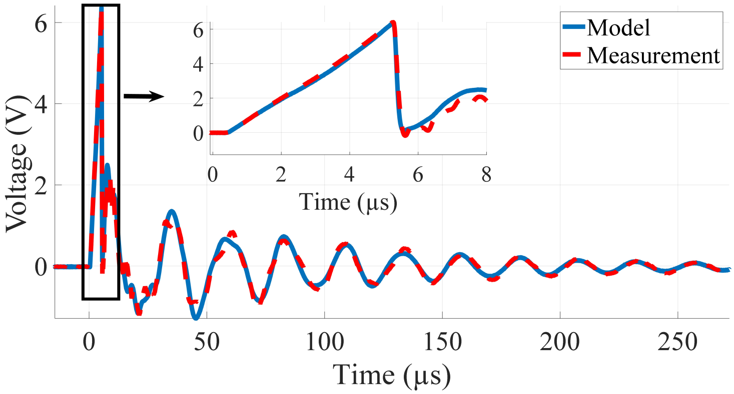

Figure 5.5: Voltage at node 13: model vs. measurement (5 µs rise time).

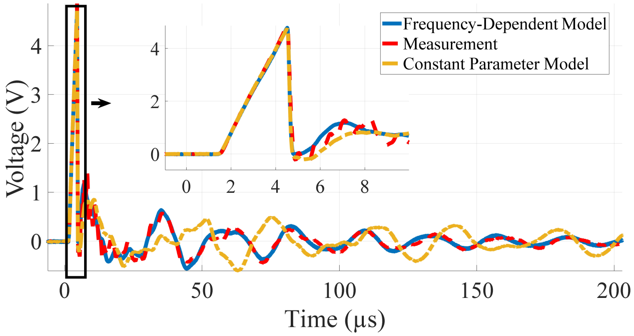

Figure 5.6: Voltage at node 15: model vs. measurement (3 µs rise time).

5.4. THREE-PHASE TRANSFORMER

The second case study involves a three-phase transformer with a rated power of 48 MVA. In addition to the conventional high-voltage (HV) and low-voltage (LV) windings, this transformer is equipped with a tap changer consisting of two coarse layer-type windings and one fine multi-start winding, providing a total of 23 tap positions. Except for the HV winding, where each disk is modeled as a separate section, each turn is considered as one section in all other windings. The general specifications of the transformer are provided in Table 5.2. In this table, G1, G2, and FW represent the transformer's tap changer windings. Specifically, G1 and G2 refer to the coarse windings, while FW represents the fine winding. Due to confidentiality agreements, full access to the transformer's detailed design data is restricted by the manufacturer.

Table 5.2: Three-Phase Transformer Parameters

Component	**Parameter**	**Value**
Transformer	Rated Power (MVA) Rated Voltage (kV) OLTC	48 150/11.2 $+12$ / -11 steps of 2.5 kV
LV Winding	Type Number of Layers Number of Turns	Layer 4 142
HV Winding	Type Number of Disks Number of Turns	Disk 90 900
G1 Winding	Type Number of Layers Number of Turns	Layer 1 144
G2 Winding	Type Number of Layers Number of Turns	Layer 1 144
FW Winding	Type Number of Steps Number of Turns	Multi-start 7 126

To investigate the influence of the magnetic core on high-frequency behavior, the complete transformer model incorporates both core- and air-flux contributions to the conductors' impedance. Figure 5.7 shows the terminal impedance of the HV winding of phase R, obtained from three modeling variations. The figure illustrates that when skin and proximity effects in conductors are accounted for, the high-frequency responses with and without considering the core converge. This occurs because, at higher frequencies, significant phase shifts emerge between different winding sections, effectively cancelling the flux contributions within the core. Consequently, the net magnetomotive force (MMF) becomes nearly zero, and the resultant core flux is negligible. The theoretical basis of this phenomenon is discussed in Chapter 3.

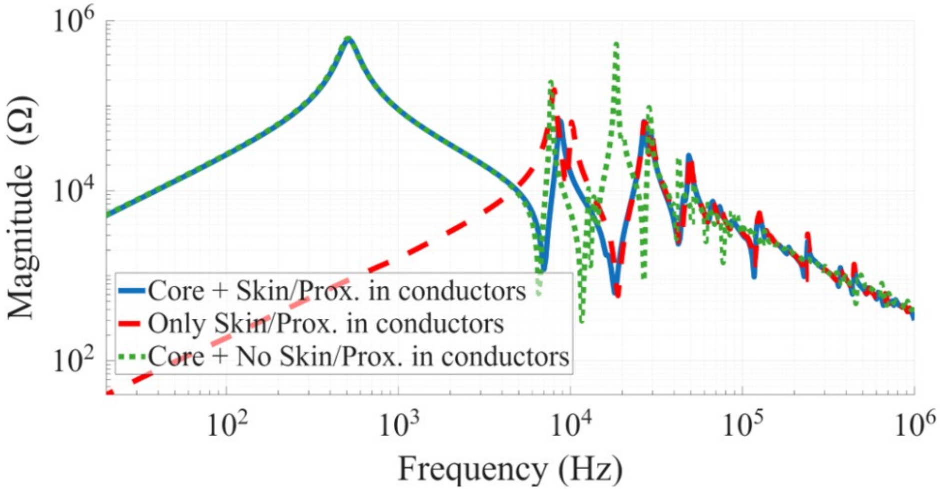

Figure 5.7: Terminal impedance of the HV winding of phase R.

Conversely, when skin and proximity effects are neglected, the high-frequency response deviates markedly. The substantial phase shift between winding sections implies that the differences in leakage impedance values across sections dictate the transformer's high-frequency behavior. Neglecting skin and proximity effects results in significant modeling errors, not only in loss estimation but also in the prediction of resonance frequencies. At lower frequencies, however, the transformer behavior is dominated by the magnetic core. Therefore, accurate modeling of core losses is essential to ensure reliable initial conditions for transient simulations. By including eddy current losses in both the core and the conductors, the model's accuracy across a broad frequency range is significantly enhanced.

To validate the model, the frequency response of the transformer is measured and compared with the simulation results. On-site frequency sweep measurements are performed using a DV FRA500 instrument. Figure 5.8 presents a comparison of the HV terminal impedance of phase R obtained from the model and the measurement, conducted at the lowest tap changer position. The good agreement observed validates the proposed modeling approach. The remaining differences between the simulated and measured responses could be attributed to unmodeled elements such as bushings, tap leads, tank.

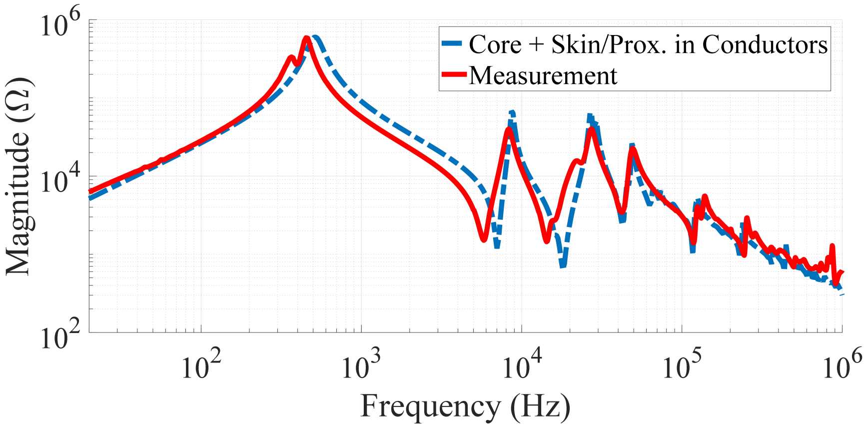

Figure 5.8: Comparison of measured and simulated terminal impedance of the HV winding of phase R.

5.5. SINGLE-PHASE TRANSFORMER

The third case study examines a single-phase transformer with a rated power of 50 MVA, as presented in CIGRÉ JWG A2/C4.52 Technical Brochure No. 904. The internal layout of this transformer is illustrated in Figure 5.9. The transformer includes four windings: tertiary (TV), low voltage (LV), high voltage (HV) and regulating (RW, tap changer).

In the model, each turn of the TV winding and each disk of the LV winding is treated as a single section. For the HV winding, each double disk is modeled as one section, while every 10 disks of the RW winding are grouped into a single modeling element. As this transformer is studied without oil, moisture absorption could influence insulation characteristics. In the absence of specific dissipation factor data in the brochure, dielectric losses are considered using Equation (5.3). The internal electrical connections and terminal designations are shown in Figure 5.9, with terminals labeled as follows: 1 (H1), 2 (X1), 3 (Y1), and

4 (Y2).

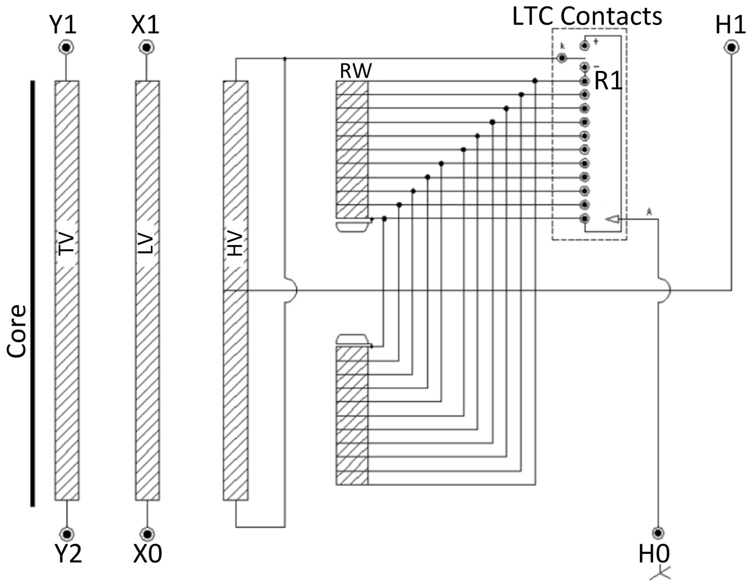

Figure 5.9: Internal connections and labeling of the single-phase transformer according to CIGRÉ JWG A2/C4.52 [102].

Figure 5.10 presents a comparison of the admittance characteristics obtained from both the developed model and the measurements. The measurement data are provided by the CIGRÉ JWG A2/C4.52 working group, as reported in [56, 102]. To further validate the model, time-domain simulations are performed. In the first simulation case, the standard lightning impulse (1.2/50 us) is applied to the HV terminal (H1), and the resulting responses at the terminals X1, Y1 and R1 are recorded. In this case, the terminals H0 and X0 are grounded, while the TV winding is left floating. In the second case, lighting impulse is applied to the LV terminal (X1) and responses are measured at H1, Y1, and R1 under the same grounding and floating conditions. The comparisons for both cases, shown in Figures 5.11 and 5.12, indicate a good agreement between the measured and simulated responses.

To examine the effect of core losses on transformer behavior, the impedance of the HV winding is evaluated for three different equivalent conductivity values: 10 S/m, 1.5 S/m, and 0 S/m, as shown in Figure 5.13. Since typical equivalent conductivity values for power transformers are below 10 S/m, variations in this parameter predominantly affect the amplitude of the resonance peaks in the low-frequency range.

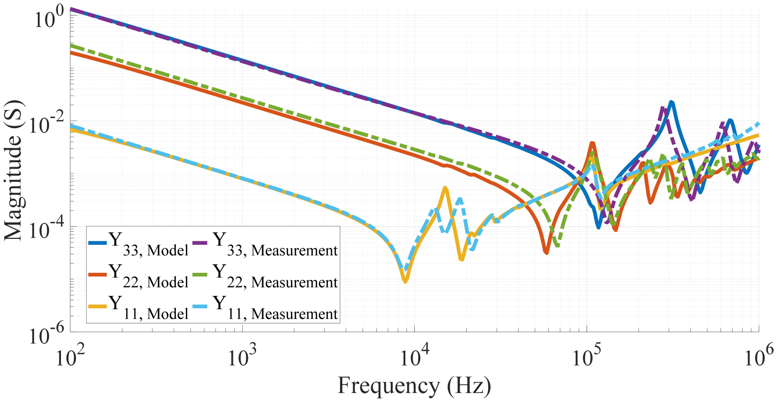

Figure 5.10: Comparison of admittance matrix elements for the CIGRÉ transformer: model vs. measurements.

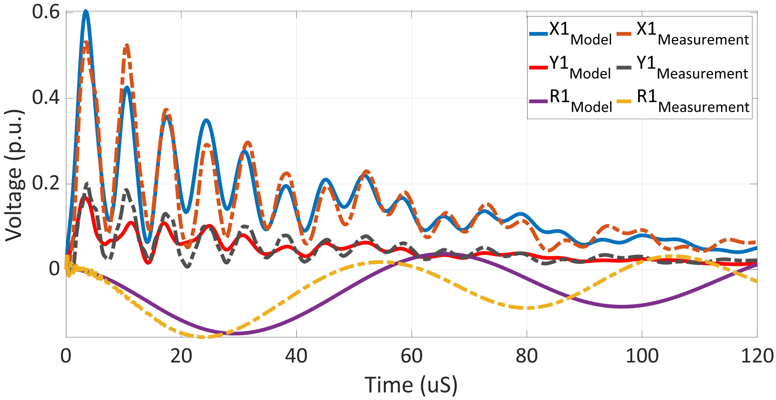

Figure 5.11: Responses at terminals X1, Y1, and R1 to a lightning impulse applied at HV terminal H1.

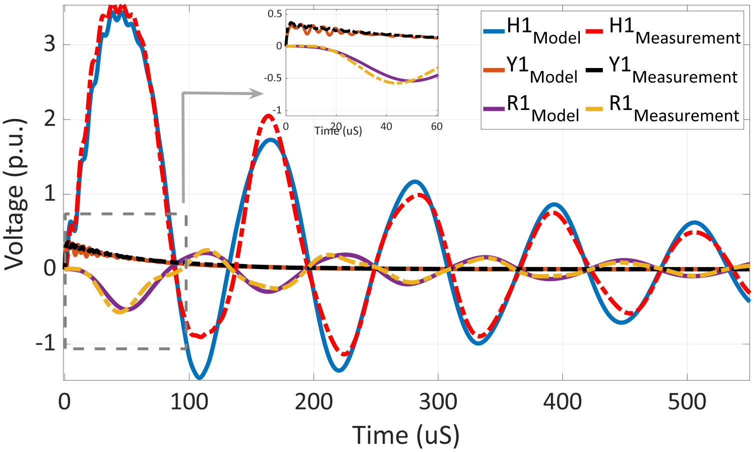

Figure 5.12: Responses at terminals H1, Y1, and R1 to a lightning impulse applied at LV terminal X1.

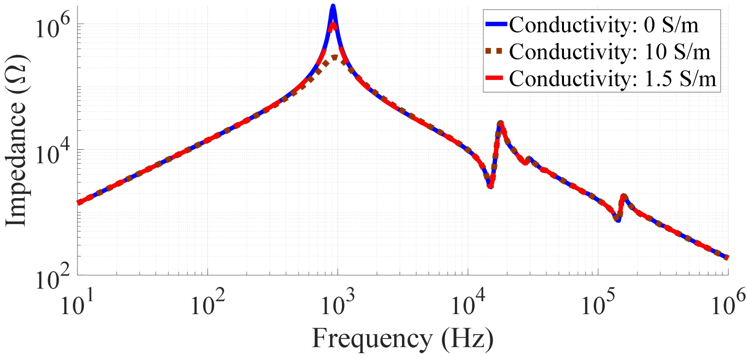

Figure 5.13: HV winding impedance obtained for different equivalent conductivity values.

5.6. EMT-BASED SOFTWARE IMPLEMENTATION

With a validated model, time-domain transient studies can be performed by implementing the model within an EMT-based simulation environment. However, because of the large number of sections and the high dimensionality of the admittance matrix, direct implementation for transient analysis is computationally unpractical. To address this, the admittance matrix must first be reduced to a smaller order while preserving the essential dynamic characteristics relevant to the study.

The Kron reduction technique is employed to reduce the original admittance matrix to a lower-order representation that retains the behavior of selected nodes of interest. This reduction can be performed using the following expression:

$$Y'_{ij} = Y_{ij} - \frac{Y_{ik}Y_{jk}}{Y_{kk}} \quad \text{for} \quad i, j \neq k \tag{5.4}$$

where k denotes the row and column to be eliminated.
To identify the most critical nodes, the amplification factor (AF) is used. It quantifies the relative voltage amplification at internal nodes compared to the terminal node. The amplification factors were analyzed across frequencies, and nodes exhibiting the highest voltage amplitudes at dominant resonances along with the terminal nodes are retained in the reduced model. The AF when the excitation is applied to terminal node i is defined as [99]:

$$AF = \frac{V_{ij}}{V_{ii}} = \frac{Z_{ij}}{Z_{ii}} \tag{5.5}$$

where V_{ii} is the terminal voltage and V_{ij} is the voltage at internal node j. Figure 5.14 illustrates the voltage amplification along the HV winding of the three-phase transformer under sinusoidal excitation at 18 kHz. This frequency corresponds to the first anti-resonance point observed in the terminal impedance (Figure 5.7) when the magnetic core is neglected. The highest voltage amplification—up to 10 p.u.—is observed in the middle section of the winding.

Alternatively, it is possible to observe only the terminal nodes and compute their corresponding voltages. By applying Equation (5.2) in the frequency domain and then using a modified Fourier transform [103], the time-domain voltages can be accurately obtained. This approach enables detailed reconstruction of the voltage distribution along the transformer winding. Figure 5.15 shows the voltage distribution in the HV winding of the transformer following the application of a standard lightning impulse (1.2/50 μs). The maximum voltage in the center of the winding reaches approximately 0.8 p.u., which, given the typical amplitudes of lightning impulses, is significantly high. The waveform exhibits oscillations at 18 kHz—again aligning with the first anti-resonance point when neglecting the core—indicating this frequency's dominant contribution due to its high amplification factor.

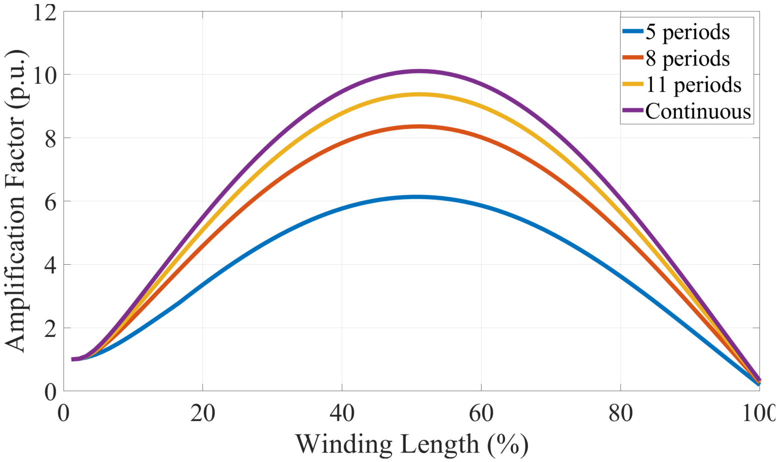

Figure 5.14: Voltage amplification in the HV winding of the three-phase transformer at 18 kHz.

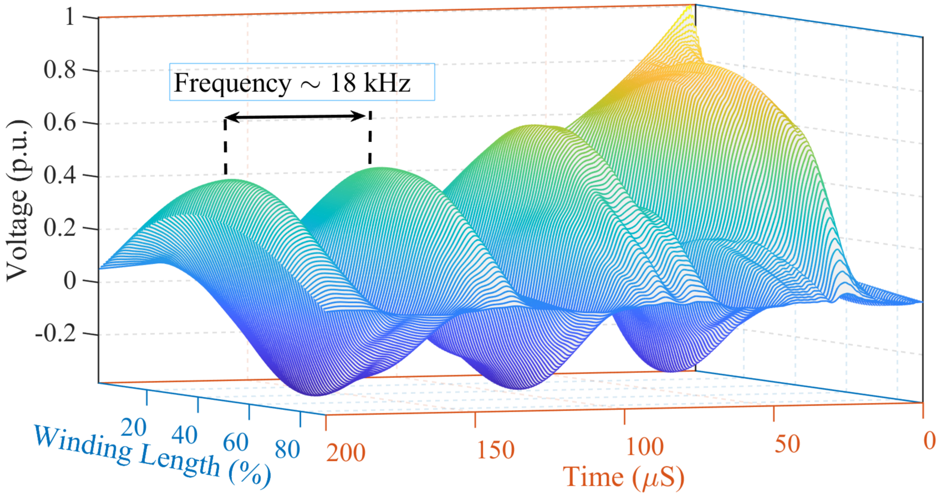

Figure 5.15: Voltage distribution in the HV winding upon applying a standard lightning impulse.

Following the matrix reduction, vector fitting and passivity enforcement algorithms [104–108] are applied to the reduced admittance matrix to ensure stability and physical reliability in the time domain. The final reduced-order model can then be implemented in an EMT software environment. Figure 5.16 compares the terminal impedance of phase R obtained from the original model and the reduced model implemented in EMT-environment. The characteristics shown correspond to the maximum tap position, with the original matrix (of order 1944) reduced to a model with only six terminals.

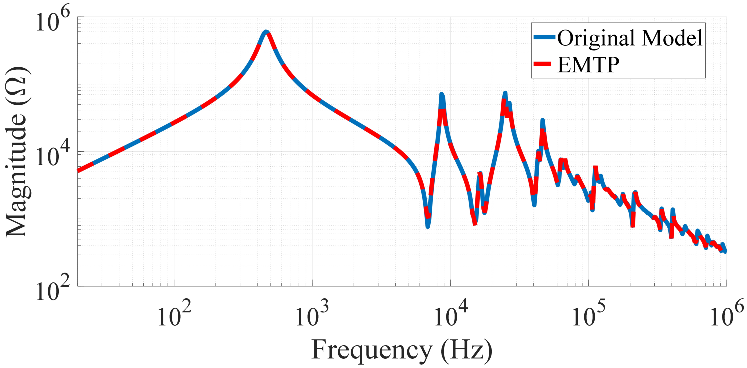

Figure 5.16: Terminal impedance of phase R: comparison between the original and the reduced model implemented in EMT-environment.

5.7. CONCLUSION

This chapter presented the application and validation of the proposed high-frequency transformer modeling approach through three comprehensive case studies: a standalone high-voltage winding, a three-phase power transformer, and a single-phase transformer published in the CIGRÉ Technical Brochure. For each case, the model accurately predicted both frequency and time-domain responses, demonstrating its robustness and practical relevance.

In the first case, detailed voltage distribution measurements along the HV winding showed excellent agreement with the simulation results, validating the accuracy of the analytical derivation and parameter extraction procedures. The second case highlighted the physical mechanisms underlying high-frequency transformer behavior, particularly the role of phase shifts and flux cancelation in rendering the magnetic core ineffective at higher frequencies. These insights reinforced the importance of accounting for skin and proximity effects in conductors to capture resonant phenomena accurately. In the third case, the model effectively reproduced admittance and transient responses of a well-documented transformer configuration, further validating its general applicability.

To enable implementation in EMT-based simulation environments, model order reduction via Kron reduction and voltage amplification analysis was employed. This allowed for the retention of critical nodes while significantly reducing the computational burden. The reduced models were subsequently fitted and enforced for passivity, enabling accurate transient studies in EMTP-type tools.

Overall, the chapter demonstrates that the developed modeling framework not only captures the relevant high-frequency phenomena with high accuracy but also enables practical integration into widely-used EMT simulation platforms. This makes it a valuable tool for transient studies in which transformers play a crucial role.

6

MACHINE LEARNING-BASED ESTIMATION OF FREQUENCY-DEPENDENT TRANSFORMER IMPEDANCE

> *A computer is like a violin. You can imagine it making beautiful music, but you have to learn how to play it*
>
> Paraphrased from ideas attributed to Marvin Minsky

This chapter presents a machine learning-based methodology for efficiently estimating the frequency-dependent impedance of transformer windings, with particular focus on the air-flux component. While the analytical approach developed in earlier chapters provides accurate results, it remains computationally intensive, especially when applied to large transformer models. To address this, a data-driven framework is introduced that leverages local conductor interactions to predict self and mutual inductance and resistance. The methodology is validated using the single-phase transformer from CIGRE JWG A2/C4.52, with time- and frequency-domain comparisons confirming the fidelity and efficiency of the proposed approach.

Parts of this chapter have been published in:

- F. Nasirpour, M. Ghaffarian Niasar, and M. Popov. “Machine Learning-Based Estimation of Frequency-Dependent Transformer Parameters for Fast-Front Transient Studies”. In: *IEEE Transactions on Power Delivery (accepted)* (2026).

6.1. INTRODUCTION

In the previous chapters, a framework for developing high-frequency transformer models was presented. The accurate computation of model parameters has a significant impact on the fidelity of these models. Among all parameters, the frequency-dependent inductances and resistances are the most computationally intensive to calculate. Chapter 4 introduced an analytical approach that offers substantial efficiency improvements compared to the finite element method (FEM). However, it remains time-consuming and resource-intensive, which may not be ideal for all types of studies.

One potential solution is to approximate the frequency-dependent inductances and resistances using functional representations. However, identifying such functions is challenging because of the complex interactions between conductors in arbitrary geometries and the wide variety of transformer designs. To address this challenge, data-driven methods are considered. These approaches enable the estimation of parameters with acceptable accuracy while significantly reducing computational costs compared to analytical or numerical methods.

The following presents a procedure for applying machine learning (ML) techniques to estimate frequency-dependent transformer parameters.

6.2. METHODOLOGY

For an accurate transient model, it is essential to incorporate frequency-dependent inductances and resistances, which arise from eddy current losses in both the core and conductors over a broad frequency range. In Chapter 4, an analytical method was developed that separately accounts for these contributions: the *core component*, representing eddy currents in the magnetic core, and the *air component*, which captures the effects of eddy currents in the conductors. The core component is computationally inexpensive and can be calculated rapidly. In contrast, the air component requires significantly more effort as a result of the complex electromagnetic interactions among the conductors. To address this computational burden, we propose an ML-based approach for efficient estimation of the p.u. length air component.

The objective is to train a model that takes as input the geometry of interest along with the frequency range and outputs the corresponding frequency-dependent inductance and resistance matrices. However, two major challenges arise. First, transformer designs vary considerably, not only in conductor size and insulation but also in the number of turns, making the input size variable. Second, the number of elements in the impedance matrices can be large. For example, a transformer with 1000 turns has 500,500 unique inductance elements, which makes the training procedure challenging.While it may seem reasonable to neglect distant conductors in the inductance matrix due to their presumed minimal influence, this assumption does not hold for compact transformer geometries. In such configurations, all conductors are in close proximity, and none of the inductance or resistance elements are truly negligible. Omitting these contributions would compromise the accuracy of the model, particularly in high-frequency transient studies. Therefore, all elements should be retained in the calculation to ensure fidelity in the electromagnetic representation.

To overcome these challenges and simplify the training process, a novel strategy is proposed that inherently fixes the input size and enables the model to be trained on a single value at a time. Before elaborating on the method, consider the geometry shown in Figure 6.1. Due to skin and proximity effects, the presence of other conductors affects the self-inductance and resistance values of the conductor i, as well as the mutual inductance and resistance between conductors i and j. Thus, for an accurate model, it is necessary to consider not only the conductor(s) of interest but also their interactions with nearby conductors. Considering this, the problem can be reformulated as follows: instead of training the model on the entire transformer geometry, where each geometry represents a single observation, we focus on the conductor(s) of interest and their k-nearest neighbors. In other words, the model takes the conductor(s) of interest and their k-nearest conductors as input and learns to predict the self- or mutual inductance and resistance. This allows us to handle varying transformer geometries with a uniform model structure. In this way, the input size of the model is fixed and independent of the total number of turns in the transformer, enhancing its generality and scalability.

Consider again Figure 6.1 as one observation. Suppose that the goal is to train a model to predict the self-inductance of the conductor i with $k = 8$. The model takes as input the characteristics (coordinates and dimensions) of the conductor i and its eight nearest conductors, the target being L_i at a specific frequency. Another observation can involve conductor j and its eight nearest neighbors, with target L_j. However, the input vectors for i and j may appear identical even though $L_i \neq L_j$. This is because the inductance also depends on the position of the conductor in the winding. Conductors located near the center are more affected by surrounding conductors than those at the periphery.

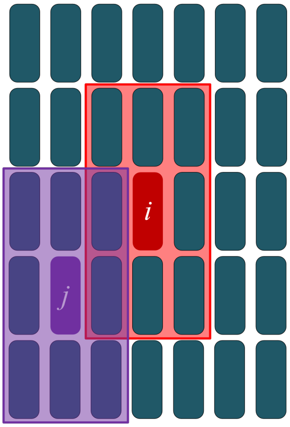

Figure 6.1: Example geometry with highlighted conductor of interest.

Moreover, the self-inductance and resistance of conductor i also depend on the total number of conductors in the geometry. For instance, Figures 6.2 and 6.3 show the self-inductance and resistance of a conductor located at the center of windings with 81, 121, 441, and 625 total turns. In other words, in Figures 6.2 and 6.3, the impedance of the same conductor is calculated while progressively increasing the number of neighbouring turns included in the computation. The physical dimensions and the position of the reference turn (x_i, y_i), remain unchanged in all cases; only the extent of the surrounding winding region considered in the calculation is varied. Figure 6.4 depicts the case with 81 turns, where the conductor under consideration is highlighted in red. It is evident that the total number of conductors significantly affects the impedance of each turn. A more compact geometry leads to stronger interactions.

To capture this effect, an additional feature, representing the relative position of the conductor of interest, is included in the input vector. The relative position of a conductor is defined with respect to the inner and outer winding boundaries. This enables the model to distinguish geometries with different numbers of turns and predict the target values more accurately, based on both relative and absolute positions.

This strategy provides several key advantages. Firstly, the model can learn how geometrical features such as conductor radii and positions influence inductance and resistance values. Secondly, it alleviates the need to generate a massive dataset of transformer geometries. If the entire geometry is used as the input, then each geometry corresponds to one training sample, necessitating a highly diverse set of transformer designs. In contrast, under the proposed method, each geometry with n turns contributes n training samples for self-inductance (or resistance)

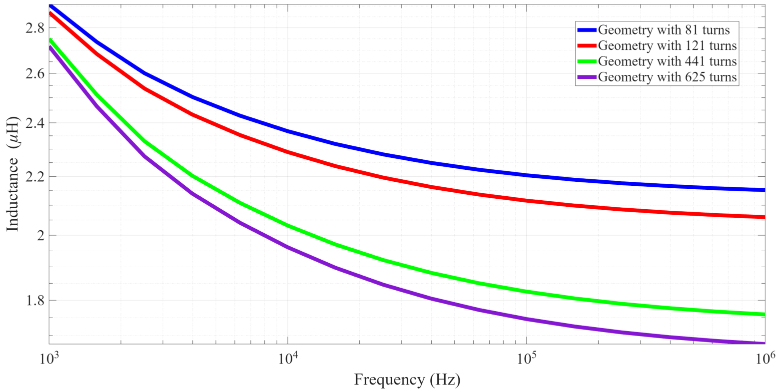

Figure 6.2: Variation of self-inductance with the total number of turns.

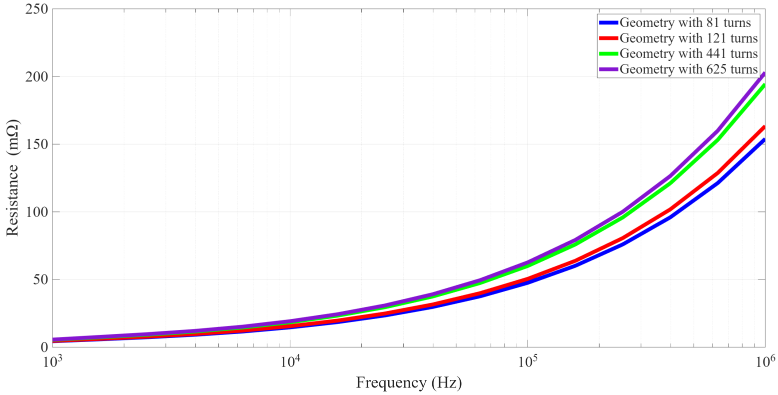

Figure 6.3: Variation of resistance with the total number of turns.

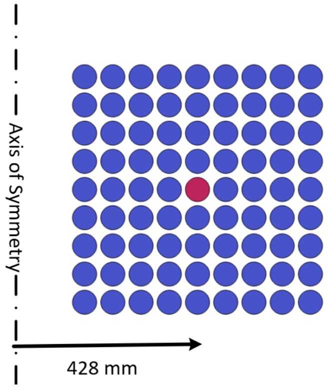

Figure 6.4: Transformer winding with 81 turns. The conductor of interest is shown in red.

and $n(n-1)/2$ samples for mutual inductance (or resistance). Hence, a dataset comprising m transformer designs with a total of N turns provides only m training instances in the conventional approach, whereas it yields $m \times N$ samples for self-inductance and $m \times N(N-1)/2$ for mutual inductance in the proposed method. It should be noted that although conductors located symmetrically with respect to the top and bottom of the winding may exhibit similar inductance values, they still form distinct feature–target pairs for training the machine-learning model. This is because their relative spatial positions within the winding are different, resulting in different feature inputs (e.g., normalized (x_i, y_i)) even when the corresponding inductance values are identical. This allows the model to learn the dependence of the impedance parameters on the conductor's position. Furthermore, the number of conductors per geometry can remain relatively small (e.g., 200 to 1000), significantly reducing the data generation burden. Once trained, the model can be applied to transformers with any number of turns, provided the number of conductors is at least $k+2$, where k is the number of nearest neighbors considered. This is not feasible under the conventional approach, where each training instance corresponds to a one transformer geometry.

In the next section, we discuss the implementation of this methodology in detail.

6.3. TRAINING A MODEL

Training a machine learning model involves several essential steps. Each of these steps is described in the following subsections.

6.3.1. DATA GENERATION

As stated earlier, the goal of the trained model is to estimate the air-flux component of the impedance matrix. To this end, the accurate analytical method developed in Chapter 4 is employed to generate training data. A total of 5000 different geometries are created, each with a varying number of turns ranging from 200 to 1000. Table 6.1 summarizes the parameters and configurations used in generating these geometries. The objective at this stage is to demonstrate the feasibility and generalization potential of the proposed method rather than to cover all possible designs

6.3.2. DATA PREPARATION

After generating the data, a Python-based preprocessing routine is developed to prepare the data for training. This routine processes the

Table 6.1: Range of parameters used for generating synthetic transformer geometries.

Parameter	Description	Range
N_{turns}	Number of turns per geometry	200 – 1000
x_{range}	Horizontal extent of winding (m)	0.15 – 1.00
r	Conductor radius (m)	0.0005 – 0.007
d_{turn}	Turn-to-turn insulation (m)	0.0001 – 0.005
d_{coil}	Coil-to-coil insulation (m)	0.0001 – 0.010
d_{winding}	Winding-to-winding insulation (m)	0.050 – 0.200

raw output and breaks it into individual observations. For example, in the case of self-inductance prediction, each observation includes:

- The features of the conductor of interest (e.g., coordinates and radius),
- The features of its k-nearest neighbors based on Euclidean distance,
- The relative position of the conductor within its respective geometry.

This processed dataset is then used to train the ML model. To ensure robust performance and avoid data leakage, the dataset is partitioned into three subsets: training, validation, and test sets. These subsets are generated from mutually exclusive geometries, ensuring that the model is evaluated on entirely unseen configurations during testing.

6.3.3. MACHINE LEARNING ALGORITHM

In this study, the *eXtreme Gradient Boosting (XGBoost)* algorithm is selected to predict the inductance and resistance values of high-frequency transformer models. XGBoost is a highly efficient and scalable implementation of gradient boosting that provides excellent predictive performance and computational speed, particularly with large datasets [110]. One of the key features of XGBoost is its built-in regularization mechanism, which penalizes overly complex models to prevent overfitting and enhance generalization [111]. XGBoost constructs an ensemble of decision trees sequentially, where each new tree attempts to correct the residual errors of the previous ensemble [112].

Mathematically, the prediction $\hat{y}$ is defined as an additive function of M trees [112]:

$$\hat{y} = F(X) = \sum_{m=1}^{M} f_m(X) \tag{6.1}$$

where $X = \{x_i | x_i \in \mathbb{R}^n\}$ denotes the input feature vectors, $y = \{y_i | y_i \in \mathbb{R}\}$ represents the target values, and $f_m(X)$ is the prediction from the m-th tree. The ensemble combines weak learners into a strong predictor through the boosting framework [112].

The optimization objective involves minimizing a loss function $l(y, \hat{y})$ that quantifies the difference between the predicted and true values. For regression tasks, the squared error is commonly used. The update, for each new tree g_m is given by [112]:

$$g_m = \arg\min_{g} \sum_{i=1}^{k} l(y_i, f_{m-1}(X_i) + g) \tag{6.2}$$

where $f_{m-1}(X)$ is the output from the previous $m-1$ trees. This iterative correction mechanism enables the model to gradually reduce residual errors.

To further enhance the model performance, Optuna's Bayesian optimization framework [110] is used for hyperparameter tuning. The following hyperparameters are optimized:

- Number of boosting rounds,
- Learning rate (step size shrinkage),
- Maximum tree depth,
- Minimum sum of instance weights per node,
- Subsample ratio of training instances,
- Subsample ratio of features,
- Minimum loss reduction required to make a split,
- L1 regularization term (`reg_alpha`),
- L2 regularization term (`reg_lambda`).

It worth mentioning that the parameter k defines the model's input size and is fixed during training. Using a different k during prediction would result in a dimension mismatch, as the trained model architecture corresponds to a specific input size.

6.4. RESULTS AND DISCUSSION

In this section, the performance of the trained model is evaluated on the test dataset. Then, the model is applied to generate the complete high-frequency model for a single-phase transformer as reported in CIGRE JWG A2/C4.52.

6.4.1. MODEL PERFORMANCE EVALUATION

Table 6.2 presents the Mean Squared Error (MSE) and coefficient of determination R^2 metrics for self- and mutual inductance at various frequencies for the test dataset. This table also shows the percentage of the predictions with errors higher than 5%. The numbers of predictions for self- and mutual inductances in this table are about 80 thousand and 10 million, respectively. A similar level of accuracy is observed for self-resistance parameters. The consistently low MSE values demonstrate the model's high predictive accuracy, while the R^2 metric confirms a strong correlation between predicted and actual values for all cases. Figure 6.5 illustrates the predicted versus actual values for a self-inductance at 100 kHz. The 45-degree reference line represents perfect accuracy, and it can be observed that nearly all predictions fall within the 5% error band. Only 0.08% of predictions exceed this threshold, demonstrating the robustness of the proposed approach. Moreover, the same level of accuracy is maintained across the entire frequency range, ensuring reliable predictions for a wide frequency range.

Table 6.2: MSE and R^2 metrics for self- and mutual inductance for different frequencies, respectively.

Frequency (kHz)	MSE ($\times 10^{-}5$)	R^2	$> 5\%$
1	2.6, 2.2	0.999, 0.999	0, 2.29
10	9, 4	0.999, 0.998	0.23, 3.96
100	4.9, 2.2	0.999, 0.999	0.08, 1.8
1000	20, 55	0.995, 0.998	1.34, 5

6.4.2. TRANSFORMER MODELS

For the actual application, the one-phase transformer from CIGRE JWG A2/C4.52 is used. Figure 6.6 presents the impedance of the HV winding obtained using the accurate analytical method compared to the characteristic obtained through the application of the ML model. As observed, the ML-based model achieves a high level of accuracy. It should be noted that while the analytical method requires approximately 12 hours to compute the parameters, the ML model completes the task within two minutes, demonstrating a significant computational advantage.

To further evaluate the model's performance, a time-domain comparison is performed. For these tests, lightning impulse signals are applied to the HV and LV terminal while all other terminals remain open. Figure 6.7 presents the results obtained from the ML-based model and compares it with experimental measurements and analytical model.

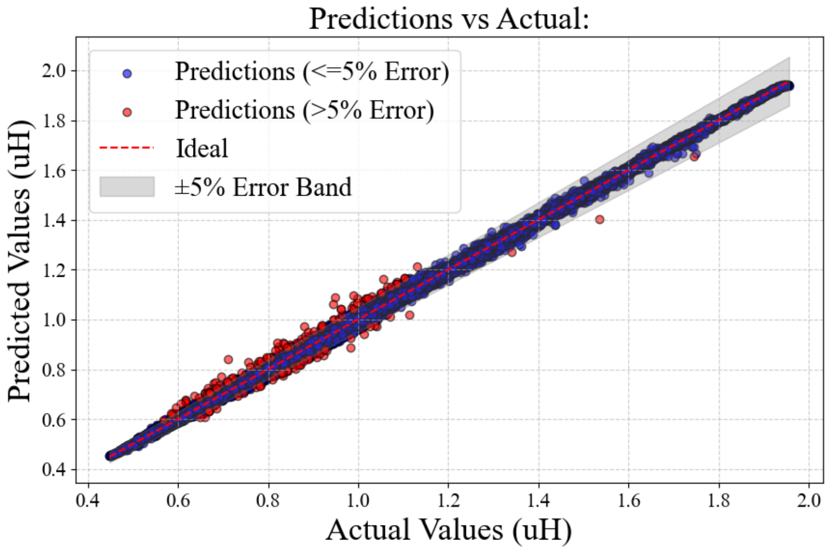

Figure 6.5: Predicted values obtained from ML vs actual values obtained from an accurate analytical method.

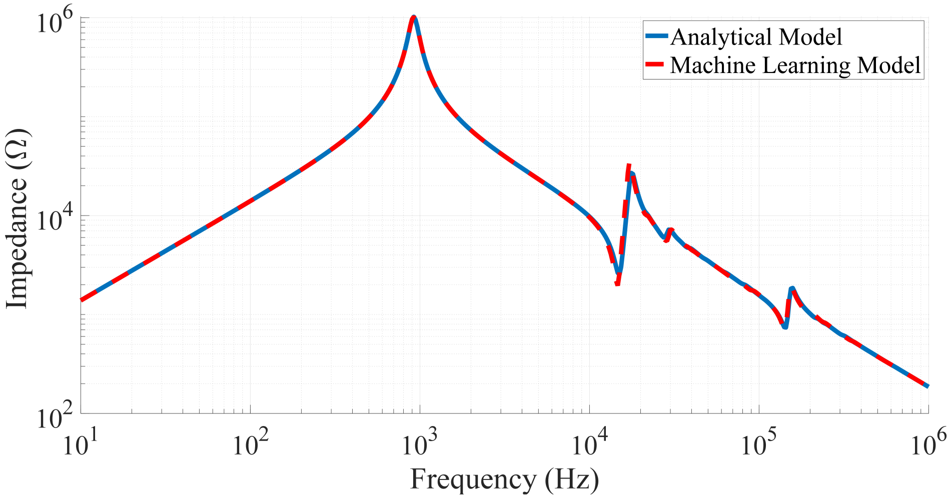

Figure 6.6: Input impedance of the HV winding obtained through ML and analytical methods.

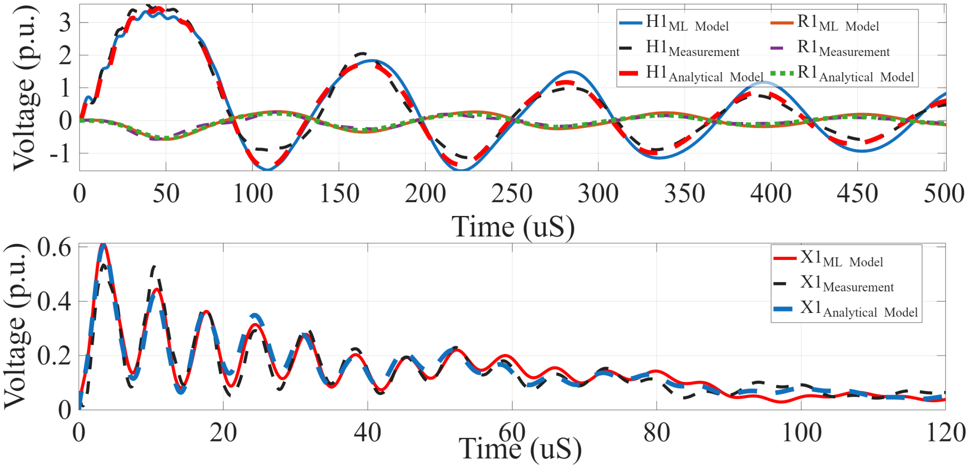

Figure 6.7: Time-domain responses to lightning impulse.

6.5. CONCLUSION

This chapter presents a machine learning-based methodology for estimating the frequency-dependent impedance of transformer windings. The proposed approach addresses the computational limitations of conventional analytical and numerical methods by introducing a scalable framework that learns from geometric configurations and their localized electromagnetic interactions. It should be noted that the machine-learning model estimates the air-flux component of the winding inductances and resistances, which is independent of the core geometry; thus, the core type does not affect the applicability of the approach in this chapter.

The key innovation is in reformulating the problem so that the model is trained on individual impedance elements rather than on entire matrices. By focusing on the conductor(s) of interest and their *k*-nearest neighbors, the method ensures fixed-size input vectors and generalizes well across transformer designs with varying numbers of turns. This approach drastically reduces the training complexity while increasing the number of effective training samples. The trained model, based on the XGBoost algorithm with hyperparameter tuning via Bayesian optimization, demonstrates high predictive accuracy for both self- and mutual impedance components across a wide frequency range. Performance evaluation using extensive test data shows excellent agreement with analytical results, with less than 1% of the self-impedance and less than 5% of mutual impedance predictions exceeding a 5% error threshold. Finally, the model was validated against a transformer case from CIGRE JWG A2/C4.52. It successfully reproduced both frequency-domain and time-domain behaviors with a high degree of accuracy, while reducing computational time from hours to minutes. This demonstrates the model's potential for fast, reliable integration into high-frequency transformer modeling workflows. Although the proposed training approach is expected to remain valid for different winding configurations, since the data generation is performed per unit length in a two-dimensional domain, it is recommended to further investigate its performance for alternative configurations, such as pancake windings. Moreover, the present machine learning model is not suitable for predicting mutual resistance values, as certain elements exhibit small negative values that adversely affect learning stability. Finally, for accurate prediction of the parameters of previously unseen geometries, the winding dimensions must fall within the ranges used during training. The number of turns, however, does not constitute a limiting factor, as discussed earlier.

7

CONCLUDING REMARKS AND RESEARCH OUTLOOK

What we know is a drop, what we don’t know is an ocean.

Isaac Newton

7.1. INTRODUCTION

This thesis presented a comprehensive analytical and data-driven framework for modeling the high-frequency behavior of power transformers. Motivated by the growing need for physically consistent and computationally efficient transformer models in electromagnetic transient (EMT) simulations, the work emphasized a white-box modeling approach that incorporates fundamental electromagnetic principles while leveraging modern numerical tools and machine learning to enhance accuracy and efficiency.

The research covered a broad spectrum—from fundamental understanding of physical phenomena to practical implementation and validation—resulting in a set of modeling tools suitable for both academic investigation and engineering applications.

7.2. SUMMARY OF MAJOR CONTRIBUTIONS

The main contributions of this thesis can be summarized as follows:

- A systematic numerical investigation was conducted to study the influence of conductor and core eddy current losses on high-frequency winding behavior. It was shown that while core losses dominate at lower frequencies, conductor eddy current losses become the primary factor at high frequencies. Notably, even with a laminated magnetic core present, the generated net magnetic flux diminishes due to distributed phase shifts along the winding, leading to a magnetically passive core behavior at higher frequencies.

- A comprehensive analytical formulation was developed to model frequency-dependent winding impedance. This included the calculation of mutual and self-impedance, considering both leakage and core flux components. Skin and proximity effects were analytically captured in this formulation.
- The analytical model was validated through three extensive case studies. These included a high-voltage winding, a three-phase transformer, and a single-phase benchmark transformer reported by CIGRÉ JWG A2/C4.52. The model demonstrated high agreement with measured and simulated results across both frequency and time domains, confirming its physical accuracy and practical applicability.
- For time-domain simulation compatibility, the full admittance matrix obtained analytically was subjected to Kron reduction to retain only critical nodes, significantly reducing model complexity. Additionally, passivity enforcement techniques were applied to ensure stability in EMT tools such as EMTP-RV, enabling reliable integration into power system studies.
- To overcome the computational burden associated with analytical or numerical impedance extraction for large systems or parameter sweeps, a machine learning framework was developed. This method reformulated the problem to estimate frequency-dependent parameters using localized geometric inputs. Using XGBoost and Bayesian optimization, the model achieved high prediction accuracy and scalability, while significantly reducing computation time from hours to minutes.

7.3. KEY FINDINGS

Several important insights emerged from this research:

- Transformer impedance is governed by different physical phenomena across the frequency spectrum. At low frequencies, the magnetic core dominates the behavior, while at high frequencies, conductor eddy current losses and associated phase shifts become more critical.
- The common assumption that the effects of the core become negligible at high frequencies is supported by cancellation of magnetomotive forces.

- Accurate high-frequency modeling requires the simultaneous evaluation of both resistance and inductance. Treating these quantities independently—common in many simplified methods—can lead to physically inconsistent results, particularly regarding damping behavior and transient response.
- Analytical modeling, when structured around electromagnetic field theory and enhanced with efficient approximations, offers a physically transparent yet computationally tractable alternative to fully numerical methods such as FEM.
- Machine learning techniques can augment or even replace traditional modeling approaches in certain contexts—especially when rapid evaluation is required for multiple transformer designs or optimization tasks.

7.4. LIMITATIONS OF THE STUDY

Despite the comprehensive scope and demonstrated capabilities, the developed framework has several limitations that should be acknowledged:

- **Applicability to foil windings:** The proposed modeling framework is not well suited for transformers with foil windings. Accurately representing a foil conductor using multiple round strands requires a large number of conductors, which significantly increases the model complexity and computational burden. In these cases, full numerical methods such as FEM may be more appropriate.
- **Magnetic nonlinearity and hysteresis:** The model assumes a linear, isotropic magnetic core and does not account for saturation, hysteresis, or core layout. While this simplification is valid for high-frequency conditions, it limits the model's accuracy under fault scenarios or core saturation effects.
- **Mutual resistance prediction in ML model:** The current machine learning model does not predict mutual resistance with sufficient accuracy. This limitation directly affects the damping behavior of the overall model.

7.5. FUTURE RESEARCH DIRECTIONS

The work presented in this thesis opens several promising avenues for future exploration:

- **Nonlinear magnetic effects:** Incorporating factors such as magnetic saturation and hysteresis would improve model fidelity.

- **Hybrid modeling:** Combining analytical modeling with deep learning or graph neural networks may further enhance the scalability and generalization of transformer models, particularly for system-level simulations or design optimization.

- **Application to monitoring:** One way to detect mechanical or electrical faults in the transformer windings is by applying FRA. One of the main challenges of the FRA is the interpretation of results, which often depends heavily on user expertise. To address this, recent research has introduced automated techniques—such as mathematical indices and AI-based classifiers—to improve diagnostic reliability. However, these methods typically rely on experimental data, which may be limited or difficult to generalize. The modeling approach presented in this study offers a complementary solution by enabling the generation of synthetic data under various fault scenarios, including disk spacing variation, axial displacement, and turn-to-turn faults. The simulated impedance changes can be used to train diagnostic models with greater accuracy and robustness, thereby enhancing the reliability of health assessments based on FRA. In summary, the proposed models could serve as a foundation for online condition monitoring, fault localization, and predictive maintenance by correlating impedance changes with evolving transformer health.

7.6. FINAL REMARKS

This thesis established a unified and physically grounded modeling strategy for capturing the high-frequency behavior of power transformers. The synergy between electromagnetic field theory, numerical validation, and machine learning resulted in a powerful yet practical modeling suite. The developed models address the pressing need for accuracy, transparency, and efficiency in transformer simulations—particularly in the context of digital substations, power-electronic interfaced grids, and renewable energy integration.

By bridging the gap between academic rigor and engineering utility, this work contributes not only to the advancement of transformer modeling but also to the broader effort of enhancing power system resilience and reliability in the face of growing complexity.

BIBLIOGRAPHY

[1] N. Chothani, M. Raichura, and D. Patel. “Advancement in Power Transformer Infrastructure and Digital Protection”. en. In: *Advancement in Power Transformer Infrastructure and Digital Protection*. Singapore: Springer Nature Singapore, 2023, pp. 27–69.

[2] C. Aj, M. Salam, Q. Rahman, F. Wen, S. Ang, and W. Voon. “Causes of transformer failures and diagnostic methods – A review”. In: *Renewable and Sustainable Energy Reviews* 82 (Feb. 2018), pp. 1442–1456. issn: 1364-0321.

[3] M. Arshad, S. Islam, and A. Khaliq. “Power transformer asset management”. In: *2004 International Conference on Power System Technology, 2004. PowerCon 2004.* Vol. 2. Nov. 2004, 1395–1398 Vol.2.

[4] M. Hamed Samimi and H. Dadashi Ilkhechi. “Survey of different sensors employed for the power transformer monitoring”. en. In: *IET Science, Measurement & Technology* 14.1 (Jan. 2020), pp. 1–8. issn: 1751-8822, 1751-8830.

[5] *Electrical transient interaction between transformers and the power system - Part 2: Case studies - Technical Brochures*. en-GB. 2014.

[6] Z. Zheng, Y. Yang, C. Li, S. Liu, and J. Ma. “Characteristics of partial discharge during its evolution in transformer winding”. In: *2010 IEEE International Symposium on Electrical Insulation*. IEEE, 2010, pp. 1–4.

[7] R. Murugan and R. Ramasamy. “Understanding the power transformer component failures for health index-based maintenance planning in electric utilities”. In: *Engineering Failure Analysis* 96 (Feb. 2019), pp. 274–288.

[8] M. Wang, A. Vandermaar, and K. Srivastava. “Review of condition assessment of power transformers in service”. In: *IEEE Electrical Insulation Magazine* 18.6 (Nov. 2002), pp. 12–25. issn: 1558-4402.

[9] S. Tenbohlen, Z. Hanif, and D. Martin. *Analysis of Major Failures of Power Transformers*. Nov. 2023.

[10] *Transformer reliability survey - Technical Brochures*. 2015.

[11] H. William and P. E. Bartley. “Failure Analysis of transformers”. In: *Proceedings of International Conference of Doble Clients*. 2000.

[12] J. C. Das. *Transients in electrical systems*. McGraw-Hill Professional Publishing, 2010.

[13] *Electrical transient interaction between transformers and the power system - Part 1: Expertise - Technical Brochures*. en-GB. 2014.

[14] J. Fuhr and T. Aschwanden. "Identification and localization of PD-sources in power-transformers and power-generators". In: *IEEE Transactions on Dielectrics and Electrical Insulation* 24.1 (Feb. 2017), pp. 17–30. issn: 1558-4135.

[15] J. McBride, T. Melle, X. M. Lopez-Fernandez, L. Coffeen, R. Degeneff, P. Hopkinson, B. Poulin, P. Riffon, A. Rocha, M. Spurlock, and L. Wagenaar. "Investigation of the Interaction Between Substation Transients and Transformers in HV and EHV Applications". In: *IEEE Transactions on Power Delivery* 36.3 (June 2021), pp. 1768–1774. issn: 1937-4208.

[16] A. Miki, T. Hosoya, and K. Okuyama. "A calculation method for impulse voltage distribution and transferred voltage in transformer windings". In: *IEEE Transactions on Power Apparatus and Systems* 3 (1978), pp. 930–939.

[17] M. Eslamian, B. Vahidi, and S. H. Hosseinian. "Analytical calculation of detailed model parameters of cast resin dry-type transformers". In: *Energy Conversion and Management* 52.7 (2011), pp. 2565–2574.

[18] W. G. Hurley and D. J. Wilcox. "Calculation of leakage inductance in transformer windings". In: *IEEE Transactions on Power electronics* 9.1 (1994), pp. 121–126.

[19] D. Wilcox, W. Hurley, and M. Conlon. "Calculation of self and mutual impedances between sections of transformer windings". In: *IEE Proceedings C Generation, Transmission and Distribution* 136.5 (1989), p. 308. issn: 01437046.

[20] M. Eslamian and B. Vahidi. "Computation of Self-impedance and Mutual Impedance of Transformer Winding Considering the Frequency-dependent Losses of the Iron Core". In: *Electric Power Components and Systems* 44.11 (July 2016), pp. 1236–1247. issn: 1532-5008, 1532-5016.

[21] M. Popov. "General approach for accurate resonance analysis in transformer windings". In: *Electric Power Systems Research* 161 (2018), pp. 45–51.

[22] Y. Shibuya and S. Fujita. "High frequency model of transformer winding". In: *Electrical Engineering in Japan* 146.3 (Feb. 2004), pp. 8–16. issn: 0424-7760, 1520-6416.

[23] E. E. Mombello. “Impedances for the calculation of electromagnetic transients within transformers”. In: *IEEE transactions on power delivery* 17.2 (2002), pp. 479–488.

[24] M. Popov, L. Van Der Sluis, R. Smeets, J. Lopez-Roldan, and V. Terzija. “Modelling, simulation and measurement of fast transients in transformer windings with consideration of frequency-dependent losses”. In: *IET Electric Power Applications* 1.1 (Jan. 2007), pp. 29–35. issn: 1751-8660, 1751-8679.

[25] M. Eslamian and B. Vahidi. “New methods for computation of the inductance matrix of transformer windings for very fast transients studies”. In: *IEEE transactions on power delivery* 27.4 (2012), pp. 2326–2333.

[26] Y. Shibuya, T. Matsumoto, and T. Teranishi. “Modelling and analysis of transformer winding at high frequencies”. In: *International Conference on Power Systems Transients (IPST’05)*. 2005.

[27] N. Abeywickrama, Y. V. Serdyuk, and S. M. Gubanski. “High-frequency modeling of power transformers for use in frequency response analysis (FRA)”. In: *IEEE Transactions on Power Delivery* 23.4 (2008), pp. 2042–2049.

[28] E. E. Mombello and G. A. D. Flórez. “An improved high frequency white-box lossy transformer model for the calculation of power systems electromagnetic transients”. In: *Electric Power Systems Research* 190 (2021), p. 106838.

[29] M. M. Kane and S. V. Kulkarni. “MTL-based analysis to distinguish high-frequency behavior of interleaved windings in power transformers”. In: *IEEE transactions on power delivery* 28.4 (2013), pp. 2291–2299.

[30] M. Eslamian and B. Vahidi. “New equivalent circuit of transformer winding for the calculation of resonance transients considering frequency-dependent losses”. In: *IEEE Transactions on power delivery* 30.4 (2014), pp. 1743–1751.

[31] M. Gunawardana, F. Fattal, and B. Kordi. “Very Fast Transient Analysis of Transformer Winding Using Axial Multiconductor Transmission Line Theory and Finite Element Method”. In: *IEEE Transactions on Power Delivery* 34.5 (Oct. 2019), pp. 1948–1956. issn: 1937-4208.

[32] E. Bjerkan and H. K. Høidalen. “High frequency FEM-based power transformer modeling: Investigation of internal stresses due to network-initiated overvoltages”. In: *Electric power systems research* 77.11 (2007), pp. 1483–1489.

[33] M. Tahir and S. Tenbohlen. “A comprehensive analysis of windings electrical and mechanical faults using a high-frequency model”. In: *Energies* 13.1 (2019), p. 105.

[34] A. Shintemirov, W. H. Tang, and Q. H. Wu. “A hybrid winding model of disc-type power transformers for frequency response analysis”. In: *IEEE Transactions on Power Delivery* 24.2 (2009), pp. 730–739.

[35] M. García-Gracia, M. Villén, M. A. Cova, and N. El Halabi. “Detailed three-phase circuit model for power transformers over wide frequency range based on design parameters”. In: *Electric power systems research* 92 (2012), pp. 115–122.

[36] S. Mousavi. “Electromagnetic modelling of power transformers for study and mitigation of effects of GICs”. PhD Thesis. KTH Royal Institute of Technology, 2015.

[37] P. Kinsler. “Faraday’s law and magnetic induction: cause and effect, experiment and theory”. In: *Physics* 2.2 (2020), pp. 150–163.

[38] M. K. Kazimierczuk. *High-frequency magnetic components*. John Wiley & Sons, 2009.

[39] JWG A2/C4.52. “High-Frequency Transformer and Reactor Models for Network Studies, Part D: Model interfacing and specifications”. In: *Conseil International des Grands Réseaux Électriques (CIGRE) Technical Brochure Nº903* (2023).

[40] R. Aghmasheh, V. Rashtchi, and E. Rahimpour. “Gray box modeling of power transformer windings for transient studies”. In: *IEEE Transactions on Power Delivery* 32.5 (2017), pp. 2350–2359.

[41] S. Jazebi, A. Rezaei-Zare, M. Lambert, S. E. Zirka, N. Chiesa, Y. I. Moroz, X. Chen, M. Martinez-Duro, C. M. Arturi, E. P. Dick, A. Narang, R. A. Walling, J. Mahseredjian, J. A. Martinez, and F. de León. “Duality-Derived Transformer Models for Low-Frequency Electromagnetic Transients—Part II: Complementary Modeling Guidelines”. In: *IEEE Transactions on Power Delivery* 31.5 (Oct. 2016), pp. 2420–2430. issn: 1937-4208.

[42] F. Nasirpour, T. Luo, M. G. Niasar, and M. Popov. “Multi-Winding Power Transformer Modeling for Fast-Front Transients”. In: *IEEE Transactions on Power Delivery* (2025), pp. 1–13.

[43] JWG A2/C4.52. “High-Frequency Transformer and Reactor Models for Network Studies, Part B: Black-Box Models”. In: *Conseil International des Grands Réseaux Électriques (CIGRE) Technical Brochure Nº901* (2023), pp. 1–88.

[44] G. H. Oliveira and S. D. Mitchell. “Comparison of black-box modeling approaches for transient analysis: A GIS case study”. In: *Proceeding of the international conference on power system transients*. 2013.

[45] B. Gustavsen. “Wideband transformer modeling including core nonlinear effects”. In: *IEEE Transactions on Power Delivery* 31.1 (2015), pp. 219–227.

[46] JWG A2/C4.52. “High-Frequency Transformer and Reactor Models for Network Studies, Part C: Grey Box Models”. In: *Conseil International des Grands Réseaux Électriques (CIGRE) Technical Brochure N^o902* (2023), pp. 1–102.

[47] S. D. Mitchell and J. S. Welsh. “Initial parameter estimates and constraints to support gray box modeling of power transformers”. In: *IEEE transactions on power delivery* 28.4 (2013), pp. 2411–2418.

[48] J. A. Martinez-Velasco. *Power system transients: parameter determination*. CRC press, 2017.

[49] M. Yang, R. Kazemi, S. Jazebi, D. Deswal, and F. de León. “Retrofitting the BCTRAN Transformer Model With Nonlinear Magnetizing Branches for the Accurate Study of Low-Frequency Deep Saturating Transients”. In: *IEEE Transactions on Power Delivery* 33.5 (Oct. 2018), pp. 2344–2353. issn: 1937-4208.

[50] V. Brandwajn, H. W. Donnel, and I. I. Dommel. “Matrix representation of three-phase n-winding transformers for steady-state and transient studies”. In: *IEEE Transactions on Power Apparatus and Systems* 6 (1982), pp. 1369–1378.

[51] J. Martinez and B. Mork. “Transformer modeling for low- and mid-frequency transients - a review”. In: *IEEE Transactions on Power Delivery* 20.2 (Apr. 2005), pp. 1625–1632. issn: 1937-4208.

[52] J. A. Martinez-Velasco and B. A. Mork. “Transformer modeling for low frequency transients-the state of the art”. In: *Proceedings of the IPST International Conference on Power Systems Transients*. 2003, pp. 1–6.

[53] E. C. Cherry. “The duality between interlinked electric and magnetic circuits and the formation of transformer equivalent circuits”. In: *Proceedings of the Physical Society. Section B* 62.2 (1949), p. 101.

[54] G. Slemon. “Equivalent circuits for transformers and machines including non-linear effects”. In: *Proceedings of the IEE - Part IV: Institution Monographs* 100.5 (Oct. 1953), pp. 129–143. issn: 2054-0701.

[55] S. Jazebi, S. E. Zirka, M. Lambert, A. Rezaei-Zare, N. Chiesa, Y. Moroz, X. Chen, M. Martinez-Duro, C. M. Arturi, E. P. Dick, A. Narang, R. A. Walling, J. Mahseredjian, J. A. Martinez, and F. de León. “Duality Derived Transformer Models for Low-Frequency Electromagnetic Transients—Part I: Topological Models”. In: *IEEE Transactions on Power Delivery* 31.5 (Oct. 2016), pp. 2410–2419. issn: 1937-4208.

[56] JWG A2/C4.52. “High-Frequency Transformer and Reactor Models for Network Studies, Part A: White-Box Models”. In: *Conseil International des Grands Réseaux Électriques (CIGRE) Technical Brochure Nº900* (2023).

[57] Q. Zhang, S. Wang, J. Qiu, X. Jing, C. Gao, J. G. Zhu, and Y. Guo. “Application of an Improved Multi-Conductor Transmission Line Model in Power Transformer”. In: *IEEE Transactions on Magnetics* 49.5 (May 2013), pp. 2029–2032. issn: 1941-0069.

[58] S. H. Hosseini and P. R. Baravati. “New high frequency multi-conductor transmission line detailed model of transformer winding for PD study”. In: *IEEE Transactions on Dielectrics and Electrical Insulation* 24.1 (Feb. 2017), pp. 316–323. issn: 1558-4135.

[59] M. Popov, L. Van der Sluis, R. P. P. Smeets, and J. L. Roldan. “Analysis of very fast transients in layer-type transformer windings”. In: *IEEE Transactions on Power Delivery* 22.1 (2006), pp. 238–247.

[60] M. Popov, L. van der Sluis, G. Paap, and H. De Herdt. “Computation of very fast transient overvoltages in transformer windings”. In: *IEEE Transactions on Power Delivery* 18.4 (Oct. 2003), pp. 1268–1274. issn: 1937-4208.

[61] Y. Shibuya, S. Fujita, and N. Hosokawa. “Analysis of very fast transient overvoltage in transformer winding”. In: *IEE Proceedings-Generation, Transmission and Distribution* 144.5 (1997), pp. 461–468.

[62] B. Gustavsen. “Improving the pole relocating properties of vector fitting”. In: *IEEE Transactions on Power Delivery* 21.3 (2006), pp. 1587–1592.

[63] B. Gustavsen and A. Semlyen. “Rational approximation of frequency domain responses by vector fitting”. In: *IEEE Transactions on power delivery* 14.3 (1999), pp. 1052–1061.

[64] B. Gustavsen. “Fast Passivity Enforcement for Pole-Residue Models by Perturbation of Residue Matrix Eigenvalues”. In: *IEEE Transactions on Power Delivery* 23.4 (2008), pp. 2278–2285.

[65] A. Semlyen and B. Gustavsen. “A half-size singularity test matrix for fast and reliable passivity assessment of rational models”. In: *IEEE Transactions on Power Delivery* 24.1 (2008), pp. 345–351.

[66] E. E. Mombello. “Modeling of a coil system considering frequency-dependent inductances and losses. Determination of the equivalent circuit impedances”. In: *Electrical Engineering (Archiv fur Elektrotechnik)* 85.3 (July 2003), pp. 137–146. issn: 0948-7921, 1432-0487.

[67] S. D. Mitchell and J. S. Welsh. “Modeling power transformers to support the interpretation of frequency-response analysis”. In: *IEEE Transactions on power delivery* 26.4 (2011), pp. 2705–2717.

[68] K. N. B. Abeywickrama, Y. V. Serdyuk, and S. M. Gubanski. “Exploring possibilities for characterization of power transformer insulation by frequency response analysis (FRA)”. In: *IEEE transactions on power delivery* 21.3 (2006), pp. 1375–1382.

[69] B. Gustavsen. “Study of transformer resonant overvoltages caused by cable-transformer high-frequency interaction”. In: *IEEE Transactions on Power Delivery* 25.2 (2010), pp. 770–779.

[70] B. Gustavsen. “Removing insertion impedance effects from transformer admittance measurements”. In: *IEEE transactions on power delivery* 27.2 (2012), pp. 1027–1029.

[71] A. Holdyk, B. Gustavsen, I. Arana, and J. Holboell. “Wideband modeling of power transformers using commercial sFRA equipment”. In: *IEEE transactions on power delivery* 29.3 (2014), pp. 1446–1453.

[72] A. Shintemirov, W. J. Tang, W. H. Tang, and Q. H. Wu. “Improved modelling of power transformer winding using bacterial swarming algorithm and frequency response analysis”. In: *Electric Power Systems Research* 80.9 (2010), pp. 1111–1120.

[73] V. Rashtchi, E. Rahimpour, and E. M. Rezapour. “Using a genetic algorithm for parameter identification of transformer R-L-C-M model”. In: *Electrical Engineering* 88.5 (June 2006), pp. 417–422. issn: 0948-7921, 1432-0487.

[74] E. Rahimpour, J. Christian, K. Feser, and H. Mohseni. “Transfer function method to diagnose axial displacement and radial deformation of transformer windings”. In: *IEEE Transactions on power delivery* 18.2 (2003), pp. 493–505.

[75] M. H. Samimi, J. Faiz, and J. Ghasemi Parchini. “Feasibility Study on the Detection of Turn-to-Turn Fault Severity in the Transformer Winding by Frequency Response Analysis and Numerical Indices”. In: *Electric Power Components and Systems* 51.9 (May 2023), pp. 856–870. issn: 1532-5008, 1532-5016.

[76] S. D. Mitchell and J. S. Welsh. “The influence of complex permeability on the broadband frequency response of a power transformer”. In: *IEEE transactions on power delivery* 25.2 (2009), pp. 803–813.

[77] R. Del Vecchio, R. M. Del Vecchio, B. Poulin, P. Feghali, D. Shah, and R. Ahuja. *Transformer design principles*. 2017.

[78] F. Nasirpour, M. H. Samimi, and H. Mohseni. “Evaluation of online techniques utilized for extracting the transformer transfer function”. In: *Scientia Iranica* 26.Special Issue on machine learning, data analytics, and advanced optimization techniques. (Dec. 2019), pp. 3582–3591. issn: 1026-3098.

[79] W. G. Hurley, M. C. Duffy, J. Zhang, I. Lope, B. Kunz, and W. H. Wölfle. “A unified approach to the calculation of self-and mutual-inductance for coaxial coils in air”. In: *IEEE Transactions on Power Electronics* 30.11 (2015), pp. 6155–6162.

[80] M. Eslamian, B. Vahidi, and S. H. Hosseinian. “Combined analytical and FEM methods for parameters calculation of detailed model for dry-type transformer”. In: *Simulation Modelling Practice and Theory* 18.3 (2010), pp. 390–403.

[81] P. Gómez and F. De Leon. “Accurate and efficient computation of the inductance matrix of transformer windings for the simulation of very fast transients”. In: *IEEE Transactions on power Delivery* 26.3 (2011), pp. 1423–1431.

[82] E. Bjerkan and H. K. Høidalen. “High frequency FEM-based power transformer modeling: Investigation of internal stresses due to network-initiated overvoltages”. In: *Electric power systems research* 77.11 (2007), pp. 1483–1489.

[83] A. D. Podoltsev, K. N. B. Abeywickrama, Y. V. Serdyuk, and S. M. Gubanski. “Multiscale computations of parameters of power transformer windings at high frequencies. Part I: Small-scale level”. In: *IEEE Transactions on magnetics* 43.11 (2007), pp. 3991–3998.

[84] K. N. B. Abeywickrama, T. Daszczynski, Y. V. Serdyuk, and S. M. Gubanski. “Determination of complex permeability of silicon steel for use in high-frequency modeling of power transformers”. In: *IEEE Transactions on Magnetics* 44.4 (2008), pp. 438–444.

[85] A. D. Podoltsev, K. N. B. Abeywickrama, Y. V. Serdyuk, and S. M. Gubanski. “Multiscale computations of parameters of power transformer windings at high frequencies. Part II: Large-scale level”. In: *IEEE Transactions on Magnetics* 43.12 (2007), pp. 4076–4082.

[86] C. T. Dervos, C. D. Paraskevas, P. D. Skafidas, and P. Vassiliou. “A Complex Permittivity Based Sensor for the Electrical Characterization of High-Voltage Transformer Oils”. In: *Sensors* 5.4 (May 2005), pp. 302–316. issn: 1424-8220.

[87] C. Dervos, C. Paraskevas, P. Skafidas, and P. Vassiliou. “Dielectric characterization of power transformer oils as a diagnostic life prediction method”. In: *IEEE Electrical Insulation Magazine* 21.1 (Jan. 2005), pp. 11–19. issn: 1558-4402.

[88] T. Luo. “Modelling and Optimization of Medium Voltage High Power Medium Frequency Transformers”. In: (2025), pp. 20–23.

[89] J. H. Harlow. *Electric power transformer engineering*. 2003.

[90] B. Gustavsen and Á. Portillo. “A damping factor-based white-box transformer model for network studies”. In: *IEEE Transactions on power delivery* 33.6 (2018), pp. 2956–2964.

[91] S. V. Kulkarn and S. A. Khaparde. *Transformer Engineering: Design, Technology, and Diagnostics*. 2012.

[92] G. M. Stein. “A study of the initial surge distribution in concentric transformer windings”. In: *IEEE Transactions on power Apparatus and systems* 83.9 (1964), pp. 877–893.

[93] F. Nasirpour, M. G. Niasar, and M. Popov. “Magnetic core effects on the high-frequency behavior of transformers”. In: *International Journal of Electrical Power & Energy Systems* 159 (2024), p. 110035.

[94] S. D. Mitchell and J. S. Welsh. “The influence of complex permeability on the broadband frequency response of a power transformer”. In: *IEEE Transactions on Power Delivery* 25.2 (2009), pp. 803–813.

[95] D. Wilcox, M. Conlon, and W. Hurley. “Calculation of self and mutual impedances for coils on ferromagnetic cores”. In: *IEE Proceedings A Physical Science, Measurement and Instrumentation, Management and Education, Reviews* 135.7 (1988), p. 470.

[96] T. Luo, M. G. Niasar, and P. Vaessen. “Two-dimensional frequency-dependent resistance and inductance calculation method for magnetic components with round conductors”. In: *IEEE Transactions on Magnetics* 60.1 (2023), pp. 1–11.

[97] T. Delaforge and H. Chazal. “Formal solution based on the magnetic potential for round conductive area”. In: *IEEE Transactions on Magnetics* 54.12 (2018), pp. 1–8.

[98] F. Nasirpour, A. Heidary, M. G. Niasar, A. Lekić, and M. Popov. “High-frequency transformer winding model with adequate protection”. In: *Electric Power Systems Research* 223 (2023), p. 109637.

[99] M. Popov. “General approach for accurate resonance analysis in transformer windings”. In: *Electric Power Systems Research* 161 (2018), pp. 45–51.

[100] E. Bjerkan. “High frequency modeling of power transformers. stresses and diagnostics”. In: (2005). (Visited on 06/04/2024).

[101] T. Luo, M. G. Niasar, and P. Vaessen. “Two-Dimensional Frequency-Dependent Resistance and Inductance Calculation Method for Magnetic Components With Round Conductors”. In: *IEEE Transactions on Magnetics* 60.1 (Jan. 2024), pp. 1–11.

[102] JWG A2/C4.52. “High-Frequency Transformer and Reactor Models for Network Studies, Part E – Measurements and Design Data”. In: *Conseil International des Grands Réseaux Électriques (CIGRE) Technical Brochure Nº904* (2023).

[103] M. Popov, L. Van Der Sluis, R. P. P. Smeets, and J. Lopez Roldan. “Analysis of Very Fast Transients in Layer-Type Transformer Windings”. In: *IEEE Transactions on Power Delivery* 22.1 (Jan. 2007), pp. 238–247. issn: 0885-8977.

[104] B. Gustavsen and A. Semlyen. “Rational approximation of frequency domain responses by vector fitting”. In: *IEEE Transactions on Power Delivery* 14.3 (1999), pp. 1052–1061.

[105] D. Deschrijver, M. Mrozowski, T. Dhaene, and D. De Zutter. “Macromodeling of multiport systems using a fast implementation of the vector fitting method”. In: *IEEE Microwave and wireless components letters* 18.6 (2008), pp. 383–385.

[106] B. Gustavsen. “Fast Passivity Enforcement for Pole-Residue Models by Perturbation of Residue Matrix Eigenvalues”. In: *IEEE Transactions on Power Delivery* 23.4 (2008), pp. 2278–2285.

[107] B Gustavsen. “Improving the pole relocating properties of vector fitting”. In: *IEEE Transactions on Power Delivery* 21.3 (2006), pp. 1587–1592.

[108] A. Semlyen and B. Gustavsen. “A half-size singularity test matrix for fast and reliable passivity assessment of rational models”. In: *IEEE Transactions on Power Delivery* 24.1 (2008), pp. 345–351.

[109] F. Nasirpour, M. Ghaffarian Niasar, and M. Popov. “Machine Learning-Based Estimation of Frequency-Dependent Transformer Parameters for Fast-Front Transient Studies”. In: *IEEE Transactions on Power Delivery (accepted)* (2026).

[110] T. Akiba, S. Sano, T. Yanase, T. Ohta, and M. Koyama. “Optuna: A Next-Generation Hyperparameter Optimization Framework”. In: *Proceedings of the 25th ACM SIGKDD International Conference on Knowledge Discovery & Data Mining*. KDD ’19. New York, NY, USA: Association for Computing Machinery, July 2019, pp. 2623–2631. isbn: 978-1-4503-6201-6.

[111] M. Patil, A. Paramane, S. Das, U. M. Rao, and P. Rozga. “Health Assessment of Solid Insulation of Mineral Oil-Filled Converter Transformer”. In: *IEEE Transactions on Dielectrics and Electrical Insulation* (2023). (Visited on 01/31/2025).

[112] W. Dong, Y. Huang, B. Lehane, and G. Ma. “XGBoost Algorithm-Based Prediction of Concrete Electrical Resistivity for Structural Health Monitoring”. In: *Automation in Construction* 114 (June 2020), p. 103155. issn: 0926-5805.

[113] F. Nasirpour, B. Behdani, A. Heidary, M. Ghaffarian Niasar, F. Ghassemi, K. Velitsikakis, M. van Riet, M. Wilkinson, M. A. van der Meijden, S. Nauta, I. Tannemaat, J. Veens, and M. Popov. “Enhancing Power Transformer Reliability: High-Frequency Modeling, Transient Interactions, and Overvoltage Protection Scheme”. In: *Cigre* Paris.Ref C4-10531-2024 (Aug. 2024).

ACKNOWLEDGEMENTS

This story begins long before this thesis.

It begins with my parents, whose love, patience, and sacrifices shaped the foundation of my life. Their unwavering support, trust, and belief in me created a sense of security that allowed me to move forward with confidence, even when the path ahead was uncertain. Everything I have achieved rests upon what they gave me first.

From there, my path was shaped by those who transformed curiosity into deeper understanding. I am especially grateful to my high school mathematics teacher, Mr. Vakili. While my interest in mathematics already existed, his way of teaching elevated it to another level. He changed how I approached problems, emphasizing depth of understanding over routine solutions, and encouraged a way of thinking that sought meaning rather than answers alone. That shift in perspective stayed with me and quietly influenced the direction I would later follow. As I moved forward, I was fortunate to meet mentors who refined the way I think and approach problems. I am sincerely thankful to my master's supervisor, Dr. Samimi, whose guidance strengthened my critical thinking and helped me develop a disciplined and thoughtful approach to problem-solving. I would also like to thank my doctoral supervisors. Prof. Popov was always present with steady support, careful attention to detail, and a willingness to help whenever needed. His reliability and thoughtfulness brought clarity and confidence throughout this process. I am especially grateful to Dr.Ghaffarian, with whom I shared many long and inspiring discussions. His creativity, brilliance, and exceptional personality made working together both stimulating and genuinely enjoyable. I consider myself very fortunate to have met such a remarkable person.

I would also like to express my sincere appreciation to the members of the PRoteuS user committee: Mr. K. Velitsikakis, Mr. I. Tannemaat, Prof. M. van der Meijden, Dr. S. Naura, Mr. L. Dorpmanns, Mr. J. Veens, and Mr. M. van Riet. Their openness, insightful discussions, and willingness to share experience and data provided essential support throughout this project. Their contributions helped ground this work in practical relevance and significantly enriched its development.

Alongside this path, my brothers, Abolfazl, Mohammad, and Ali, were always there. With them, time seems to pass without notice, and the moments we share are filled with laughter, warmth, and lasting memories. Their presence has been a constant reminder of where I belong.

Friendship has also been an essential part of this journey. I am grateful to my dearest friends—Iman, Mohammad, Sobhan, and Saeed—for years of shared experiences that shaped who I am today. I also thank the friends I made during my master's studies, including Mojtaba, Mehran, Adel, Sadjed, and Milad, for the meaningful experiences and memories we share. I am particularly thankful to Mojtaba for his influence and support during that time. After moving to the Netherlands, I was fortunate to form new friendships with Sobhan, Reza, Hassan, Behzad, Mojtaba, Amir S., Amir H., Ali, and Javad, to name but a few, who made a new place feel like home. I also thank my office mates, Aleksandar, Milan and Wouter, for the pleasant atmosphere and shared days that made work more enjoyable.

Above all, I thank the Creator for guiding me through every stage of my life—for strength in difficult moments, patience when the path was unclear, and the countless blessings that carried me forward.

Finally, I thank my beautiful and loving wife, Shiva. She has been my constant support, my calm in difficult times, and my strength when I needed it most. Her love, patience, and understanding gave meaning to every step of this journey. Nothing I have done would have been possible without her.

To all those named here, and to those whose influence lives quietly between the lines, I offer my sincere gratitude. This work stands as a small reflection of the love, support, and shared moments that accompanied me along the way.

Farzad

LIST OF PUBLICATIONS

1. F. Nasirpour, M. Ghaffarian Niasar, and M. Popov. “Machine Learning-Based Estimation of Frequency-Dependent Transformer Parameters for Fast-Front Transient Studies”. In: *IEEE Transactions on Power Delivery (accepted)* (2026)
2. F. Nasirpour, T. Luo, M. G. Niasar, and M. Popov. “Multi-Winding Power Transformer Modeling for Fast-Front Transients”. In: *IEEE Transactions on Power Delivery* (2025), pp. 1–13
3. F. Nasirpour, M. G. Niasar, and M. Popov. “Magnetic core effects on the high-frequency behavior of transformers”. In: *International Journal of Electrical Power & Energy Systems* 159 (2024), p. 110035
4. F. Nasirpour, B. Behdani, A. Heidary, M. Ghaffarian Niasar, F. Ghassemi, K. Velitsikakis, M. van Riet, M. Wilkinson, M. A. van der Meijden, S. Nauta, I. Tannemaat, J. Veens, and M. Popov. “Enhancing Power Transformer Reliability: High-Frequency Modeling, Transient Interactions, and Overvoltage Protection Scheme”. In: *Cigre* Paris.Ref C4-10531-2024 (Aug. 2024)
5. F. Nasirpour, A. Heidary, M. G. Niasar, A. Lekić, and M. Popov. “High-frequency transformer winding model with adequate protection”. In: *Electric Power Systems Research* 223 (2023), p. 109637